Advanced Computational Studies of

Collisions of

Complex Atoms, Ions, and Molecules

by

Chih-Yuan Lin

(Under the direction of Phillip C. Stancil)

Abstract

This dissertation focuses on the theoretical investigation of non-adiabatic collision processes of complex atoms, ions, and molecules. The inelastic processes, particularly charge transfer due to ion-atom collisions and quenching and excitation in atom-atom collisions, are studied using a quantum-mechanical molecular-orbital close-coupling method, which is based on the perturbed stationary state approach adopting molecular orbitals as basis functions. Within this collision model, the motion of nuclei is governed by adiabatic potential energy surfaces which are constructed from the motion of electrons. Transitions between adiabatic molecular states are driven by non-adiabatic couplings. With the adiabatic potential energies and non-adiabatic couplings provided by the multireference single- and double-excitation configuration interaction method, a set of coupled Schrödinger equations is solved to obtain the collisional cross sections. We discuss the theoretical method in detail giving the coupled-channel equations in the adiabatic and diabatic representations. A transformation between the adiabatic and diabatic pictures are described. The partial wave analysis to obtain radial coupled equations and the resulting S-matrix is discussed. In order to extend the current theoretical method for ion-atom collisions to ion-molecule collisions, the infinite

order sudden approximation is adopted to reduce the complexity arising from the rotational motion of molecular targets. Applications of these methods to three different collision systems are given. In N-H⁺ collisions, rate coefficients, total and state-selective cross sections for electron capture processes are presented. For Na-He collisions, collisional cross sections and rate coefficients for elastic scattering and inelastic quenching and excitation are given. Additionally, the variation of scattering lengths with reduced mass and collision energy and their relation to vibrational bound states of the quasi-molecule are illustrated. Finally, for H⁺-CO collisions, we calculate vibrationally-resolved cross sections elucidating vibronic transitions for three different orientation angles. Angle-averaged results are given. The steric effect is prominent in the angle-dependent results.

INDEX WORDS:

ion-atom collisions, atom-atom collisions, ion-molecule collisions, charge exchange, scattering length, vibronic interactions, non-adiabatic interactions

ADVANCED COMPUTATIONAL STUDIES OF COLLISIONS OF COMPLEX ATOMS, IONS, AND MOLECULES

by

CHIH-YUAN LIN

B.A., Soochow University, Taiwan, 1997M.S., National Taiwan University, Taiwan, 2001

A Dissertation Submitted to the Graduate Faculty of The University of Georgia in Partial Fulfillment of the

Requirements for the Degree

DOCTOR OF PHILOSOPHY

ATHENS, GEORGIA

© 2007

Chih-Yuan Lin

All Rights Reserved

ADVANCED COMPUTATIONAL STUDIES OF COLLISIONS OF COMPLEX ATOMS, IONS, AND MOLECULES

by

CHIH-YUAN LIN

Approved:

Major Professor: Phillip C. Stancil

Committee: Henning Meyer

Timothy G. Heil Robert J. Buenker

Electronic Version Approved:

Maureen Grasso Dean of the Graduate School The University of Georgia May 2007

DEDICATION

This dissertation is dedicated to my loving wife, Yen-Yi, for giving me the strength and courage to overcome all difficulties, and to my baby son, Wei-Hsiang, whose arrival has brought new light in our family. I also deeply appreciate my father and mother, my brother, Chih-Hsun, my sister, Yu-Ching, and my mother-in-law for always being there and giving me your support and encouragement. Thank you all! Without all of you, I couldn't make this far.

ACKNOWLEDGMENTS

There are several to whom I owe a sincere debt of gratitude. First and foremost, I would like to acknowledge my advisor, Prof. Phillip Stancil for his guidance, patience, and encouragement. He was always available for discussion with me and gave me the freedom and confidence to explore areas of my own interests. From him, I have learned not only how to complete an academic research, but also how to become a better individual. Without his support in all respects, this research would have never been possible. In addition, I am thankful for our group member Libo Zhao, whose profuse experience in Atomic Physics gives me very useful help and inspiration. I also want to thank other group members Benhui Yang and Jason Perry for sharing the wonderful time together in our office.

I also would like to thank Prof. Robert Buenker for his helpful discussion with me and giving me useful advice. In addition, I am deeply appreciative of his group's members, Peter Funke, H.-Peter Liebermann, J. P. Gu, and Yan Li for our cooperation.

Many thanks go to Prof. Mineo Kimura. I appreciate his assistance and direction when I visited him at Kyushu University in Japan. I also would like to thank Wasa Satomi for her help during my stay in Japan.

My thanks also go to Prof. David Landau and all members of the Center for Simulational Physics (CSP) for offering me opportunities to give seminars and creating a friendly and supportive research atmosphere for us.

Finally, I would like to express my gratitude to my committee members, Prof. Henning Meyer and Prof. Timothy Heil for their effort and time to look through my dissertation and giving me helpful comments.

Table of Contents

			Page
Ackn	OWLEDG	GMENTS	V
List o	of Figu	RES	viii
List o	of Tabi	ES	xiii
Снар	TER		
1	Intro	DUCTION	1
2	THE S	CATTERING THEORY	7
	2.1	Coupled-Channel equations in the adiabatic representation	7
	2.2	Coupled-Channel equations in a diabatic representation .	14
	2.3	Adiabatic-diabatic transformation	16
	2.4	Partial wave analysis	19
	2.5	The scattering S -matrix	23
	2.6	Infinite order sudden approximation	27
3	ELECT	TRON CAPTURE IN COLLISIONS OF N^+ WITH H AND H^+ WITH N	32
	3.1	Introduction	32
	3.2	ELECTRONIC STRUCTURE CALCULATIONS	33
	3.3	Potentials and Couplings	34
	3.4	RESULTS AND DISCUSSION	35
	3.5	Astrophysical Implications	42
	3.6	SIIMMADV	18

4	ELAST	TC AND INELASTIC PROCESSES IN COLLISIONS OF NA(3S,3P) WITH	
	He fr	OM THERMAL ENERGIES TO THE ULTRACOLD	49
	4.1	Introduction	49
	4.2	ELECTRONIC STRUCTURE CALCULATIONS	51
	4.3	Potentials and Couplings	52
	4.4	RESULTS AND DISCUSSION	54
	4.5	ASTROPHYSICAL IMPLICATIONS	72
	4.6	Summary	78
5	Vibra	TIONALLY-RESOLVED CHARGE TRANSFER FOR PROTON COLLISIONS	
	WITH	CO AND H COLLISIONS WITH CO ⁺	80
	5.1	Introduction	80
	5.2	ELECTRONIC STRUCTURE CALCULATIONS	82
	5.3	RESULTS AND DISCUSSION	83
	5.4	ASTROPHYSICAL AND ATMOSPHERIC APPLICATIONS	100
	5.5	Summary	100
6	SUMM	ARY AND FUTURE RESEARCH	120
Вівці	OGRAPH	Y	123
Appen	NDIX		
A	THE D	DERIVATION OF COUPLED-CHANNEL EQUATIONS	130
В	The R	ROTATION MATRIX	132
\mathbf{C}	ELECT	TRONIC WAVE FUNCTION DERIVATIVES IN THE BF FRAME	135
D	Angui	LAR MOMENTUM IN SPHERICAL POLAR COORDINATES	137
E	Тотаі	L ANGULAR MOMENTUM	138
F	Тне п	AAISING AND LOWERING OPERATOR	141
G	THE D	DIFFERENTIAL CROSS SECTION	143

LIST OF FIGURES

2.1	The relation between the space-fixed coordinates (x, y, z) and the body-fixed	
	coordinates (x', y', z')	9
2.2	Jacobi coordinates for a A-BC system	28
3.1	Adiabatic potentials for NH^+ as a function of internuclear distance $R.$	36
3.2	Nonadiabatic radial and rotational couplings for the $\mathrm{NH^{+}}$ system as functions	
	of internuclear distance R	37
3.3	Diagonal diabatic potential curves compared to the adiabatic potential energies.	38
3.4	Off-diagonal diabatic potentials for the quartet, and doublet states of the $\mathrm{NH^{+}}$	
	system as a function of internuclear distance R	39
3.5	Total and state-selective electron capture cross sections for \mathcal{N}^+ collisions with	
	H	43
3.6	Total cross sections for N(2 p^3 $^2D^o$) + H ⁺ \rightarrow N ⁺ (2 p^2 3P) + H and N(2 p^3 $^4S^o$)	
	$+ H^{+} \rightarrow N^{+}(2p^{2} {}^{3}P) + H. \dots $	44
3.7	Rate coefficients for the collision of \mathcal{N}^+ with atomic hydrogen as a function of	
	temperature T	45
3.8	Rate coefficients for the collision of ${\mathcal H}^+$ with atomic nitrogen as a function of	
	temperature T	46
4.1	Adiabatic and diabatic potentials for Na-He as functions of internuclear dis-	
	tance R	55
4.2	The nonadiabatic radial coupling and its corresponding off-diagonal diabatic	
	potential coupling for Na-He as a function of internuclear distance $R.$	56
4.3	Nonadiabatic rotational couplings and their corresponding off-diagonal dia-	
	batic couplings for Na-He as functions of internuclear distance R	57

4.4	The total Na-He elastic cross section for the 1 $^{2}\Sigma^{+}$ state and its partial-wave	
	cross sections for $J=0$ -2 as functions of collision energy	61
4.5	The total Na-He elastic cross section for the 1 $^2\Pi$ state and its partial-wave	
	cross sections for $J=1$ -5	62
4.6	The total Na-He elastic cross section for the 2 $^2\Sigma^+$ state and its partial-wave	
	cross sections for $J=1$ -5	63
4.7	The total and state-to-state quenching cross sections for Na-He	64
4.8	The total and state-to-state excitation cross sections for Na-He	65
4.9	Rate coefficients of elastic collision processes as functions of temperature T	
	for Na-He	66
4.10	Rate coefficients of inelastic collision processes, Na(3p $^2P^o$)+He \rightarrow Na(3s 2S)+	
	He and Na(3s 2S) + He \rightarrow Na(3p $^2P^o$) + He, as functions of temperature T .	67
4.11	The Na-He scattering length as a function of reduced mass and collision energy	
	for the 1 ${}^2\Sigma^+$ $(J=0)$	70
4.12	The Na-He scattering length as a function of reduced mass and collision energy	
	for the 2 $^2\Sigma^+$ $(J=0)$	71
4.13	The variation of the Na-He scattering length for the 1 $^2\Sigma^+$ with reduced mass	
	$(E = 10^{-13} \text{ eV})$	73
4.14	The variation of the Na-He scattering length for the 2 $^2\Sigma^+$ with reduced mass	
	$(E = 10^{-13} \text{ eV})$	74
4.15	The variation of the Na-He binding energies for the 1 $^2\Sigma^+$ with reduced mass.	75
4.16	The variation of the Na-He binding energies for the 2 $^2\Sigma^+$ with different	
	reduced mass for bound states of $v=0$ and $J=0.$	76
5.1	Collisions of H^+ with CO defined in Jacobi coordinates	83
5.2	Adiabatic potential curves of H-CO ⁺ as functions of R with $r=r_{\rm e}.$	84
5.3	Adiabatic potential curves of H-CO ⁺ as functions of R with $r=1.7,1.9,2.1,$	
	2.3, and 2.5 a_0 for $\gamma = 0^{\circ}$	85

5.4	Adiabatic potential curves of H-CO ⁺ as functions of R with $r = 1.7, 1.9, 2.1,$	
	2.3, and 2.5 a_0 for $\gamma = 90^{\circ}$	86
5.5	Adiabatic potential curves of H-CO $^+$ as functions of R with $r=1.7,1.9,2.1,$	
	2.3, and 2.5 a_0 for $\gamma = 180^{\circ}$	87
5.6	Nonadiabatic radial couplings of H-CO ⁺ as functions of R with $r=1.7,1.9,$	
	2.1, 2.3, and 2.5 a_0 for $\gamma = 0^{\circ}$	88
5.7	Nonadiabatic radial couplings of H-CO ⁺ as functions of R with $r=1.7,1.9,$	
	2.1, 2.3, and 2.5 a_0 for $\gamma = 90^{\circ}$	89
5.8	Nonadiabatic radial couplings of H-CO ⁺ as functions of R with $r=1.7,1.9,$	
	2.1, 2.3, and 2.5 a_0 for $\gamma = 180^{\circ}$	90
5.9	Diabatic potentials of H-CO $^+$ as functions of R for the vibronic states shifted	
	from X $^1\Sigma^+$ and 2 $^1\Sigma^+$ at $\gamma=0^\circ$ with $r=r_{\rm e}.$	91
5.10	Diabatic potentials of H-CO $^+$ as functions of R for the vibronic states shifted	
	from 1 $^1A'$ and 2 $^1A'$ at $\gamma = 90^\circ$ with $r = r_{\rm e}$	92
5.11	Diabatic potentials of H-CO $^+$ as functions of R for the vibronic states shifted	
	from X $^1\Sigma^+$ and 2 $^1\Sigma^+$ at $\gamma=180^\circ$ with $r=r_{\rm e}.$	93
5.12	Vibronic couplings of H-CO ⁺ for $\gamma=0^\circ$ as functions of R connecting states	
	$\nu = 0 - 5$ with states $\nu' = \nu$ and $\nu \pm 1$	94
5.13	Vibronic couplings of H-CO ⁺ for $\gamma = 90^{\circ}$ as functions of R connecting states	
	$\nu = 0 - 5$ with states $\nu' = \nu$ and $\nu \pm 1$	95
5.14	Vibronic couplings of H-CO ⁺ for $\gamma=180^\circ$ as functions of R connecting states	
	$\nu = 0 - 5$ with states $\nu' = \nu$ and $\nu \pm 1$	96
5.15	State-to-state cross sections of $H^+ + CO(\nu = 0) \rightarrow H + CO^+(\nu' = 0 - 5)$ for	
	$\gamma=0^\circ,90^\circ,180^\circ,$ and angle-averaged	102
5.16	Angle-averaged state-to-state cross sections of H ⁺ + CO(ν = 0) \rightarrow H +	
	$CO^{+}(\nu' = 0 - 8)$ for 9.96 eV/u and 1001.50 eV/u	103
5 17	State-to-state cross sections of H ⁺ collisions with $CO(u)$ for $\gamma = 0^{\circ}$	104

5.18	State-to-state cross sections of H ⁺ collisions with $CO(\nu)$ for $\gamma = 90^{\circ}$	105
5.19	State-to-state cross sections of H ⁺ collisions with CO(ν) for $\gamma=180^{\circ}$	106
5.20	Angle-averaged state-to-state cross sections of $H^+ + CO(\nu) \rightarrow H + CO^+(\nu' = 0)$	
	0-6)	107
5.21	Initial state-selective cross sections of H ⁺ collisions with CO ($\gamma = 0^{\circ}$) for	
	initial states of $\nu = 0 - 10$	108
5.22	Initial state-selective cross sections of H ⁺ collisions with CO ($\gamma=90^{\circ}$) for	
	initial states of $\nu = 0 - 10$	109
5.23	Initial state-selective cross sections of H ⁺ collisions with CO ($\gamma=180^{\circ}$) for	
	initial states of $\nu = 0 - 10$	110
5.24	Angle-averaged initial state-selective cross sections of H ⁺ collisions with CO	
	for initial states of $\nu = 0 - 10$	111
5.25	Angle-averaged state-to-state cross sections of H + CO ⁺ (ν') \rightarrow H ⁺ + CO(ν =	
	0-6)	112
5.26	Angle-averaged state-to-state cross sections of H + CO ⁺ ($\nu' = 0$) \rightarrow H ⁺ +	
	$CO(\nu=0-10)$ 10.06 eV/u and at 1001.03 eV/u	113
5.27	Initial state-selective cross sections of H collisions with CO ⁺ ($\gamma = 0^{\circ}$) for	
	initial states of $\nu' = 0 - 8$	114
5.28	Initial state-selective cross sections of H collisions with CO ⁺ ($\gamma = 90^{\circ}$) for	
	initial states of $\nu' = 0 - 8$	115
5.29	Initial state-selective cross sections of H collisions with CO ⁺ ($\gamma = 180^{\circ}$) for	
	initial states of $\nu' = 0 - 8$	116
5.30	Angle-averaged initial state-selective cross sections of H collisions with $\mathrm{CO^{+}}$	
	for initial states of $\nu' = 0 - 8$	117
5.31	Orientation-angle-averaged and -dependent total cross sections for the colli-	
	sions of H ⁺ with CO compared with previous theoretical and experimental	
	data	118

5.32	Orientation-angle-averaged and -dependent total cross sections for the colli-	
	sions of H with CO^+	119
В.1	A rotation about the z-axis by an angle α	133
B.2	A rotation about the y_1 -axis by an angle β	133
В.3	A rotation about the z_2 -axis by an angle γ	134

LIST OF TABLES

3.1	Comparison of asymptotic separated-atom energies between the MRD-CI cal-	
	culations and experiments for the eight molecular states of $\mathrm{NH^+}.$	35
3.2	Rate coefficients for electron capture from collisions of N with H^+ and N^+	
	with H	47
4.1	Parameters of long-range potentials for 1 $^2\Sigma^+,$ 1 $^2\Pi,$ and 2 $^2\Sigma^+$ corresponding	
	to Eqs. (4.5) and (4.6)	53
4.2	Comparison of asymptotic separated-atom energies between the MRD-CI cal-	
	culations and experiment for the lowest three molecular states of Na-He. $$	53
4.3	Fitting parameters of inelastic rate coefficients for Na(3s \rightarrow 3p) excitation	
	and $Na(3p \rightarrow 3s)$ quenching due to collisions with He and H	60

Chapter 1

Introduction

Living in a world constructed from atomic and molecular building blocks, the understanding of a variety of macroscopic and microscopic phenomena due to colliding atoms and molecules is of considerable importance and interest. Collisions between ions, atoms, and molecules play crucial roles in a wide range of applications, such as the early Universe, the interstellar medium, planetary atmospheres, fusion energy, and radiotherapy.

In the review by Lepp et al. [1], it was highlighted that atomic and molecular processes control the evolution of the Universe, and are also important probes for our understanding of it. Due to the low-density of interstellar space, microphysical processes, such as collisional ionization or charge transfer, govern most physical and chemical phenomena within an astronomical plasma. In modern computational astrophysics, a large-scale numerical simulation of astronomical spectra, such as with the code CLOUDY [2], requires large quantities of atomic and molecular data. With the precise rate coefficients provided by atomic and molecular scattering calculations, the spectral synthesis through a numerical simulation is able to compare with and to interpret the observed spectrum on a quantitative basis. In particular, with improvements in telescope detector technology, comes unprecedented advancement in astronomical observational resolution and sensitivity which realizes the investigation of the atmospheres of extrasolar planets and other objects. Through the observation of absorption spectrum and the theoretical study of a variety of collisional mechanisms, it is possible to reveal the physical conditions in the atmospheres of extrasolar planets. Besides planets, another interesting phenomena, X-ray emission, occurring in cometary atmospheres has also

drawn a great deal of attention. Since X-ray emission in space is generally thought to originate from hot collisional plasmas, it is surprising to discover strong X-ray emission from cold cometary atmospheres. To explain such a particular circumstance, charge exchange processes occurring at the interface of the coma and solar wind are major mechanisms.

In addition to implications to astrophysics, research in controlled fusion to produce energy also counts on the availability of accurate atomic and molecular data. Cross-section data for ion-atom collision processes play crucial roles in the edge plasma of magnetic confinement fusion devices, such as Tokamaks, in which a critical ion-atom collision process occurring in the edge plasma is charge transfer. Another practical application is relevant to ion-based radiotherapy. The interactions of ions with biomolecules, such as DNA, are responsible for biological radiation damage processes. The electron capture of the RNA base uracil by collisions of C^{q+} ions [3] had been studied to understand the ionization and fragmentation dynamics of uracil. However, as mentioned in [4], theoretical studies are sparse. More calculations of ion-biomolecule collisions are needed in order to have a better understanding of the damage mechanisms of biomolecules.

In atomic collisions, theoretical methods can be categorized as perturbative or nonperturbative. For high-energy collisions, where the projectile velocity is much larger than
the velocity of the orbital electron in the target, the ionization channel is a dominant process. Generally, it's believed that the perturbative approach is valid for this circumstance. In
contrast, due to many inelastic channels, strongly coupled together, and being nearly impossible to single out a dominant channel, a non-perturbative method such as the close-coupling
approach is taken to be an appropriate description for low- to intermediate-energy collisions.
According to the treatment of nuclear motion, the close-coupling method can be divided into
a semiclassical model and a quantum-mechanical description. In a semiclassical formalism,
the motion of nuclei can be described by a classical trajectory for collisions where the de
Broglie wavelength of the projectile is much less than the typical interaction range, while
electronic wave functions are governed by the time-dependent Schrödinger equation. The

merits of a semiclassical representation are that it provides an intrinsically simple picture of the collision dynamics and reduces the complexity of computations. However, its disadvantage is the neglect of the quantum effects of nuclear motion, which might be critical at low energies. For a quantum mechanical approach, both nuclei and electrons are treated fully in a quantal description. Although the difficulty of numerical calculation increases, taking advantage of the fully quantal method to perform close-coupling computations becomes available with the advanced technology of high-speed computing.

In close-coupling methods, the wave function is expressed by an expansion of a set of basis functions. There are two types of basis functions that are commonly used. One is the atomic orbital (AO) method and the other is the molecular orbital (MO) method. The AO method is believed to be an appropriate description of intermediate-energy collisions. Each atomic orbital is located at the target or projectile such that the atomic characteristics are retained throughout the collision. It is obvious that the atomic-orbital expansion approach is valid for large internuclear separations, but is incapable of providing an accurate description for small internuclear separations which is important for slow collisions. On the contrary, the molecular-orbital expansion approach is more appropriate for describing slow collisions. The concept of the molecular orbital is based on work by Hund [5] and Mulliken [6]. In 1929, the paper by Lennard-Jones [7] was the first one to treat molecular orbital theory in a quantitative way. Although the MO model provides a better treatment for slow collisions than the AO model, the MO method has intrinsic problems in which the correct asymptotic boundary conditions of the scattering wave function are not fulfilled and the Galilean invariance of the coupled equations is violated. To avoid these defects, the so-called electron translation factor (ETF) had been introduced to remove the difficulties associated with the conventional MO method [8, 9].

The major focus of my investigations is aimed at the inelastic collision processes of charge transfer, quenching, and excitation to promote the modeling of interstellar gas and planetary atmospheres going beyond standard assumptions of thermodynamic equilibrium.

In addition, an investigation of elastic atom-atom collisions for ultra-low energies is carried out to explore the characteristics of scattering lengths. The calculations of ion-atom or atomatom collisions are based on the perturbed stationary state (PSS) model in which the basis functions are constructed by the molecular orbitals, or so-called molecular-orbital close-coupling (MOCC) method. The PSS approximation was devised by Mott with the aim of treating slow encounters between atomic systems [10]. In an excellent review article of slow atomic collisions by Delos [8], the PSS theory and its problems are discussed in great detail. A complete description of the MOCC method is given in the book of Bransden and McDowell [9].

We adopt the quantum-mechanical MOCC method neglecting ETFs to investigate the different collision systems, which include ion-atom, atom-atom, and ion-molecule collisions. For a practical application of ion-atom collisions, we study charge exchange processes for collisions of nitrogen with protons and singly ionized nitrogen with hydrogen. The results are helpful to elucidate the discrepancy between observed and predicted emission line ratios of N to N⁺ in Seyfert 2 galaxies and provide a comparison of rate coefficients due to radial and rotational couplings with spin-orbit coupling.

As an application to atom-atom collisions, the interaction of sodium with helium has been studied from thermal energies to the ultracold. Rate coefficients for collisional excitation and de-excitation of sodium due to helium collisions at thermal energies are useful for the clarification of whether or not non-local thermodynamic equilibrium (NLTE) effects can account for the magnitude of sodium absorption in the extrasolar giant planet (EGP) HD 209458b. The level populations of atoms are determined by the rates of all collisional processes, such as excitation and de-excitation, and radiative processes, such as photoabsorption, spontaneous and stimulated emission. Local thermodynamic equilibrium (LTE) is valid for cases in which all transitions are dominated by collisional rates. For a gas in LTE, the level populations for each species are obtained by the Saha-Boltzmann distribution and are related to the gas temperature when the density is sufficiently large. If the collisional

rates are small or the density is below some critical value and radiative rates are large, LTE doesn't hold. Extending to ultra-low energies, scattering lengths become dominant physical quantities for the study of collisions. The variation of the scattering length with the reduced mass of the system provides a test of the sensitivity of the scattering length to the potential. The relation between the scattering length and bound states of the collision complex is explored.

In the early 1970s, rotational excitation due to molecular collisions had drawn considerable attention. Based on a rigid rotator model, a set of close-coupling equations devised by Arthurs and Dalgarno [11] was widely applied to the study of rotational transitions in scattering problems [12, 13]. Due to the complexity arising from the molecular rotational degree of freedom, many efforts were made to simplify the angular momentum coupling. The "sudden approximation" [14, 15], which is a time-scale criterion based on the assumption of an slow internal degree of freedom compared to the time scale or "suddenness" of the collision event, is widely used in the treatment of inelastic molecular collisions. Taking advantage of the development of the sudden approximation in rotational transitions of molecular collisions, most investigations for vibronic transitions of ion-molecule collisions are performed within the framework of the infinite order sudden approximation (IOSA). The IOSA is actually an approach comprising the energy sudden approximation (ESA) and the centrifugal sudden approximation (CSA). When the collision time of a projectile is much smaller than molecular rotational periods, one could use the ESA to simplify the rotational motion of molecular targets. The criterion of using the CSA requires that the radial relative motion of the projectile is much faster compared to its angular relative motion. The detailed description of ESA, CSA, and IOSA can be found in the articles of Sidis [16] and Baer [17].

Within the framework of IOSA, we extend the quantal MOCC approach to investigate ion-molecule collisions and apply it to charge transfer processes due to proton collisions with CO. Since the solar wind is primarily composed of protons, its interaction with planetary atmospheres or cometary comas is dominated by charge exchange processes due to atomic

or molecular collisions with protons. X-ray emission is usually considered to result from hot collisional plasmas. In 1996, it was surprising that X-ray emission was discovered in comet Hyakutake [18] because cometary atmospheres are cold. It becomes an interesting topic to understand the mechanism of X-ray emission from comets [19], and charge exchange processes occurring in the interface between the solar wind and cometary atmospheres. Since CO is an important molecule in a variety of astrophysical objects and a comet is a mixture of frozen H₂O and CO, collisions of CO with protons are believed to be of importance in many different astronomical environments. Taking advantage of the IOSA approach, we take into account the vibrational motion of target molecule and study the vibrationally-resolved charge transfer due to CO collisions with protons and CO⁺ collisions with H. The orientation angle-dependent cross sections explicitly illustrate the steric effect in ion-molecule collisions.

In Chapter 2, a detailed discussion of the MOCC method includes the coupled-channel equations in the adiabatic and diabatic representation, adiabatic-diabatic transformation, partial wave analysis, S-matrix, and IOSA approach. Three applications based on the quantal MOCC and IOSA methods for ion-atom, atom-atom, and ion-molecule collisions are presented in Chapters 3-5, respectively. In Chapter 6, a summary of present investigations and an outlook of future research directions are given.

Chapter 2

THE SCATTERING THEORY

2.1 Coupled-channel equations in the adiabatic representation

The Hamiltonian, H, of a system of two nuclei A and B with masses M_A and M_B , respectively, separated by a vector \mathbf{R} and one electron with a position vector \mathbf{s} with respect to the center of mass of the nuclei, is given in atomic units by

$$H = -\frac{1}{2\mu}\nabla_{\mathbf{R}}^2 - \frac{1}{2m}\nabla_{\mathbf{s}}^2 + V,$$
 (2.1)

where $\mu = M_A M_B/(M_A + M_B)$, $m = (M_A + M_B)m_e/(M_A + M_B + m_e) \simeq 1$ with $m_e = 1$ a.u., and V represents nucleus-nucleus and nucleus-electron Coulomb interactions. The total wave functions Ψ can be expanded in terms of adiabatic molecular orbitals $\psi_i(\mathbf{s}, \mathbf{R})$ as

$$\Psi = \sum_{j=1} \psi_j(\mathbf{s}, \mathbf{R}) F_j(\mathbf{R}). \tag{2.2}$$

The adiabatic molecular orbitals $\psi_j(\mathbf{s}, \mathbf{R})$ are solutions of the Schrödinger equation for the one-electron system,

$$\left[-\frac{1}{2} \nabla_{\mathbf{s}}^2 + V - \varepsilon_j(R) \right] \psi_j(\mathbf{s}, \mathbf{R}) = 0, \tag{2.3}$$

and satisfy the orthonormality condition,

$$\int \psi_i^*(\mathbf{s}, \mathbf{R}) \psi_j(\mathbf{s}, \mathbf{R}) d\mathbf{s} = \delta_{ij}. \tag{2.4}$$

 $\varepsilon_j(R)$ in Eq (2.3) is an eigenvalue of the one-electron system and also an electronic potential curve for the nuclear motion which varies parametrically with R.

From the Schrödinger equation,

$$H\Psi = E\Psi, \tag{2.5}$$

taking advantage of the variational method, the coupled equations for channel functions $F_j(\mathbf{R})$ are provided by

$$\int \psi_i^*(\mathbf{s}, \mathbf{R})[H - E]\Psi(\mathbf{s}, \mathbf{R})d\mathbf{s} = 0.$$
(2.6)

where E is the total energy and i = 1, 2, ...N. Then with the use of Eqs. (2.1) and (2.2) (see Appendix A), we obtain

$$[\nabla_{\mathbf{R}}^2 + k_i^2] F_i(\mathbf{R}) = \sum_{j=1}^{N} [M_{ij}(\mathbf{R}) + \mathbf{P}_{ij}(\mathbf{R}) \cdot \nabla_{\mathbf{R}}] F_j(\mathbf{R})$$
(2.7)

where $k_i^2 = -2\mu(\varepsilon_i(R) - E)$, while $M_{ij}(\mathbf{R})$ and $\mathbf{P}_{ij}(\mathbf{R})$ are defined as

$$M_{ij}(\mathbf{R}) = -\int \psi_i^*(\mathbf{s}, \mathbf{R}) \nabla_{\mathbf{R}}^2 \psi_j(\mathbf{s}, \mathbf{R}) d\mathbf{s}$$
 (2.8)

and

$$\mathbf{P}_{ij}(\mathbf{R}) = -2 \int \psi_i^*(\mathbf{s}, \mathbf{R}) \nabla_{\mathbf{R}} \psi_j(\mathbf{s}, \mathbf{R}) d\mathbf{s}.$$
 (2.9)

Eq. (2.7) is the perturbed stationary state equation obtained in molecular coordinates (\mathbf{s}, \mathbf{R}) [9].

The adiabatic molecular orbitals are usually calculated in the body-fixed frame of reference, in which the z'-axis is directed along the internuclear line between the two nuclei (see Fig. 2.1). The body-fixed frame is conventionally obtained from the space-fixed frame by three rotations with the three Euler angles, α , β , and γ (see Appendix B). Because of the symmetry with respect to the z'-axis in the body-fixed frame for this system, we set $\gamma = 0$ and denote $\alpha = \Phi$ and $\beta = \Theta$. Φ and Θ are the azimuthal and polar angles of \mathbf{R} in the space-fixed frame. The components (x', y', z') of position vectors \mathbf{r}' in the body-fixed frame can be expressed in terms of their components (x, y, z) of \mathbf{r} in the space-fixed frame through the following transformation:

$$\mathbf{r}' = R(\Theta, \Phi)\mathbf{r},\tag{2.10}$$

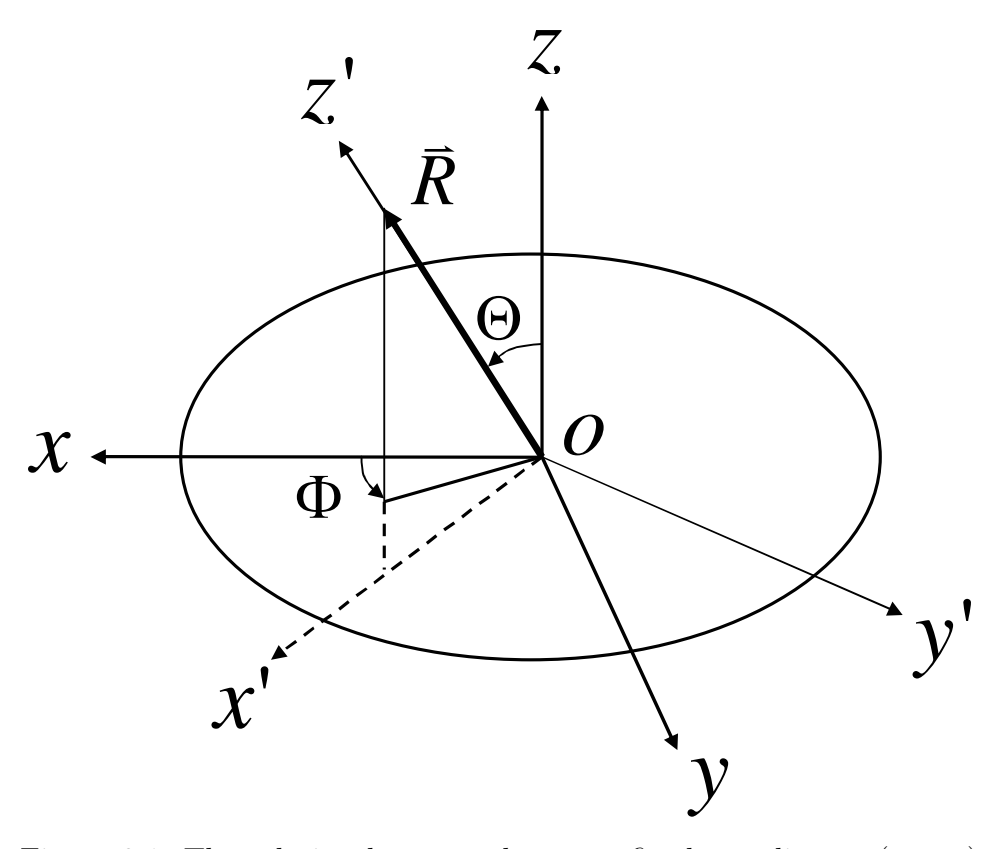


Figure 2.1: The relation between the space-fixed coordinates (x, y, z) and the body-fixed coordinates (x', y', z').

where

$$R(\Theta, \Phi) = \begin{pmatrix} \cos \Theta \cos \Phi & \cos \Theta \sin \Phi & -\sin \Theta \\ -\sin \Phi & \cos \Phi & 0 \\ \sin \Theta \cos \Phi & \sin \Theta \sin \Phi & \cos \Theta \end{pmatrix}. \tag{2.11}$$

Since **R** is along the z'-axis in the body-fixed frame, the adiabatic molecular orbitals $\psi_j(\mathbf{s}, \mathbf{R})$ in the space-fixed frame can be expressed as $\bar{\psi}_j(\mathbf{s}', R)$ in the body-fixed frame. In addition, because $R^TR = I$, the expression of the operator $\nabla_{\mathbf{s}'}^2$ in the body-fixed frame is the same as $\nabla_{\mathbf{s}}^2$ in the space-fixed frame except for replacing variables (x, y, z) by (x', y', z'). Taking advantage of this invariance, the formalism of the coupled equations, Eq. (2.7), is unaltered, but the molecular orbitals $\psi_j(\mathbf{s}, \mathbf{R})$ are replaced by $\bar{\psi}_j(\mathbf{s}', R)$, where the orbitals $\bar{\psi}_j(\mathbf{s}', R)$

satisfy

$$\left[-\frac{1}{2} \nabla_{\mathbf{s}'}^2 + V - \varepsilon_j(R) \right] \bar{\psi}_j(\mathbf{s}', R) = 0$$
 (2.12)

and

$$\bar{L}_z \bar{\psi}_j(\mathbf{s}', R) = \pm \lambda_j \bar{\psi}_j(\mathbf{s}', R), \tag{2.13}$$

where \bar{L}_z is the z-component of the electronic angular momentum in the body-fixed frame and $\lambda_j = 0, 1, 2, 3, ...$ referred to one-electron levels, σ , π , δ , and ϕ . Note that the molecular orbitals in the body-fixed frame depending on the magnitude of R. The wave function Ψ using the molecular orbitals in the body-fixed frame can be written as

$$\Psi = \sum_{j=1}^{N} \bar{\psi}_j(\mathbf{s}', R) F_j(\mathbf{R}), \qquad (2.14)$$

while

$$M_{ij}(R) = -\int \bar{\psi}_i^*(\mathbf{s}', R) \nabla_{\mathbf{R}}^2 \bar{\psi}_j(\mathbf{s}', R) d\mathbf{s}'$$
(2.15)

and

$$\mathbf{P}_{ij}(R) = -2 \int \bar{\psi}_i^*(\mathbf{s}', R) \nabla_{\mathbf{R}} \bar{\psi}_j(\mathbf{s}', R) d\mathbf{s}.$$
 (2.16)

According to Eqs. (2.10) and (2.11), \mathbf{s}' is not only a function of \mathbf{s} but also a function of Θ and Φ . This leads to

$$\frac{\partial}{\partial R}\bar{\psi}_{j}(\mathbf{s}',R) = \left[\frac{\partial'}{\partial R} + \frac{\partial x'}{\partial R}\frac{\partial}{\partial x'} + \frac{\partial y'}{\partial R}\frac{\partial}{\partial y'} + \frac{\partial z'}{\partial R}\frac{\partial}{\partial z'}\right]\bar{\psi}_{j}(\mathbf{s}',R),\tag{2.17a}$$

$$\frac{\partial}{\partial \Theta} \bar{\psi}_j(\mathbf{s}', R) = \left[\frac{\partial'}{\partial \Theta} + \frac{\partial x'}{\partial \Theta} \frac{\partial}{\partial x'} + \frac{\partial y'}{\partial \Theta} \frac{\partial}{\partial y'} + \frac{\partial z'}{\partial \Theta} \frac{\partial}{\partial z'} \right] \bar{\psi}_j(\mathbf{s}', R), \tag{2.17b}$$

$$\frac{\partial}{\partial \Phi} \bar{\psi}_j(\mathbf{s}', R) = \left[\frac{\partial'}{\partial \Phi} + \frac{\partial x'}{\partial \Phi} \frac{\partial}{\partial x'} + \frac{\partial y'}{\partial \Phi} \frac{\partial}{\partial y'} + \frac{\partial z'}{\partial \Phi} \frac{\partial}{\partial z'} \right] \bar{\psi}_j(\mathbf{s}', R), \tag{2.17c}$$

where $\frac{\partial'}{\partial R}$, $\frac{\partial'}{\partial \Theta}$, and $\frac{\partial'}{\partial \Phi}$ denote the derivatives taken with \mathbf{s}' held constant in the body-fixed frame. Using Eqs. (2.10) and (2.11), the derivatives with respect to R, Θ , and Φ in the

space-fixed frame (see Appendix C) can be expressed as

$$\frac{\partial}{\partial R}\bar{\psi}_{j}(\mathbf{s}',R) = \frac{\partial'}{\partial R}\bar{\psi}_{j}(\mathbf{s}',R), \qquad (2.18a)$$

$$\frac{\partial}{\partial \Theta}\bar{\psi}_{j}(\mathbf{s}',R) = \left[\frac{\partial'}{\partial \Theta} - i\bar{L}_{y}\right]\bar{\psi}_{j}(\mathbf{s}',R)$$

$$= -i\bar{L}_{y}\bar{\psi}_{j}(\mathbf{s}',R), \qquad (2.18b)$$

$$\frac{\partial}{\partial \Phi}\bar{\psi}_{j}(\mathbf{s}',R) = \left[\frac{\partial'}{\partial \Phi} - i\cos\Theta\bar{L}_{z} + i\sin\Theta\bar{L}_{x}\right]\bar{\psi}_{j}(\mathbf{s}',R)$$

$$= -i\cos\Theta\bar{L}_{z}\bar{\psi}_{j}(\mathbf{s}',R) + i\sin\Theta\bar{L}_{x}\bar{\psi}_{j}(\mathbf{s}',R), \qquad (2.18c)$$

where \bar{L}_x , \bar{L}_y , and \bar{L}_z are defined as the components of electronic angular momentum in the body-fixed frame, and follow the commutation relations,

$$[\bar{L}_i, \bar{L}_j] = i\epsilon_{ijk}\bar{L}_k, \tag{2.19}$$

where ϵ_{ijk} is the Levi-Civita or permutation tensor of rank 3. With the help of Eq. (2.18), the gradient of $\bar{\psi}_j(\mathbf{s}', R)$ with respect to R, Θ , and Φ can be evaluated and $\mathbf{P}_{ij}(R)$ can be expressed as

$$\mathbf{P}_{ij}(R) = -2\left\{\hat{R}\langle i|\frac{\partial'}{\partial R}|j\rangle + \hat{\Theta}\frac{-i}{R}\langle i|\bar{L}_y|j\rangle + \hat{\Phi}\left[\frac{-i\cot\Theta}{R}\lambda_j\delta_{ij} + \frac{i}{R}\langle i|\bar{L}_x|j\rangle\right]\right\}.$$
(2.20)

The notation $\langle i|O|j\rangle$, in which O is an arbitary operator, is defined as

$$\langle i|O|j\rangle \equiv \int \bar{\psi}_j^*(\mathbf{s}', R)O\bar{\psi}_j(\mathbf{s}', R)d\mathbf{s}'.$$
 (2.21)

Then we immediately obtain that

$$\mathbf{P}_{ij}(R) \cdot \nabla_{\mathbf{R}} = -2\langle i|\frac{\partial}{\partial R}|j\rangle \frac{\partial}{\partial R} + i\frac{2}{R^2}\langle i|\bar{L}_y|j\rangle \frac{\partial}{\partial \Theta} -i\frac{2}{R^2\sin\Theta} \left[\langle i|\bar{L}_x|j\rangle - \cot\Theta\lambda_j\delta_{ij}\right] \frac{\partial}{\partial \Phi},$$
 (2.22)

where we use the fact of Eq. (2.18a).

Similarily,

$$M_{ij}(R) = -\langle i|\frac{\partial^2}{\partial R^2} + \frac{2}{R}\frac{\partial}{\partial R}|j\rangle + \frac{1}{R^2}\langle i|\bar{L}_x^2 + \bar{L}_y^2|j\rangle - \frac{2\cot\Theta}{R^2}\lambda_j\langle i|\bar{L}_x|j\rangle + \frac{\cot^2\Theta}{R^2}\lambda_j^2\delta_{ij}.$$
(2.23)

Combining Eqs. (2.22) and (2.23), the terms on the right hand side of Eq. (2.7) are given in the following form:

$$M_{ij}(R) + \mathbf{P}_{ij}(R) \cdot \nabla_{\mathbf{R}} = \frac{1}{R^2 \sin^2 \Theta} \left[\lambda_j^2 \cos^2 \Theta + i2\lambda_j \cos \Theta \frac{\partial}{\partial \Phi} \right] \delta_{ij}$$

$$+ \langle i| - \frac{\partial^2}{\partial R^2} - \frac{2}{R} \frac{\partial}{\partial R} + \frac{\bar{L}_x^2 + \bar{L}_y^2}{R^2} |j\rangle$$

$$- 2\langle i| \frac{\partial}{\partial R} |j\rangle \frac{\partial}{\partial R} + \frac{2}{R^2} \left[i\langle i|\bar{L}_y|j\rangle \frac{\partial}{\partial \Theta} - i\frac{\langle i|\bar{L}_x|j\rangle}{\sin \Theta} \frac{\partial}{\partial \Phi} - \lambda_j \langle i|\bar{L}_x|j\rangle \cot \Theta \right]. \tag{2.24}$$

For the left hand side of Eq. (2.7), the operator $\nabla_{\mathbf{R}}^2$ can be expressed in spherical polar coordinates as

$$\nabla_{\mathbf{R}}^{2} = \frac{\partial^{2}}{\partial R^{2}} + \frac{2}{R} \frac{\partial}{\partial R} + \frac{1}{R^{2}} \left[\frac{\partial^{2}}{\partial \Theta^{2}} + \cot \Theta \frac{\partial}{\partial \Theta} + \frac{1}{\sin^{2} \Theta} \frac{\partial^{2}}{\partial \Phi^{2}} \right]. \tag{2.25}$$

Thus, based on Eqs. (2.24) and (2.25), Eq. (2.7) can be written as

$$\left\{ \frac{\partial^{2}}{\partial R^{2}} + \frac{1}{R^{2}} \left[\frac{\partial^{2}}{\partial \Theta^{2}} + \cot \Theta \frac{\partial}{\partial \Theta} + \frac{1}{\sin^{2}\Theta} \left(\frac{\partial}{\partial \Phi} - i\lambda_{i} \cos \Theta \right)^{2} \right] + k_{i}^{2} \right\} RF_{i}(\mathbf{R})
= \sum_{j=1}^{N} \left\{ \langle i| - \frac{\partial^{2}}{\partial R^{2}} + \frac{\bar{L}_{x}^{2} + \bar{L}_{y}^{2}}{R^{2}} |j\rangle - 2\langle i| \frac{\partial}{\partial R} |j\rangle \frac{\partial}{\partial R} \right. (2.26)
+ \frac{2}{R^{2}} \left[i\langle i|\bar{L}_{y}|j\rangle \frac{\partial}{\partial \Theta} - i\frac{\langle i|\bar{L}_{x}|j\rangle}{\sin\Theta} \frac{\partial}{\partial \Phi} - \lambda_{j}\langle i|\bar{L}_{x}|j\rangle \cot\Theta \right] \right\} RF_{j}(\mathbf{R}).$$

Furthermore, we can define

$$\mathbf{J}_{i}^{2} = -\left[\frac{\partial^{2}}{\partial\Theta^{2}} + \cot\Theta\frac{\partial}{\partial\Theta} + \frac{1}{\sin^{2}\Theta}\left(\frac{\partial}{\partial\Phi} - i\lambda_{i}\cos\Theta\right)^{2} - \lambda_{i}^{2}\right],\tag{2.27}$$

as well as the radial coupling $V_{ij}^R(R)$ and the rotational (Coriolis) coupling $V_{ij}^C(R)$ as

$$V_{ij}^{R}(R) = \left[\langle i| - \frac{\partial^{2}}{\partial R^{2}} + \frac{\bar{L}_{x}^{2} + \bar{L}_{y}^{2}}{R^{2}} |j\rangle - 2\langle i| \frac{\partial}{\partial R} |j\rangle \frac{\partial}{\partial R} \right] \delta_{\lambda_{i},\lambda_{j}}, \tag{2.28}$$

and

$$V_{ij}^{C}(R) = \frac{2}{R^{2}} \left[i \langle i | \bar{L}_{y} | j \rangle \frac{\partial}{\partial \Theta} - i \frac{\langle i | \bar{L}_{x} | j \rangle}{\sin \Theta} \frac{\partial}{\partial \Phi} - \lambda_{j} \langle i | \bar{L}_{x} | j \rangle \cot \Theta \right]. \tag{2.29}$$

It is worth noticing that in $V_{ij}^R(R)$, operators $\bar{L}_x^2 + \bar{L}_y^2$ which can be expressed in terms of the ladder operators,

$$\bar{L}_{+} \equiv \bar{L}_{x} + i\bar{L}_{y},\tag{2.30}$$

and

$$\bar{L}_{-} \equiv \bar{L}_{x} - i\bar{L}_{y},\tag{2.31}$$

so that

$$\bar{L}_x^2 + \bar{L}_y^2 = \frac{1}{2}(\bar{L}_+\bar{L}_- + \bar{L}_-\bar{L}_+),$$
(2.32)

connects states with the same values of λ . The rest of the terms including $\frac{\partial}{\partial R}$ and $\frac{\partial^2}{\partial R^2}$ are also zero for states with different values of λ , because $\bar{\psi}_j(\mathbf{s}', R)$, an eigenfunction of \bar{L}_z with the eigenvalue λ_j , can be formally written as

$$\bar{\psi}_i(\mathbf{s}', R) = A_i(r', \theta', R)e^{i\lambda_j \phi'}, \tag{2.33}$$

where r', θ' , and ϕ' are components of \mathbf{s}' in spherical polar coordinates, and

$$\int_0^{2\pi} e^{i(\lambda_j - \lambda_i)\phi'} d\phi' = 2\pi \delta_{\lambda_i, \lambda_j}.$$
(2.34)

Consequently, the radial coupling $V_{ij}^R(R)$ becomes zero if states that it connects have different values of λ . Using the definitions of Eqs. (2.27), (2.28), and (2.29), Eq. (2.27) can be simply written as

$$\left\{ \frac{\partial^2}{\partial R^2} - \frac{\mathbf{J}_i^2 - \lambda_i^2}{R^2} + k_i^2 \right\} RF_i(\mathbf{R}) = \sum_{j=1}^N [V_{ij}^R(R) + V_{ij}^C(R)] RF_j(\mathbf{R}).$$
(2.35)

2.2 Coupled-Channel equations in a diabatic representation

In the coupled equations of channel functions $F_j(\mathbf{R})$, the radial coupling V_{ij}^R includes three terms, $-2\langle i|\frac{\partial}{\partial R}|j\rangle\frac{\partial}{\partial R}$, $-\langle i|\frac{\partial^2}{\partial R^2}|j\rangle$ and $\langle i|\frac{\bar{L}_x^2+\bar{L}_y^2}{R^2}|j\rangle$. We introduce matrix elements $A_{ij}(R)$ and $B_{ij}(R)$, which are defined as

$$A_{ij}(R) \equiv \langle i | \frac{\partial}{\partial R} | j \rangle \tag{2.36}$$

and

$$B_{ij}(R) \equiv \langle i|\frac{\partial^2}{\partial R^2}|j\rangle.$$
 (2.37)

The Hellman-Feynman theorem [20] enables us to express $A_{ij}(R)$ in the form

$$A_{ij}(R) = \begin{cases} -\frac{1}{\varepsilon_i(R) - \varepsilon_j(R)} \langle i | \frac{\partial V}{\partial R} | j \rangle, & i \neq j \\ 0, & i = j. \end{cases}$$
 (2.38)

It is obvious that the matrix with elements of $A_{ij}(R)$ is skew symmetric, $A_{ij} = -A_{ji}$, due to Eq. (2.38) and since $A_{ij}(R)$ is real. Due to the Wigner-von Neumann non-crossing rule [21], adiabatic states, i and j, with the same symmetry will never cross each other, i.e. $\varepsilon_i(R) \neq \varepsilon_j(R)$ for any value of R. However, it is posssible that two states approach each other in a narrow region of R to make a so-called avoided-crossing. In the case of an avoided-crossing, the $A_{ij}(R)$ is nearly singular or changes vary rapidly near the avoiding-crossing. This behavior can cause difficulties when numerical methods, such as finite-differencing, are used. In order to overcome this problem, one way is to use a diabatic basis instead of the adiabatic basis. The idea is to make a unitary transformation for adiabatic molecular orbitals and channel functions such that $A_{ij}(R)$ in the diabatic representation becomes zero.

Given a unitary matrix with elements $C_{ij}(R)$, the transformation for adiabatic molecular orbitals $\bar{\psi}_i(\mathbf{s}', R)$ into diabatic orbitals $\bar{\psi}_j^d(\mathbf{s}', R)$ is given by

$$\bar{\psi}_j^d(\mathbf{s}', R) = \sum_i \bar{\psi}_i(\mathbf{s}', R) C_{ij}(R). \tag{2.39}$$

Since the expansion of the total wave function Ψ in the adiabatic basis is equivalent to the expansion in the diabatic basis, we obtain

$$\sum_{i} \bar{\psi}_{i}(\mathbf{s}', R) F_{i}(\mathbf{R}) = \sum_{j} \bar{\psi}_{j}^{d}(\mathbf{s}', R) G_{j}(\mathbf{R}), \qquad (2.40)$$

where $G_j(\mathbf{R})$ are channel functions in the diabatic representation. Substituting Eq. (2.39) for $\bar{\psi}_j^d(\mathbf{s}', R)$ in Eq. (2.40) leads to

$$\sum_{i} \bar{\psi}_{i}(\mathbf{s}', R) F_{i}(\mathbf{R}) = \sum_{j} \sum_{i} \bar{\psi}_{i}(\mathbf{s}', R) C_{ij}(R) G_{j}(\mathbf{R})$$
$$= \sum_{i} \bar{\psi}_{i}(\mathbf{s}', R) \sum_{j} C_{ij}(R) G_{j}(\mathbf{R}). \tag{2.41}$$

Therefore, the transformation of channel functions is given by

$$F_i(\mathbf{R}) = \sum_j C_{ij}(R)G_j(\mathbf{R}). \tag{2.42}$$

To ensure that the symmetries are preserved in the diabatic representation, the transformation only combines the adiabatic molecular orbitals with the same symmetry, *i.e.* adiabatic σ orbitals transform to diabatic σ orbitals only. Since the symmetries are preserved, the coupled equations in the diabatic representation can be obtained from the same procedure as discussed previously. It is worth noticing that

$$\int d\mathbf{s}' \bar{\psi}_i^*(\mathbf{s}', R) \left[-\frac{1}{2} \nabla_{\mathbf{s}'}^2 + V \right] \bar{\psi}_j(\mathbf{s}', R)$$
(2.43)

gives $\varepsilon_j(R)\delta_{ij}$ in the adiabatic basis. It indicates that there is no contribution of the integral from terms with $i \neq j$. However, the same integral in the diabatic basis could have terms with $i \neq j$.

In Eq. (2.43), substituting the diabatic orbitals $\bar{\psi}_i^d(\mathbf{s}', R)$ for the adiabatic molecular orbitals $\bar{\psi}_j(\mathbf{s}', R)$, we obtain

$$U_{ij}(R) = \int d\mathbf{s}' \bar{\psi}_i^{d*}(\mathbf{s}', R) \left[-\frac{1}{2} \nabla_{\mathbf{s}'}^2 + V \right] \bar{\psi}_j^d(\mathbf{s}', R). \tag{2.44}$$

From Eq. (2.39) and the result of the integral (2.43), the expression for $U_{ij}(R)$ becomes

$$U_{ij}(R) = \sum_{k} C_{ik}^{\dagger}(R) \varepsilon_k(R) C_{kj}(R). \tag{2.45}$$

Because $k_i^2 = -2\mu(\varepsilon_i(R) - E)$, we can replace $\varepsilon_k(R)$ in Eq. (2.45) with $-\frac{k_k^2}{2\mu} + E$. Thus, the relation between $U_{ij}(R)$ and k_k^2 is given by

$$-2\mu U_{ij}(R) + 2\mu E \delta_{ij} = \sum_{k} C_{ik}^{\dagger}(R) k_k^2(R) C_{kj}(R).$$
 (2.46)

Using the expansion of Ψ in terms of the diabatic basis and the definition of $U_{ij}(R)$ in Eq. (2.44), the coupled-channel equations in the diabatic representation are expressed as

$$\sum_{j=1}^{N} \left\{ \left[\frac{\partial^2}{\partial R^2} - \frac{\mathbf{J}_i^2 - \lambda_i^2}{R^2} \right] \delta_{ij} - 2\mu U_{ij}(R) + 2\mu E \delta_{ij} \right\} RG_j(\mathbf{R})$$

$$= \sum_{j=1}^{N} \left[{}^d V_{ij}^R(R) + {}^d V_{ij}^C(R) \right] RG_j(\mathbf{R}), \tag{2.47}$$

where ${}^dV_{ij}^R(R)$ and ${}^dV_{ij}^C(R)$ are the radial and rotational coupling, respectively. The ${}^dV_{ij}^R(R)$ and ${}^dV_{ij}^C(R)$ have exactly the same form as $V_{ij}^R(R)$ and $V_{ij}^C(R)$ of the coupled-channel equations in the adiabatic basis states, but are taken with respect to the diabatic basis states.

2.3 Adiabatic-diabatic transformation

For the coupled-channel equations in the diabatic basis, we similarly denote $A_{ij}^d(R)$ and $B_{ij}^d(R)$ as matrix elements of the operators $\frac{\partial}{\partial R}$ and $\frac{\partial^2}{\partial R^2}$, respectively, which are parts of the radial coupling ${}^dV_{ij}^R(R)$, namely

$$A_{ij}^d(R) \equiv \langle i^d | \frac{\partial}{\partial R} | j^d \rangle \tag{2.48}$$

and

$$B_{ij}^d(R) \equiv \langle i^d | \frac{\partial^2}{\partial R^2} | j^d \rangle, \tag{2.49}$$

where $|i^d\rangle$ stands for the diabatic basis state *i*. Provided that the diabatic basis $|k^d\rangle$ is complete, we could insert an identity operator into Eq. (2.49) such that it can be written in terms of $A_{ij}^d(R)$ as

$$B_{ij}^{d}(R) = \langle i^{d} | \frac{\partial}{\partial R} \left[\sum_{k} |k^{d}\rangle \langle k^{d} | \frac{\partial}{\partial R} | j^{d}\rangle \right]$$
$$= \sum_{k} A_{ik}^{d}(R) A_{kj}^{d}(R) + \frac{d}{dR} A_{ij}^{d}(R). \tag{2.50}$$

From Eq. (2.48), the relation between $A_{ij}^d(R)$ and $A_{ij}(R)$ obtained using the transformation of Eq. (2.39) is given by

$$A_{ij}^{d}(R) = \sum_{kl} \langle k | C_{ki}^{*}(R) \frac{\partial}{\partial R} \left[C_{lj}(R) | l \rangle \right]$$

$$= \sum_{k} C_{ik}^{\dagger}(R) \frac{d}{dR} C_{kj}(R) + \sum_{kl} C_{ik}^{\dagger}(R) A_{kl}(R) C_{lj}(R)$$

$$= \sum_{k} C_{ik}^{\dagger}(R) \left[\frac{d}{dR} C_{kj}(R) + \sum_{l} A_{kl}(R) C_{lj}(R) \right]. \tag{2.51}$$

To ensure that $A_{ij}^d(R)$ vanishes, it is required, for each k,

$$\frac{d}{dR}C_{kj}(R) + \sum_{l} A_{kl}(R)C_{lj}(R) = 0.$$
 (2.52)

In addition, $B_{ij}^d(R)$ will vanish as well by Eq. (2.50) as long as the basis is a complete set. Therefore, the solution of Eq. (2.52) gives the unitary transformation to obtain the diabatic basis states. To solve Eq. (2.52), we adopt the boundary condition,

$$\lim_{R \to \infty} C_{ij}(R) = \delta_{ij}, \tag{2.53}$$

in order to let $U_{ij}(R)$ in Eq. (2.45) approach the eigenvalues ε_i of the adiabatic molecular orbitals, *i.e.*

$$U_{ij}(R \to \infty) = \varepsilon_i(R \to \infty)\delta_{ij}. \tag{2.54}$$

The differential equation (2.52), together with the boundary condition (2.53) can be summarized in one integral equation, namely

$$C_{ij}(R) = \delta_{ij} + \sum_{k} \int_{R}^{\infty} A_{ik}(R') C_{kj}(R') dR'.$$
 (2.55)

The solution of this integral equation can be obtained by iteration:

$$C_{ij}(R) = \delta_{ij} + \int_{R}^{\infty} dR_1 A_{ij}(R_1) + \sum_{k} \int_{R}^{\infty} dR_1 A_{ik}(R_1) \int_{R_1}^{\infty} dR_2 A_{kj}(R_2) + \sum_{kl} \int_{R}^{\infty} dR_1 A_{ik}(R_1) \int_{R_1}^{\infty} dR_2 A_{kl}(R_2) \int_{R_2}^{\infty} dR_3 A_{lj}(R_3) + \dots$$
 (2.56)

For the two-state case, the matrix of A(R) with elements $A_{ij}(R)$ is represented by

$$A(R) = \begin{pmatrix} 0 & A_{12}(R) \\ -A_{12}(R) & 0 \end{pmatrix}. \tag{2.57}$$

With $A_{ij}(R)$ given, the solution of $C_{ij}(R)$ can be written explicitly as

$$C_{11} = C_{22}$$

$$= 1 - \int_{R}^{\infty} dR_{1} A_{12}(R_{1}) \int_{R_{1}}^{\infty} dR_{2} A_{12}(R_{2})$$

$$+ \int_{R}^{\infty} dR_{1} A_{12}(R_{1}) \int_{R_{1}}^{\infty} dR_{2} A_{12}(R_{2}) \int_{R_{2}}^{\infty} dR_{3} A_{12}(R_{3}) \int_{R_{3}}^{\infty} dR_{4} A_{12}(R_{4})$$

$$+ \dots$$

$$= 1 - \frac{1}{2} \int_{R}^{\infty} dR_{1} A_{12}(R_{1}) \int_{R}^{\infty} dR_{2} A_{12}(R_{2})$$

$$+ \frac{1}{4!} \int_{R}^{\infty} dR_{1} A_{12}(R_{1}) \int_{R}^{\infty} dR_{2} A_{12}(R_{2}) \int_{R}^{\infty} dR_{3} A_{12}(R_{3}) \int_{R}^{\infty} dR_{4} A_{12}(R_{4})$$

$$+ \dots$$

$$= \cos \omega(R)$$

$$(2.58)$$

and

$$C_{12} = -C_{21}$$

$$= \int_{R}^{\infty} dR_{1} A_{12}(R_{1}) - \int_{R}^{\infty} dR_{1} A_{12}(R_{1}) \int_{R_{1}}^{\infty} dR_{2} A_{12}(R_{2}) \int_{R_{2}}^{\infty} dR_{3} A_{12}(R_{3})$$

$$+ \dots$$

$$= \int_{R}^{\infty} dR_{1} A_{12}(R_{1})$$

$$- \frac{1}{3!} \int_{R}^{\infty} dR_{1} A_{12}(R_{1}) \int_{R}^{\infty} dR_{2} A_{12}(R_{2}) \int_{R}^{\infty} dR_{3} A_{12}(R_{3})$$

$$+ \dots$$

$$= \sin \omega(R), \qquad (2.59)$$

where we used [22]

$$\int_{R}^{\infty} dR_{1} A_{12}(R_{1}) \int_{R_{1}}^{\infty} dR_{2} A_{12}(R_{2}) \dots \int_{R_{n-1}}^{\infty} dR_{n} A_{12}(R_{n})$$

$$= \frac{1}{n!} \int_{R}^{\infty} dR_{1} A_{12}(R_{1}) \int_{R}^{\infty} dR_{2} A_{12}(R_{2}) \dots \int_{R}^{\infty} dR_{n} A_{12}(R_{n}) \tag{2.60}$$

and define

$$\omega(R) \equiv \int_{R}^{\infty} dR' A_{12}(R'). \tag{2.61}$$

In matrix form, the transformation matrix C(R) for the two-state case is given by

$$C(R) = \begin{pmatrix} \cos \omega(R) & \sin \omega(R) \\ -\sin \omega(R) & \cos \omega(R) \end{pmatrix}.$$
 (2.62)

Its unitary property can be easily proved and the boundary condition of $R \to \infty$ is satisfied. C(R) here is the rotation matrix. For three- and four-state cases, analytical expressions of the transformation matrix C(R) were given by the work of Heil *et al.* [23].

2.4 Partial wave analysis

The channel functions (nuclear wave functions) of coupled Schrödinger equations can be expanded in terms of total angular momentum wave functions to obtain coupled radial equations. In the scattering systems, we neglect the interaction of the electronic spin and the orbital angular momentum (i.e. spin-orbit coupling) so that the total angular momentum \mathbf{J} is the sum of the nuclear orbital angular momentum \mathbf{N} and the electronic orbital angular momentum \mathbf{L} . Using the expression relating angular momentum in spherical polar coordinates to Cartesian components (see Appendix D), we have the following

$$J_{+} \equiv J_{x} + iJ_{y}$$

$$= \exp(i\Phi) \left(\frac{\partial}{\partial \Theta} + i \cot \Theta \frac{\partial}{\partial \Phi} + \frac{\lambda}{\sin \Theta} \right), \qquad (2.63)$$

$$J_{-} \equiv J_{x} - iJ_{y}$$

$$= \exp\left(-i\Phi\right) \left(-\frac{\partial}{\partial\Theta} + i\cot\Theta\frac{\partial}{\partial\Phi} + \frac{\lambda}{\sin\Theta}\right), \qquad (2.64)$$

and

$$J_z \equiv -i\frac{\partial}{\partial \Phi},\tag{2.65}$$

where we neglect primes on the derivatives, because channel functions are only dependent on \mathbf{R} . Taking advantage of Eqs. (2.63), (2.64), and (2.65), the operator \mathbf{J}_i^2 defined in Eq. (2.27) can be proved to be the square of the total angular momentum \mathbf{J} (see Appendix E). Because \mathbf{J}^2 and J_z commute, we could find simultaneous eigenfunctions $\mathbf{H}_{M,\lambda}^J(\Theta,\Phi)$ so that

$$\mathbf{J}^{2}\mathbf{H}_{M,\lambda}^{J}(\Theta,\Phi) = J(J+1)\mathbf{H}_{M,\lambda}^{J}(\Theta,\Phi), \tag{2.66}$$

and

$$J_z \mathbf{H}_{M,\lambda}^J(\Theta, \Phi) = M \mathbf{H}_{M,\lambda}^J(\Theta, \Phi), \tag{2.67}$$

where M is the projection of the total angular momentum \mathbf{J} onto the z-axis of the space-fixed frame. The Φ -dependence of $\mathbf{H}_{M,\lambda}^{J}(\Theta,\Phi)$ can be obtained directly from Eq. (2.67), while the Θ -dependence is given by [24, 25]

$$d_{M,\lambda}^{J}(\Theta) = N_{M,\lambda}^{J} \sum_{\sigma} {J + \lambda \choose J - M - \sigma} {J - \lambda \choose \sigma} (-1)^{J - M - \sigma} \times \left[\cos\frac{\Theta}{2}\right]^{2\sigma + M + \lambda} \left[\sin\frac{\Theta}{2}\right]^{2J - 2\sigma - M - \lambda}, \tag{2.68}$$

where

$$\binom{n}{m} = \frac{n!}{m!(n-m)!},\tag{2.69}$$

and

$$N_{M,\lambda}^{J} = \sqrt{\frac{(J+M)!(J-M)!}{(J+\lambda)!(J-\lambda)!}}.$$
 (2.70)

 $N_{M,\lambda}^J$ is determined by the normalization property of $\mathbf{H}_{M,\lambda}^J(\Theta,\Phi)$:

$$\int_0^{\pi} \sin\Theta d\Theta \int_0^{2\pi} d\Phi \mathbf{H}_{M,\lambda}^{J^*}(\Theta, \Phi) \mathbf{H}_{M',\lambda}^{J'}(\Theta, \Phi) = \frac{4\pi}{2J+1} \delta_{JJ'} \delta_{MM'}. \tag{2.71}$$

Eq. (2.68) also could be rewritten in terms of the Jacobi polynomial using Rodrigues' formula [24], namely

$$d_{M,\lambda}^{J}(\Theta) = N_{M,\lambda}^{J} \frac{(1-\mu)^{\frac{\lambda-M}{2}}}{(1+\mu)^{\frac{\lambda+M}{2}}} \left[\left(\frac{\partial}{\partial \mu} \right)^{J-M} (1-\mu)^{J-\lambda} (1+\mu)^{J+\lambda} \right], \tag{2.72}$$

where $\mu = \cos \Theta$.

The eigenfunctions $\mathbf{H}_{M,\lambda}^{J}(\Theta,\Phi)$ can be written as

$$\mathbf{H}_{M,\lambda}^{J}(\Theta,\Phi) = (-1)^{\lambda+M} d_{M,\lambda}^{J}(\Theta) \exp(iM\Phi). \tag{2.73}$$

and the expansion of channel function $G_i(\mathbf{R})$ is

$$G_j(\mathbf{R}) = \frac{1}{R} \sum_J g_j^J(R) \mathbf{H}_{M,\lambda_j}^J(\Theta, \Phi). \tag{2.74}$$

In order to obtain coupled radial equations, we substitute Eq. (2.74) for the channel function in Eq. (2.47) and use the orthogonal property of $\mathbf{H}_{M,\lambda_j}^J(\Theta,\Phi)$ to cancel the angular part of the channel function. Because the rotational coupling ${}^dV_{ij}^C(\mathbf{R})$ is the only one which includes derivatives with respect to Θ and Φ , we need to clarify operations of the rotational coupling on $\mathbf{H}_{M,\lambda_j}^J(\Theta,\Phi)$ in advance. Replacing the \bar{L}_x and \bar{L}_y by \bar{L}_+ and \bar{L}_- , the rotational coupling in Eq. (2.47) can be written in the form of

$${}^{d}V_{ij}^{C}(\mathbf{R}) = \frac{-1}{R^{2}} \left\{ \langle i^{d} | \bar{L}_{+} | j^{d} \rangle \left[-\frac{\partial}{\partial \Theta} + \frac{i}{\sin \Theta} \frac{\partial}{\partial \Phi} + \lambda_{j} \cot \Theta \right] + \langle i^{d} | \bar{L}_{-} | j^{d} \rangle \left[\frac{\partial}{\partial \Theta} + \frac{i}{\sin \Theta} \frac{\partial}{\partial \Phi} + \lambda_{j} \cot \Theta \right] \right\}.$$
(2.75)

Due to the commutation relations,

$$[J_z, J_{\pm}] = \pm J_{\pm},$$
 (2.76)

and the help of

$$J_{-}J_{+} = \mathbf{J}^{2} - J_{z}^{2} - J_{z} \tag{2.77}$$

and

$$J_{+}J_{-} = \mathbf{J}^{2} - J_{z}^{2} + J_{z}, \tag{2.78}$$

the result of operators J_+ and J_- acting on $\mathbf{H}^J_{M,\lambda_j}(\Theta,\Phi)$ are given by

$$J_{\pm}\mathbf{H}_{M,\lambda_{i}}^{J}(\Theta,\Phi) = \sqrt{(J \pm M + 1)(J \mp M)}\mathbf{H}_{M\pm1,\lambda_{i}}^{J}(\Theta,\Phi). \tag{2.79}$$

Using Eq. (2.79) and the fact of

$$d_{M,\lambda_j}^J(-\Theta) = d_{\lambda_j,M}^J(\Theta), \tag{2.80}$$

which is easily proved by Eq. (2.68), we can obtain useful relations as follows (see Appendix F),

$$\left[\mp \frac{\partial}{\partial \Theta} + \frac{i}{\sin \Theta} \frac{\partial}{\partial \Phi} + \lambda_j \cot \Theta\right] \mathbf{H}_{M,\lambda_j}^J(\Theta, \Phi)$$

$$= \sqrt{(J \pm \lambda_j + 1)(J \mp \lambda_j)} \mathbf{H}_{M,\lambda_j \pm 1}^J(\Theta, \Phi). \tag{2.81}$$

According to Eqs. (2.75) and (2.81) followed by normalization integrals, it leads to

$$^{d}\bar{V}_{ij}^{C}(R) \equiv \frac{2J+1}{4\pi} \int_{0}^{\pi} \sin\Theta d\Theta \int_{0}^{2\pi} d\Phi \mathbf{H}_{M,\lambda_{i}}^{J^{*}}(\Theta,\Phi)^{d} V_{ij}^{C}(\mathbf{R}) \mathbf{H}_{M',\lambda_{j}}^{J'}(\Theta,\Phi)$$

$$= -\delta_{\lambda_{i},\lambda_{j}+1} \left[(J-\lambda_{j})(J+\lambda_{j}+1) \right]^{1/2} \frac{\langle i^{d}|\bar{L}_{+}|j^{d}\rangle}{R^{2}}$$

$$-\delta_{\lambda_{i},\lambda_{j}-1} \left[(J+\lambda_{j})(J-\lambda_{j}+1) \right]^{1/2} \frac{\langle i^{d}|\bar{L}_{-}|j^{d}\rangle}{R^{2}}. \tag{2.82}$$

Due to the properties of \bar{L}_+ and \bar{L}_- ,

$$\delta_{\lambda_i,\lambda_j-1}\langle i^d|\bar{L}_+|j^d\rangle = 0 \tag{2.83}$$

and

$$\delta_{\lambda_i,\lambda_j+1}\langle i^d|\bar{L}_-|j^d\rangle = 0. \tag{2.84}$$

We can rewrite ${}^d\bar{V}^C_{ij}(R)$ as

$${}^{d}\bar{V}_{ij}^{C}(R) = -2\delta_{\lambda_{i},\lambda_{j}+1} \left[(J-\lambda_{j})(J+\lambda_{j}+1) \right]^{1/2} \frac{\langle i^{d}|i\bar{L}_{y}|j^{d}\rangle}{R^{2}}$$

$$+2\delta_{\lambda_{i},\lambda_{j}-1} \left[(J+\lambda_{j})(J-\lambda_{j}+1) \right]^{1/2} \frac{\langle i^{d}|i\bar{L}_{y}|j^{d}\rangle}{R^{2}}.$$

$$(2.85)$$

Finally, the coupled radial equations extracted from Eq. (2.47) are given as

$$\sum_{j=1}^{N} \left\{ \left[\frac{\partial^{2}}{\partial R^{2}} + \frac{\lambda_{i}^{2} - J(J+1)}{R^{2}} \right] \delta_{ij} - 2\mu U_{ij} + 2\mu E \delta_{ij} \right\} g_{j}^{J}(R)$$

$$= \sum_{j=1}^{N} \left[{}^{d}V_{ij}^{R}(R) + {}^{d}\bar{V}_{ij}^{C}(R) \right] g_{j}^{J}(R), \qquad (2.86)$$

where $g_j^J(R)$ is defined in Eq. (2.74).

2.5 The scattering S-matrix

The coupled radial Schrödinger equations can be expressed in matrix form as

$$\left[\frac{d^2}{dR^2}I + \mathcal{V}(R)\right]\mathcal{G}^J(R) = \underline{0},\tag{2.87}$$

where I is the identity matrx, $\underline{0}$ the null matrix and \mathcal{V} the symmetric potential matrix with elements

$$\mathcal{V}_{ij}(R) = \frac{\lambda_i^2 - J(J+1)}{R^2} \delta_{ij} + \sum_n C_{in}^{\dagger}(R) k_n^2 C_{nj}(R) - {}^{d}V_{ij}^{R}(R) - {}^{d}V_{ij}^{C}(R). \tag{2.88}$$

Each column of the square matrix $\mathcal{G}^{J}(R)$ is a linear independent solution including each radial channel function as an element for the coupled equations. In other words, $\mathcal{G}_{ij}^{J}(R)$ is the *i*th channel component of the *j*th independent solution. A general solution is a linear combination of channel functions.

According to Eqs. (2.52), (2.53), and (2.85), we have the asymptotic limit

$$R^{2}\mathcal{V}_{ij}(R) \xrightarrow{R \to \infty} \left[\lambda_{i}^{2} - J(J+1) + (k_{i}R)^{2}\right] \delta_{ij}$$

$$-\langle i^{d}|\overline{L}_{x}^{2} + \overline{L}_{y}^{2}|j^{d}\rangle$$

$$-2\delta_{\lambda_{i},\lambda_{j}+1} \left[(J-\lambda_{i})(J+\lambda_{j}+1)\right]^{1/2} \langle i^{d}|i\overline{L}_{y}|j^{d}\rangle$$

$$+2\delta_{\lambda_{i},\lambda_{j}-1} \left[(J+\lambda_{i})(J-\lambda_{j}+1)\right]^{1/2} \langle i^{d}|i\overline{L}_{y}|j^{d}\rangle. \tag{2.89}$$

If λ_i , $\langle i^d | \overline{L}_x^2 + \overline{L}_y^2 | j^d \rangle$, and $\langle i^d | i \overline{L}_y | j^d \rangle$ compared with J(J+1) can be neglected as $R \to \infty$, the off-diagonal terms of Eq. (2.87) will vanish and only diagonal terms remain. Namely,

$$\[\frac{d^2}{dR^2} + k_i^2 - \frac{J(J+1)}{R^2} \] \mathcal{G}_{ii}^J(R) = 0, \tag{2.90}$$

which is the Riccati-Bessel equation. Two linear independent solutions of Eq. (2.90) are the Riccati-Bessel functions, $\hat{j}_J(k_iR)$ and $\hat{n}_J(k_iR)$, which can be expressed as

$$\begin{cases}
\hat{j}_J(k_i R) = k_i R j_J(k_i R) & \xrightarrow{R \to \infty} \sin(k_i R - \frac{1}{2} J \pi) \\
\hat{n}_J(k_i R) = k_i R n_J(k_i R) & \xrightarrow{R \to \infty} \cos(k_i R - \frac{1}{2} J \pi),
\end{cases} (2.91)$$

where $j_J(k_iR)$ and $n_J(k_iR)$ are spherical Bessel functions of the first and second kind, respectively. Therefore, the general solution of Eq. (2.87) in the asymptotic region can be expressed as a linear combination of Riccati-Bessel functions or spherical Bessel functions. The method we adopt for solving this multichannel scattering problem is the multichannel log-derivative method of Johnson [26]. In this approach, the log-derivative matrix is defined to be

$$y(R) = \left[\mathcal{G}^J(R)\right]' \left[\mathcal{G}^J(R)\right]^{-1}, \qquad (2.92)$$

where the prime means differentiation with respect to R, while the boundary conditions are chosen to be

$$\mathcal{G}^J(0) = 0 \tag{2.93}$$

and

$$\left[\mathcal{G}^{J}(0)\right]' = I. \tag{2.94}$$

Using Eq. (2.92) to eliminate the second derivative term of $\mathcal{G}^{J}(R)$ in Eq. (2.87), we obtain

$$y'(R) + \mathcal{V}(R) + y^2(R) = 0 \tag{2.95}$$

with y'(0) which is a diagonal matrix with infinite elements. The numerical techniques for solving the differential equation (2.95) are given in Ref. [26]. The numerical solutions of Eq. (2.95) are required to match the asymptotic form of the wave function, namely for some R_N which is numerically large enough to be regarded as infinity,

$$\mathcal{G}^{J}(R) = \mathcal{J}(R) + \mathcal{N}(R)\mathcal{K}^{J}, \quad R \ge R_{N}$$
(2.96)

where K is the reaction matrix. The diagonal matrices $\mathcal{J}(R)$ and $\mathcal{N}(R)$ for the open channels are defined as

$$\begin{cases}
\mathcal{J}_{ij}(R) = \delta_{ij}k_j^{-1/2}\hat{j}_J(k_jR) \\
\mathcal{N}_{ij}(R) = \delta_{ij}k_j^{-1/2}\hat{n}_J(k_jR).
\end{cases} (2.97)$$

Taking advantage of the multichannel log-derivative method, $y(R_N)$ can be obtained and the K-matrix may be extracted from Eqs. (2.92) and (2.96). On the other hand, because the spherical Bessel functions, j_J and n_J , can be expressed in terms of spherical Hankel functions, $h_J^{(1)}$ (outgoing waves) and $h_J^{(2)}$ (incoming waves), we also could describe the asymptotic boundary condition, instead of using Eq. (2.96), by the following:

$$\mathcal{G}^{J}(R) = \mathcal{H}^{(2)}(R) + \mathcal{H}^{(1)}(R)\mathcal{S}^{J}, \quad R \to \infty$$
(2.98)

where $\mathcal{H}^{(1)}$ and $\mathcal{H}^{(2)}$ are diagonal matrices with elements defined as

$$\begin{cases}
\mathcal{H}_{ij}^{(1)}(R) = \delta_{ij}k_j^{-1/2}\exp\left[i(k_jR - \frac{1}{2}J\pi)\right] \\
\mathcal{H}_{ij}^{(2)}(R) = \delta_{ij}k_j^{-1/2}\exp\left[-i(k_jR - \frac{1}{2}J\pi)\right].
\end{cases} (2.99)$$

Comparing Eqs. (2.96) and (2.98), we can obtain a relation between the S-matrix and the K-matrix as

$$S^{J} = \left[\mathbf{I} + i \mathcal{K}^{J} \right] \left[\mathbf{I} - i \mathcal{K}^{J} \right]^{-1}. \tag{2.100}$$

Solving the coupled radial Schrödinger equations, the solution of the *i*th linear independent radial wave function, $g_{ith}^{J}(R)$, can be written as

$$g_{i\text{th}}^{J}(R) = \sum_{j} C_{j}^{(i)} g_{j}^{J}(R) = \sum_{j} C_{j}^{(i)} \mathcal{G}_{ji}^{J}(R).$$
 (2.101)

According to Eq. (2.74), the *i*th general solution of the nuclear wave function, $G_{i\text{th}}(\mathbf{R})$, can be expressed as

$$G_{i\text{th}}(\mathbf{R}) = \sum_{j} C_j^{(i)} G_j(\mathbf{R}) = \sum_{J} \sum_{j} C_j^{(i)} \frac{\mathcal{G}_{ji}^J}{R} \mathbf{H}_{M,\lambda_j}^J(\Theta, \Phi), \qquad (2.102)$$

and asymptotically as

$$G_{i\text{th}}(\mathbf{R}) = \sum_{J} \sum_{j} C_{j}^{(i)} \frac{1}{R} \left\{ \delta_{ji} k_{i}^{-1/2} \exp\left[-i(k_{i}R - \frac{1}{2}J\pi)\right] - \mathcal{S}_{ji}^{J} k_{j}^{-1/2} \exp\left[i(k_{j}R - \frac{1}{2}J\pi)\right] \right\} \mathbf{H}_{M,\lambda_{j}}^{J}(\Theta, \Phi).$$

$$(2.103)$$

Alternatively, the scattering amplitude $f_{ji}(\Theta, \Phi)$ is defined by the asymptotic form of the nuclear wave function:

$$G_{i\text{th}}(\mathbf{R}) = A \sum_{i} \left[\delta_{ji} \exp\left(i\mathbf{k}_{i} \cdot \mathbf{R}\right) + f_{ji}(\Theta, \Phi) \frac{\exp\left(ik_{j}R\right)}{R} \right], \tag{2.104}$$

where \mathbf{k}_i is in a direction parallel to the direction of incidence, which we take to be the z-axis. Because the expansion of incident plane waves in terms of spherical Bessel functions $j_J(k_iR)$ is

$$\exp(ik_i z) = \sum_{J} [(4\pi)(2J+1)]^{1/2} i^J j_J(k_i R) \mathbf{H}_{0,\lambda_i}^J, \qquad (2.105)$$

 $G_{i\text{th}}(\mathbf{R})$ can be rewritten as a linear combination of incoming spherical waves, $\exp(-ik_iR)/R$, and outgoing spherical waves, $\exp(ik_jR)/R$. The coefficients for incoming waves are

$$\frac{A\delta_{ji}}{2k_i} \sum_{J} \left[(4\pi)(2J+1) \right]^{1/2} i^{2J+1} \mathbf{H}_{0,\lambda_j}^{J}, \tag{2.106}$$

and for outgoing waves are

$$\frac{iA\delta_{ji}}{2\sqrt{k_i k_j}} \sum_{J} \left[\left[(4\pi)(2J+1) \right]^{1/2} \mathbf{H}_{0,\lambda_j}^{J} \right] + Af_{ji}, \tag{2.107}$$

where we use the fact of $\delta_{ji} \frac{1}{k_i} = \delta_{ji} \frac{1}{\sqrt{k_i k_j}}$. Comparing the coefficients of incoming and outgoing spherical wave in Eqs. (2.103), (2.106), and (2.107), we find that the scattering amplitude is independent of Φ and given by

$$f_{ji}(\Theta) = \sum_{J} \frac{i}{2\sqrt{k_i k_j}} \left[(4\pi)(2J+1) \right]^{1/2} \mathbf{H}_{0,\lambda_j}^{J}(\Theta, \Phi) \left[\delta_{ji} - \mathcal{S}_{ji} \right].$$
 (2.108)

Given the scattering amplitude, the corresponding differential cross section is given by (see Appendix G)

$$\frac{d\sigma_{ji}}{d\Omega} = \frac{k_j}{k_i} |f_{ji}(\Theta)|^2, \tag{2.109}$$

and the integral cross section in term of the S-matrix is

$$\sigma_{ji} = \frac{\pi}{k_i^2} \sum_{J} (2J+1) |\delta_{ji} - \mathcal{S}_{ji}^J|^2.$$
 (2.110)

2.6 Infinite order sudden approximation

From the point of view of coupled equations, the study of collisions of neutral and ionic atoms with molecules faces the problem of increased complexity. Compared to ion-atom collisions, the degrees of freedom for a system of ion-molecule collisions increases due to the addition of vibrational and rotational motion of the molecule. The rapid increase of the number of channels of vibronic or ro-vibronic states leads to the treatment of coupled scattering equations becoming a formidable task. Over the past four decades, progress has been made in the development of approximate methods, which can be traced with the review article of Tully [27], the book of Bernstein [15], the work of Kleyn et. al. [28] and Baer [29].

In order to reduce the complexity arising from the rotational and vibrational degrees of freedom, the so-called infinite order sudden approximation (IOSA) provides a practical approach to deal with coupled-channel calculations for vibronic transition processes. One of the first quantal coupled-channel calculations using IOSA was reported by McGuire and Bellum [30]. The IOSA approach is based on the energy sudden (ES) and centrifugal sudden (CS) approximations. For the ES approximation, the spacings between the rotational levels of the target molecule are neglected. This is equivalent to treating all of rotational levels as degenerate. In other words, one replaces the various wave numbers with respect to the various rotational levels by an effective wave number. Qualitatively, the criteria for the validity of this approximation requires that the rotational periods of the target molecule are much larger than a characteristic collision time of the projectile relative to the target center of mass. In general, atom- or ion-molecule collisions with collision energies larger than 0.1 eV/u fulfill the condition.

In the CS approximation, the relative radial velocity of the projectile needs to be much faster than the velocity of its rotational motion around the molecule center of mass. Based on this assumption, the CS approximation apparently would fail in the vicinity of a classical turning point due to the lack of radial velocity at these points by definition. On the other

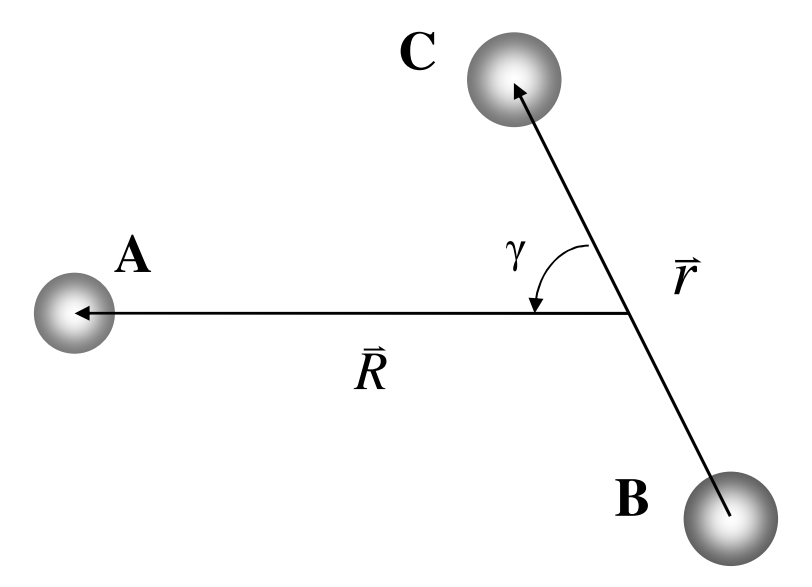


Figure 2.2: Jacobi coordinates for a A-BC system.

hand, the approximation is more applicable for collisions with small projectile orbital angular momentum of the projectile because of the small centrifugal barrier.

Within the framework of the MOCC method, the treatment of ion-molecule collisions is carried out under the IOSA approach. It is appropriate to describe these collision systems in Jacobi coordinates as follows: \mathbf{R} is the vector pointing from the target molecule center of mass to the projectile, \mathbf{r} the vector representing the internal geometry of the target molecule, and γ the angle between \mathbf{R} and \mathbf{r} (see Fig. 2.2). After removal of the center of mass motion, the Hamiltonian for collisions of atom A with diatomic molecule BC is written as

$$H = -\frac{1}{2\mu_R} \nabla_{\mathbf{R}}^2 - \frac{1}{2\mu_r} \nabla_{\mathbf{r}}^2 - \frac{1}{2} \nabla_{\mathbf{s}}^2 + V(\mathbf{R}, \mathbf{r}, \mathbf{s}), \qquad (2.111)$$

where $\mu_R = M_A(M_B + M_C)/(M_A + M_B + M_C)$ and $\mu_r = M_B M_C/(M_B + M_C)$. $V(\mathbf{R}, \mathbf{r}, \mathbf{s})$ represents nucleus-nucleus, nucleus-electron, and electron-electron Coulomb interactions. The origin of electronic position vectors \mathbf{s} is chosen to be the nuclear center of mass of the ABC system. The mass polarization terms are neglected. It is worth mentioning that there will be a summation over electronic kinetic energy operators if the system involves more than one

electron. The total wave function Ψ in terms of diabatic molecular orbitals $\bar{\psi}_k^d(\mathbf{s}', R, r, \gamma)$, where \mathbf{s}' represents the electronic position vector in the body-fixed frame, can be expanded as

$$\Psi = \sum_{k,\nu} \bar{\psi}_k^d(\mathbf{s}', R, r, \gamma) N_k(\mathbf{R}, \mathbf{r}), \qquad (2.112)$$

where the nuclear wave function $N_k(\mathbf{R}, \mathbf{r})$ is given by the expansion of a complete basis set $\xi_{k\nu}(\mathbf{r})$ of the diatom:

$$N_k(\mathbf{R}, \mathbf{r}) = \sum_{\nu} G_{k\nu}(\mathbf{R}) \xi_{k\nu}(\mathbf{r}). \tag{2.113}$$

The $\xi_{k\nu}(\mathbf{r})$ are eigenfunctions of the equation

$$\left[-\frac{1}{2\mu_r} \nabla_{\mathbf{r}}^2 + U_{kk}(R \to \infty, r; \gamma) \right] \xi_{k\nu}(\mathbf{r}) = E_{k\nu} \xi_{k\nu}(\mathbf{r}), \tag{2.114}$$

where γ is taken as a parameter, $E_{k\nu}$ is an eigenvalue and U_{kk} , a diagonal element of the diabatic potential matrix which becomes the potential curve of the diatom BC as R approaches the asymptotic limit. U_{kk} is, therefore, independent of γ as $R \to \infty$. The orthonormal property of $\xi_{k\nu}(\mathbf{r})$ is given by

$$\langle \xi_{k\nu} | \xi_{k'\nu'} \rangle = (1 - \delta_{kk'}) \int d\mathbf{r} \xi_{k\nu}(\mathbf{r}) \xi_{k'\nu'}(\mathbf{r}) + \delta_{kk'} \delta_{\nu\nu'}. \tag{2.115}$$

Under the assumption of the ES approximation, the $\xi_{k\nu}(\mathbf{r})$ can be expressed as

$$\xi_{k\nu}(\mathbf{r}) = \frac{\chi_{k\nu}(r)}{r} |j_k, m_{j_k}\rangle, \qquad (2.116)$$

where $|j_k, m_{j_k}\rangle$ represents a rotational wave function, with $j_k = 0$ in practice, and $\chi_{k\nu}(r)$, the vibrational wave function of the diatom, satisfies the equation

$$\left[-\frac{1}{2\mu_r} \frac{d^2}{dr^2} + U_{kk}(R \to \infty, r) \right] \chi_{k\nu}(r) = E_{k\nu} \chi_{k\nu}(r). \tag{2.117}$$

Expanding U_{kk} by r with respect to it's equilibrium position r_e , the eigenvalue $E_{k\nu}$ has the following relation with the vibrational excitation energy $\varepsilon_{k\nu}$:

$$E_{k\nu} = U_{kk}(R \to \infty, r = r_e) + \varepsilon_{k\nu}. \tag{2.118}$$

Inserting the total wave function Ψ into the Schrödinger equation followed by projections on $\bar{\psi}_k^d(\mathbf{s}', R, r, \gamma)$ and $\xi_{k\nu}(\mathbf{r})$, we can obtain a set of coupled Schrödinger equations:

$$\left(\nabla_{\mathbf{R}}^{2} + k_{i\nu}^{2}\right) G_{i\nu}(\mathbf{R}) = 2\mu_{R} \sum_{j \neq i} \sum_{\nu'} \langle \chi_{i\nu}(r) | U_{ij}(R, r, \gamma) | \chi_{j\nu'}(r) \rangle G_{j\nu'}(\mathbf{R})$$

$$+ \sum_{j} \sum_{\nu'} \langle \chi_{i\nu}(r) | M_{ij} + \mathbf{P}_{ij} \cdot \nabla_{\mathbf{R}} | \chi_{j\nu'}(r) \rangle G_{j\nu'}(\mathbf{R}), \qquad (2.119)$$

where $k_{i\nu}^2$ is defined as

$$k_{i\nu}^2 = 2\mu_R \left[E - \langle \chi_{i\nu} | U_{ii}(R, r, \gamma) | \chi_{i\nu} \rangle \right],$$
 (2.120)

while M_{ij} and \mathbf{P}_{ij} are given as Eqs. (2.8) and (2.9) except replacing the adiabatic electronic wave function by a diababtic one. The term

$$\langle \chi_{i\nu}(r)|U_{ii}(R,r,\gamma)|\chi_{i\nu}(r)\rangle,$$
 (2.121)

which is a integral of diabatic electronic potential energies U_{ii} over vibrational wave functions, is the so-called diabatic vibronic energy and E is the total energy of the system. We make the approximation that the diabatic vibronic energies can be obtained by

$$\langle \chi_{i\nu}(r)|U_{ii}(R,r,\gamma)|\chi_{i\nu}(r)\rangle = U_{ii}(R,r=r_e,\gamma) + \varepsilon_{i\nu}. \tag{2.122}$$

The vibrationally-resolved couplings (vibronic couplings) appearing in the right hand side of Eq. (2.119) come mainly from two parts. One is the integral of the off-diagonal term U_{ij} over vibrational wave functions, where U_{ij} is the diabatic electronic coupling resulting from the interaction between molecular states of the same symmetry ($\lambda = \lambda'$). The other one is the integral related to M_{ij} and \mathbf{P}_{ij} over vibrational wave functions, while in the diabatic representation only the electronic couplings connecting molecular states with different symmetry ($\lambda = \lambda' \pm 1$) in the M_{ij} and \mathbf{P}_{ij} remain.

Since within the framework of IOSA, the coupled equations are solved for each orientation angle γ , the S-matrix, using the same approach described in Sec. 2.4, is extracted from the asymptotic boundary condition and is parametrically dependent on γ . Therefore, the major physical quantities, cross sections, for transitions driven by vibronic couplings are

 γ -dependent. This leads to vibrationally-resolved state-to-state cross section $\sigma_{k\nu',i\nu}(E,\gamma)$ for transitions from the ν th vibrational state of the *i*th electronic state to the ν' th vibrational state of the *k*th electronic state expressed in terms of *S*-matrix elements as

$$\sigma_{k\nu',i\nu}(E,\gamma) = \frac{\pi g_{i\nu}}{k_{i\nu}^2} \sum_{J} (2J+1) |S_{k\nu',i\nu}^J(\gamma)|^2, \qquad (2.123)$$

where $k_{i\nu}$ denotes the wave number for the A-BC center-of-mass motion of the initial incoming channel and $g_{i\nu}$ is the initial approach probability factor for the electronic state. Given the state-to-state cross sections, we can sum over all final vibronic states to obtain the vibrationally-resolved initial state-selective cross section

$$\sigma_{i\nu}(E,\gamma) = \sum_{k\nu'} \sigma_{k\nu',i\nu}(E,\gamma), \qquad (2.124)$$

or all initial vibronic states to give the vibrationally-resolved final state-selective cross section

$$\sigma_{k\nu'}(E,\gamma) = \sum_{i\nu} \sigma_{k\nu',i\nu}(E,\gamma). \tag{2.125}$$

In LTE, the distribution of initial states for molecular targets depends on the molecular gas temperature T. In order to take this effect into account, the population of initial vibrational states for molecular targets is determined with a Boltzmann distribution. The total cross section for a given temperature T and orientation angle γ is given by

$$\sigma(E, T, \gamma) = \frac{\sum_{i\nu} \exp(-\varepsilon_{i\nu}/k_b T) \sigma_{i\nu}(E, \gamma)}{\sum_{i\nu} \exp(-\varepsilon_{i\nu}/k_b T)},$$
(2.126)

where $\varepsilon_{i\nu}$ are the excitation energies of the diatom and k_b the Boltzmann constant.

The physical quantities independent of orientation angle are obtained following an integral over the orientation angle γ , which gives angle-averaged cross sections as [17]

$$\sigma(E,T) = \frac{1}{2} \int_0^{\pi} \sigma(E,T,\gamma) \sin \gamma d\gamma. \tag{2.127}$$

It is easy to see from Eqs. (2.126) and (2.127) that angle-averaged total cross sections for a given temperature T are independent of the order of taking a Boltzmann distribution and integration over the orientation angle.

Chapter 3

Electron capture in collisions of N^+ with H and H^+ with N

As an application of ion-atom collisions, the quantal MOCC approach is applied to charge transfer processes due to collisions of N⁺ with atomic hydrogen and H⁺ with atomic nitrogen. The MOCC calculations utilize *ab initio* adiabatic potentials and nonadiabatic radial and rotational couplings obtained with the multireference single- and double-excitation configuration interaction (MRD-CI) approach. Total and state-selective cross sections for the energy range 0.1 meV/u - 1 keV/u are presented and compared with existing experimental and theoretical data. A large number of low-energy resonances are obtained for exoergic channels and near the threshold of endoergic channels. Rate coefficients are also obtained and comparison to previous calculations suggests nonadiabatic effects dominate for temperatures greater than 20,000 K, but that the spin-orbit interaction plays a major role for lower temperatures [31].

3.1 Introduction

In the electron capture process, electrons are transferred from one atomic system to another during a collision. The importance of electron capture is not only in understanding of dynamical mechanisms for atomic and molecular collisions, but also in practical applications. In many environments of current research, such as planetary atmospheres and astrophysical and laboratory plasmas, charge transfer can have a crucial influence. Because of the abundance of ions in astronomical environments, charge transfer may be the dominant process in establishing the ionization balance and may also influence spectral line emission. In addition,

a deeper understanding of the electron capture process will also help in modeling the edge region of tokamak fusion plasmas [32].

In this work we investigate the reactions

$$N^{+}(2p^{2} {}^{3}P) + H \leftrightarrow N(2p^{3} {}^{2}D^{o}) + H^{+} - 1.4372 \text{ eV},$$
 (3.1)

and

$$N^{+}(2p^{2} {}^{3}P) + H \leftrightarrow N(2p^{3} {}^{4}S^{o}) + H^{+} + 0.9467 \text{ eV},$$
 (3.2)

using the MOCC method. The theoretical method for the scattering calculations has been described in Chapter 2 and has also been given in the literature [33, 34]. A brief description of the electronic structure calculations is presented in Section 3.2. In Section 3.3 the adiabatic potentials and nonadiabatic couplings of NH⁺ are discussed. The resulting cross sections and rate coefficients including total and state-selective are given in Section 3.4 and compared with the existing experimental data and previous calculations. Astrophysical implications are given in Section 3.5. Section 3.6 gives a summary of this chapter. Atomic units are used unless otherwise noted.

3.2 Electronic Structure Calculations

The *ab initio* adiabatic potentials and nonadiabatic couplings in the present work are obtained from the MRD-CI method which has been detailed earlier in Buenker and coworker's publications [35, 36, 37]. Here only information relevant to the present calculation is specified. The atomic orbital basis sets for molecular calculations consist of contracted Gaussian functions. The (8s2p) basis for the hydrogen atom is contracted in [5s2p] and augmented by one s-, one p-, and one d-type diffuse function with exponents which are 0.0195, 0.042, and 1.1 respectively. For the nitrogen atom, the (15s10p2d) basis is contracted in [9s6p2d]. Eight molecular states including five doublets and three quartets are considered for collisions of the NH⁺ system. The finite difference technique [38, 39] has been applied to obtain radial

couplings (matrix elements of $\partial/\partial R$), while rotational couplings have been calculated by employing appropriate pairs of CI eigenfunctions.

3.3 POTENTIALS AND COUPLINGS

For the present calculations, adiabatic potentials for NH⁺ include eight molecular states which are 1 $^4\Sigma^-$, 2 $^4\Sigma^-$, 1 $^4\Pi$, 1 $^2\Sigma^-$, 2 $^2\Sigma^-$, 1 $^2\Pi$, 2 $^2\Pi$, and 1 $^2\Delta$. Fig. 3.1 shows the adiabatic potentials as a function of internuclear distance R for R=1 to 10 (a.u.). As internuclear distance approaches infinity, these eight molecular states will degenerate into three separated-atom states which are N(2 p^3 $^4S^o$) + H⁺, N⁺(2 p^2 3P) + H, and N(2 p^3 $^2D^o$) + H⁺. The corresponding relations are displayed in Table 3.1.

The interactions between different molecular states result from nonadiabatic radial and rotational couplings. Radial coupling results from the interaction between molecular states of the same symmetry ($\Lambda=\Lambda'$) while rotational coupling is due to interaction between molecular states of different symmetry ($\Lambda=\Lambda'\pm 1$), where Λ is the projection quantum number of the electronic orbital angular momentum onto the internuclear axis. Nonadiabatic couplings as a function of R are plotted in Fig. 3.2. The radial couplings include interactions of two quartet Σ^- states, two doublet Σ^- states, and two doublet Π states, while the rotational couplings comprise interactions of the quartet Π state with quartet Σ^- states, and doublet Π states with doublet Σ^- and Δ states.

Given adiabatic potentials and couplings, we transform them to a diabatic representation by a unitary transformation [23] as described in Section 2.3. In Fig. 3.3, several diagonal diabatic potentials are plotted and compared with the adiabatic potential energies. It is clear that the adiabatic potential curves of the same symmetry don't cross, but crossings may occur in the diabatic representation. However, adiabatic and diabatic potential curves will merge into identical asymptotical atomic energies at large R. In order to get reliable cross sections near the threshold, we make an asymptotic fit to join the *ab initio* data smoothly

Table 3.1: Comparison of asymptotic separated-atom energies between the MRD-CI calculations and experiments for the eight molecular states of NH⁺. These states are of symmetries $^{2,4}\Sigma^{-}$, $^{2,4}\Pi$, and $^{2}\Delta$.

Asymptotic atomic state	Mol. state	This work	Expt.
		(eV)	(eV)
$N(2p^3 {}^4S^o) + H^+$	$1 \ ^4\Sigma^-$	0.0000	0.0000
$N^{+}(2p^{2} {}^{3}P) + H$	$2~^4\Sigma^-$	0.7143	0.9467
	$1~^2\Pi$	0.7180	
	$1~^4\Pi$	0.7241	_
	$1~^2\Sigma^-$	0.7258	_
$N(2p^3 {}^2D^o) + H^+$	$2~^2\Pi$	2.6407	2.3840
, <u> </u>	$1~^2\Delta$	2.6411	_
	$2~^2\Sigma^-$	2.6435	_

to the long range form $-\frac{\alpha}{2R^4}$, where α is the dipole polarizability. We adopted $\alpha=4.50$ for H and $\alpha=7.42$ and 11.17 for N(2 p^3 $^4S^o$) and N(2 p^3 $^2D^o$), respectively.

Several major off-diagonal diabatic couplings are illustrated in Fig. 3.4. The couplings in Fig. 3.4(a) show the important interactions between the asymptotic atomic states of $N(2p^3 \ ^4S^o) + H^+$ and $N^+(2p^2 \ ^3P) + H$ for the charge transfer process in the NH⁺ system, while the couplings in Fig. 3.4(b) give us the important interactions between $N^+(2p^2 \ ^3P) + H$ and $N(2p^3 \ ^2D^o) + H^+$. The related adiabatic labelings corresponding to a specific diabatic coupling are indicated above the symbol in the figures.

3.4 RESULTS AND DISCUSSION

3.4.1 Cross Sections

The state-selective cross sections for the electron capture process are evaluated by using the molecular electronic structure and coupling data in Section 3.3, but with the potentials

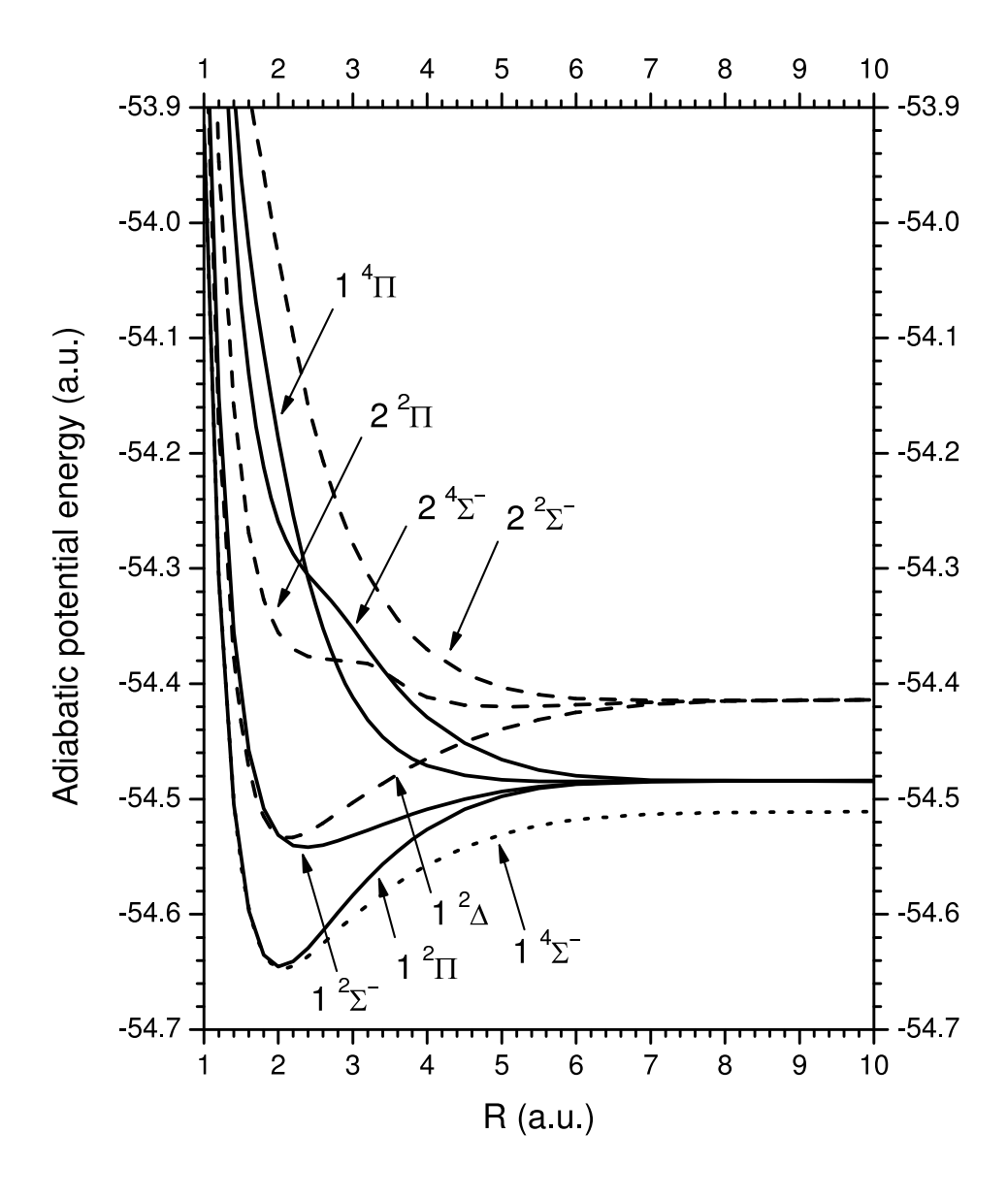


Figure 3.1: Adiabatic potentials for NH⁺ as a function of internuclear distance R. The dotted curve corresponds to the asymptotic atomic state of N($2p^3$ $^4S^o$) + H⁺, solid curves to N⁺($2p^2$ 3P) + H, and dashed curves to N($2p^3$ $^2D^o$) + H⁺.

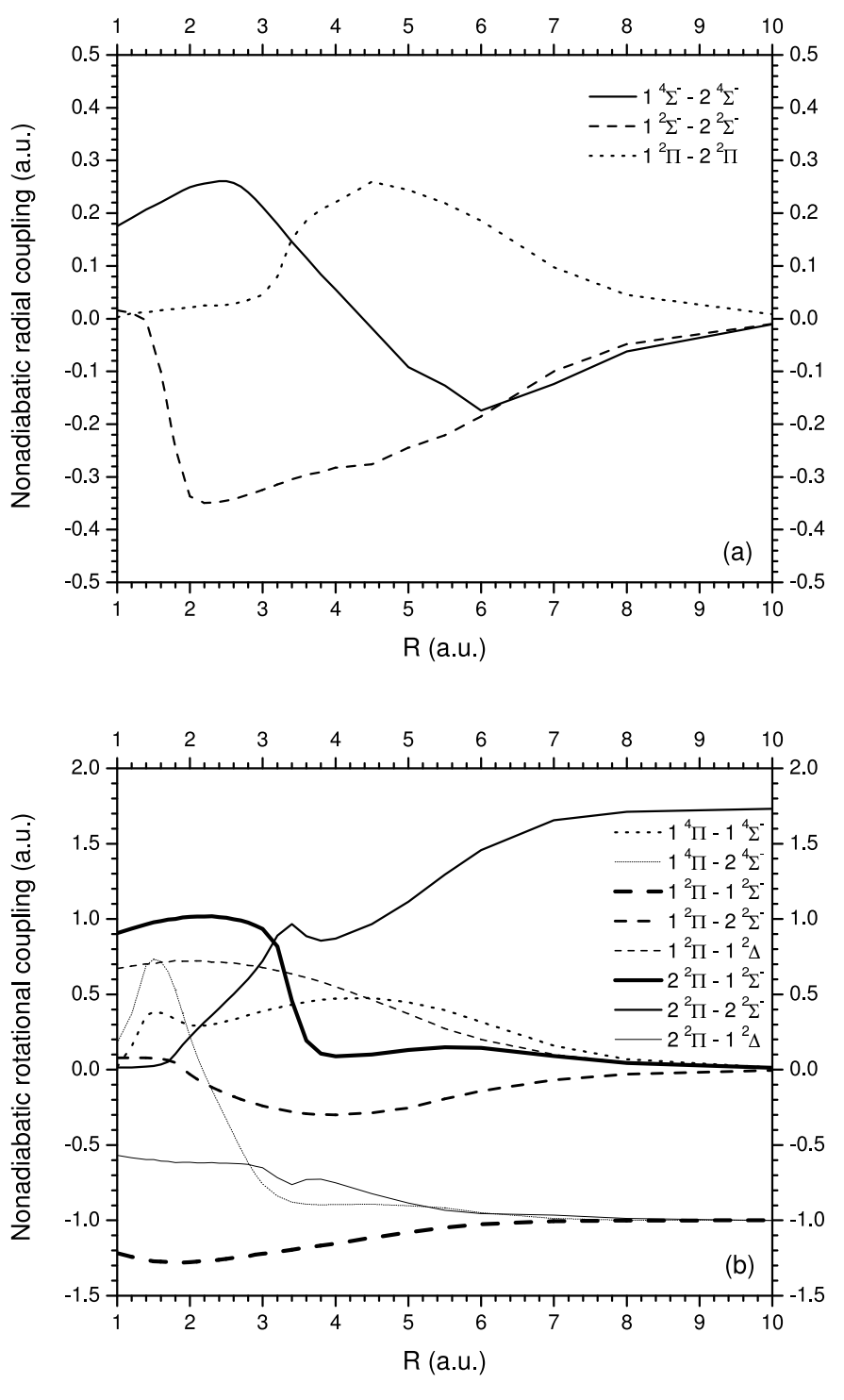


Figure 3.2: Nonadiabatic (a) radial and (b) rotational couplings for the $\mathrm{NH^+}$ system as functions of internuclear distance R.

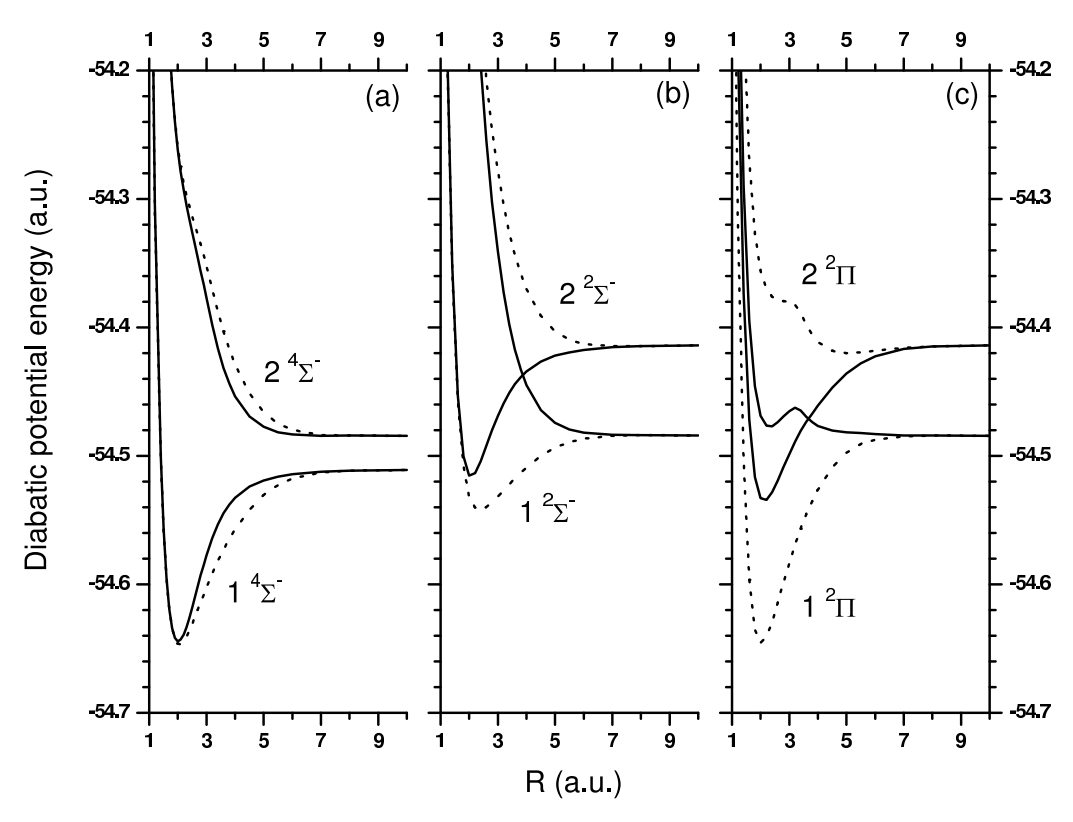


Figure 3.3: Diagonal diabatic potential curves (solid lines) compared to the adiabatic potential energies (dotted lines), (a) the quartet Σ^- states, (b) the doublet Σ^- states, and (c) the doublet Π states.

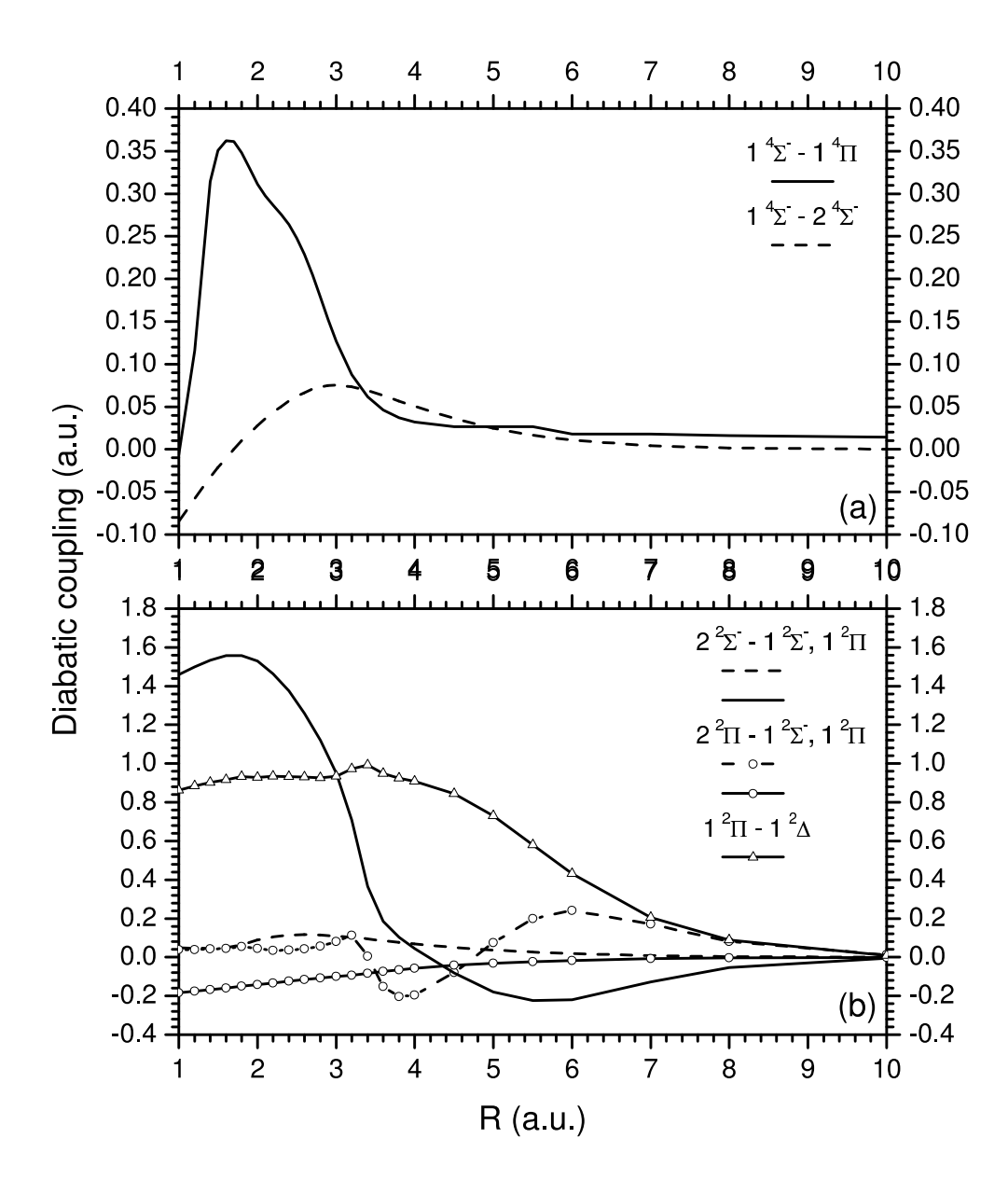


Figure 3.4: Off-diagonal diabatic potentials for the (a) quartet, and (b) doublet states of the NH⁺ system as a function of internuclear distance R.

shifted to match the experimental asymptotic energies as listed in Table 3.1. The contributions from the individual partial waves are summed as in Eq. (2.110) until a convergence of the state-selective cross section is achieved. The total cross section then can be obtained from the sum of state-selective cross sections. The results over the energy range from 0.1 meV/u to 1 keV/u are illustrated in Fig. 3.5 for total cross sections and state-selective cross sections of reactions (3.1) and (3.2), which are endoergic and exoergic respectively. In our calculation, reaction (3.1) includes five channels, 1 $^2\Sigma^-$, 1 $^2\Pi$, 2 $^2\Sigma^-$, 2 $^2\Pi$, and 2 $^2\Delta$, while there are three channels including 1 $^4\Sigma^-$, 1 $^4\Pi$, and 2 $^4\Sigma^-$ in reaction (3.2). It is clear from the cross sections that for the energy region between 10 and 500 eV/u capture into $N(2p^3 {}^4S^o)$ is the dominant path. As the collision energy approaches 1.53 eV/u, cross sections for capture into the $N(2p^3 {}^2D^o)$ decrease rapidly to zero because of the approach of the $N(2p^3 {}^2D^o)$ + H⁺ threshold. In addition, from the inset plot of Fig. 3.5, we find several orbiting resonances [32] due to quasibound rovibrational states of the quasimolecule. Although these features have been found and studied theoretically in different collision systems [40], there is still no experimental verification. On the other hand, cross sections for capture into the $N(2p^3 {}^4S^o)$ display Langevin behavior [34] at the lowest energies. Later we will also see this behavior exhibited in the rate coefficients (see Fig. 3.7) that tend to a constant in the corresponding temperature range. Again referring to Fig. 3.5, the comparison of the total cross sections of the present work to experimental results [41] shows the best agreement in the energy region above 100 eV/u, but with significant discrepancies for lower energies. The discrepancies are likely related to uncertainties in the incident ion beam and the neutral target. A significant fraction of the incident beam may have included metastable N⁺ and doubly charged molecular ions.

The cross sections for charge transfer processes in the collision of atomic nitrogen with H^+ are presented in Fig. 3.6. We find numerous orbiting resonances in the low energy region for each process. For the collision of $N(2p^3 \ ^4S^o)$ with H^+ , comparisons with the calculations of Kimura *et al.* [42] and Cabrera-Trujillo *et al.* [43] illustrate that the theoretical results, all

obtained with different methods, are in good agreement except for the low energy portion of the calculation of Kimura *et al.* In addition, we also display the experimental results of Gilbody *et al.* [44] in Fig. 3.6, but for collisions of protons with N₂; the concept of additivity appears not to be valid for this collision system, at least for energies less than 1 keV/u. For collisions of metastable $N(2p^3 \ ^2D^o)$ with H⁺, we are unaware of experimental or other theoretical data with which to compare our results.

3.4.2 Rate Coefficients

In Figs. 3.7-3.8 and Table 3.2, we present the rate coefficients for collisions of N⁺ with atomic hydrogen and H⁺ with atomic nitrogen. The rate coefficients $\alpha(T)$, where T is the temperature, are determined by averaging over the cross section $\sigma(E)$ with the Maxwellian energy distribution,

$$\alpha(T) = \frac{1}{\sqrt{\pi\mu}} \left(\frac{2}{k_b T}\right)^{3/2} \int_0^\infty \sigma(E) E \exp\left(-E/k_b T\right) dE, \tag{3.3}$$

where k_b is the Boltzmann constant and μ is the reduced mass of the system.

In Fig. 3.7, because reaction (3.1) is endoergic, the rate coefficient drops abruptly to zero as T approaches the threshold. On the contrary, the exoergic reaction (3.2), tends to a constant. The rate coefficient also displays slight fluctuations due to the orbiting resonances in the cross sections. For reaction (3.2), the results of Steigman *et al.* [45] are much larger than all other calculations. Comparing our total rate coefficients to the calculations of Butler and Dalgarno [46], we find their results are also larger below $\sim 20{,}000$ K, but become smaller than the current results above $\sim 20{,}000$ K. The discrepancy is related to the consideration of different coupling mechanisms in the calculations: spin-orbit between the 1 $^4\Sigma^-$ and 1 $^2\Pi$ states in the earlier work and nonadiabatic radial and rotational interactions in the current study. Therefore an estimate of the total rate coefficients can be obtained by summing the results from both mechanisms with spin-orbit coupling dominating below $\sim 20{,}000$ K, and radial/rotational coupling the primary mechanism above $\sim 20{,}000$ K.

Rate coefficients for the reverse of reactions (3.1) and (3.2) are presented in Fig. 3.8. For the reverse of reaction (3.2), our results are smaller than the predictions of Kimura $et\ al.$ and Steigman $et\ al.$ The former discrepancy is consistent with the observation (see Fig. 3.6) that our cross sections are smaller than those of Kimura $et\ al.$ for energies less than 100 eV/u. The rate coefficients of Kingdon and Ferland [47] were obtained by applying detailed-balance to the spin-orbit rate coefficients of Butler and Dalgarno. Again they are larger than the current results for temperatures less than or approximately equal to 20,000 K. A reasonable estimate of the total rate coefficient for the reverse of reaction (3.1) could be obtained by summing the two results. Finally, no data exists for the metastable nitrogen reaction, the reverse of process (3.2). The rate coefficient for the process is expected to approach a constant, but apparently for temperatures less than $\sim 10\ \text{K}$.

3.5 Astrophysical Implications

Nitrogen is the sixth most cosmically abundant element and as such has been observed in a variety of astrophysical and atmospheric environments. In particular, the role of the charge exchange reaction (3.2) and its reverse in photoionized gas has been investigated recently. Kingdon and Ferland [48] have studied the role of exothermic charge transfer reactions, such as process (3.2), on the thermal equilibrium of photoionized nebulae. For a typical model of a nova shell, they found that charge transfer could contribute up to \sim 60 percent of the total heating with most of the contribution coming from reaction (3.2). Therefore, the magnitude of charge transfer heating is dependent on the value of the rate coefficients for this reaction. In another example, a discrepancy has been known for many years between the observed and predicted emission line ratios of N to N⁺ in narrow line region clouds of Seyfert 2 galaxies. Oliva, Marconi, and Moorwood [49] have proposed through extensive modeling that if the rate coefficients for reaction (3.2) and its reverse are reduced by a factor of \sim 30, then the discrepancy could be resolved. In both cases, the modeling was carried out with the spectral synthesis code Cloudy [2] which incorporates the charge transfer rate coefficients of Butler

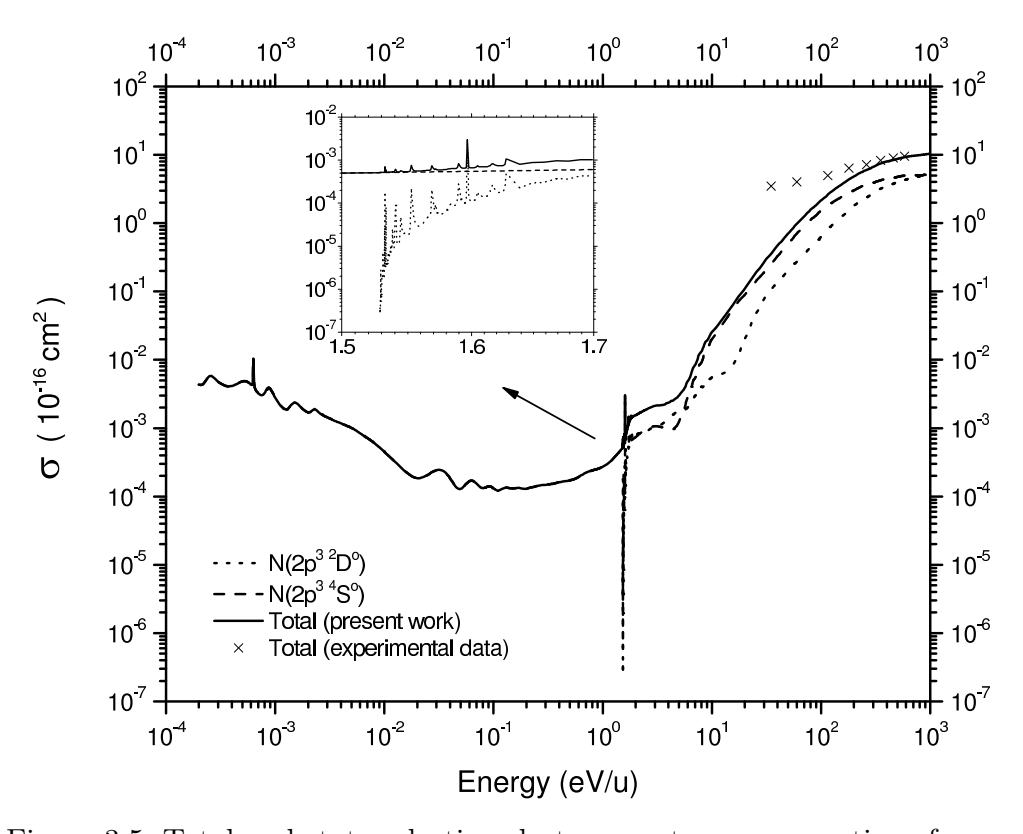


Figure 3.5: Total and state-selective electron capture cross sections for $N^+ + H \rightarrow N + H^+$. The dashed and dotted line are state-selective cross sections. The final states of N are indicated in the figure. Solid line and \times are total cross sections for the present work and the measurement of Stebbings *et al.* [41].

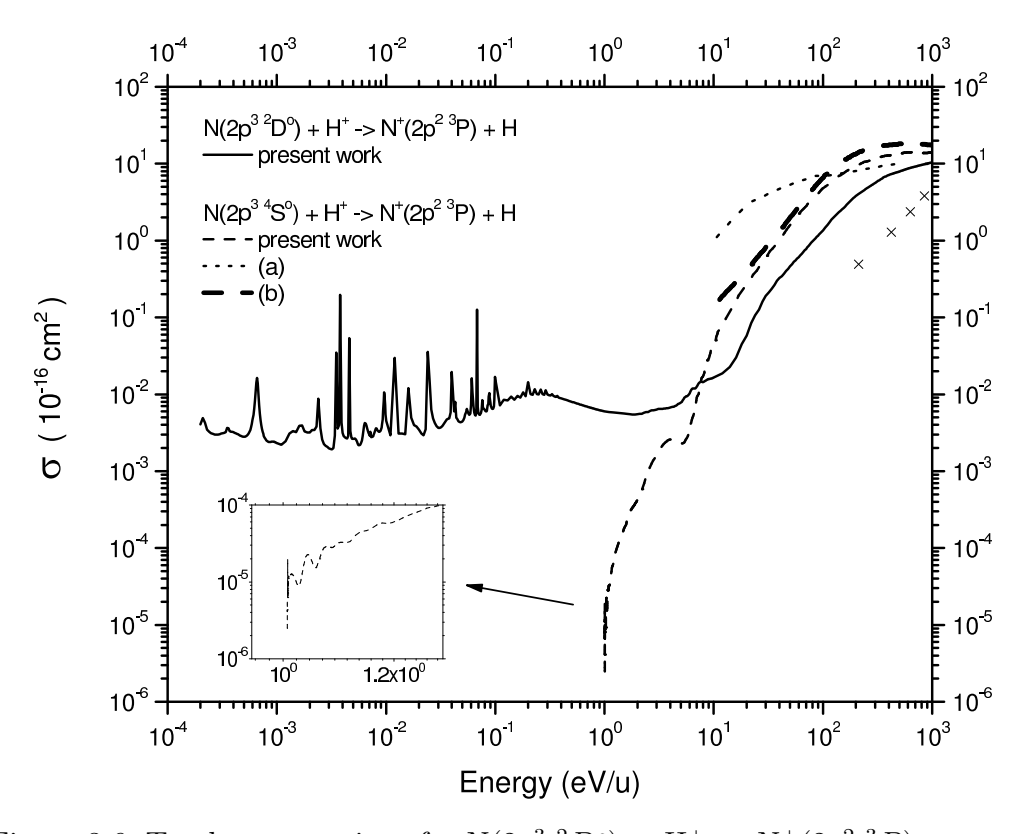


Figure 3.6: Total cross sections for N(2 p^3 $^2D^o$) + H⁺ \rightarrow N⁺(2 p^2 3P) + H (solid line) and N(2 p^3 $^4S^o$) + H⁺ \rightarrow N⁺(2 p^2 3P) + H (non-solid line: (a) Kimura et~al.~[42]; (b) Cabrera-Trujillo et~al.~[43]). The experimental values of Gilbody et~al.~[44], indicated by \times , are for proton collisions on N₂.

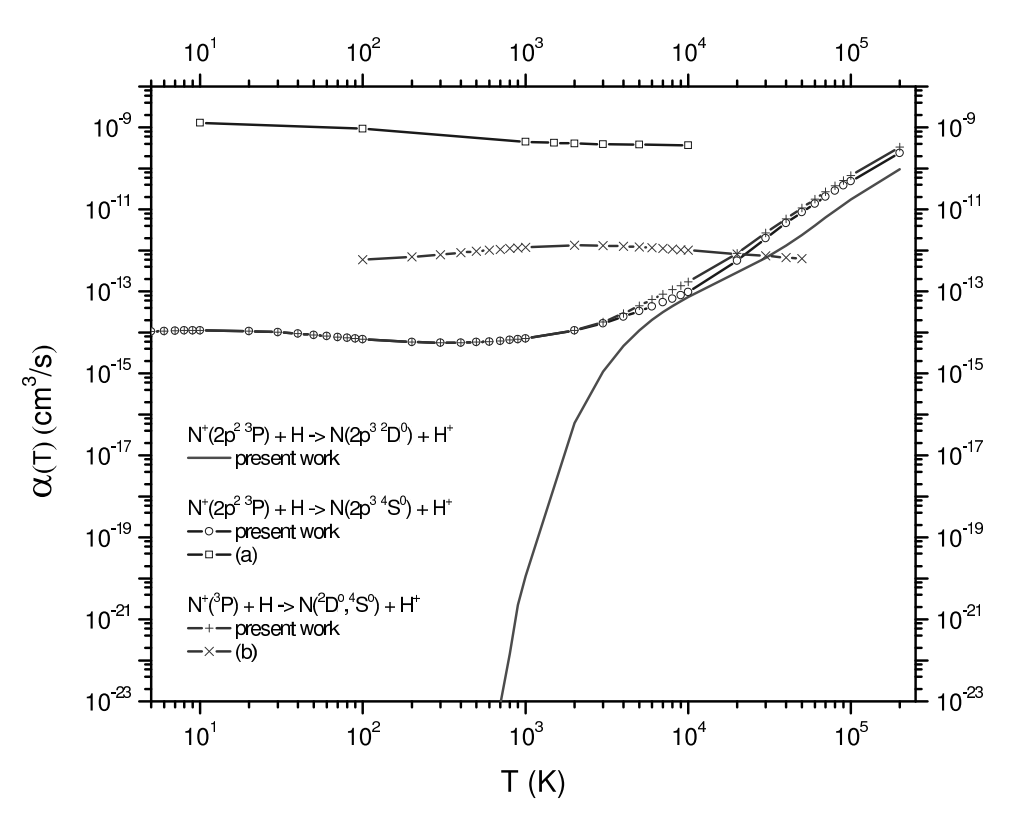


Figure 3.7: Rate coefficients for the collision of N^+ with atomic hydrogen as a function of temperature T. (a) and (b) refer to calculations of Steigman *et al.* [45] and Butler and Dalgarno [46], respectively.

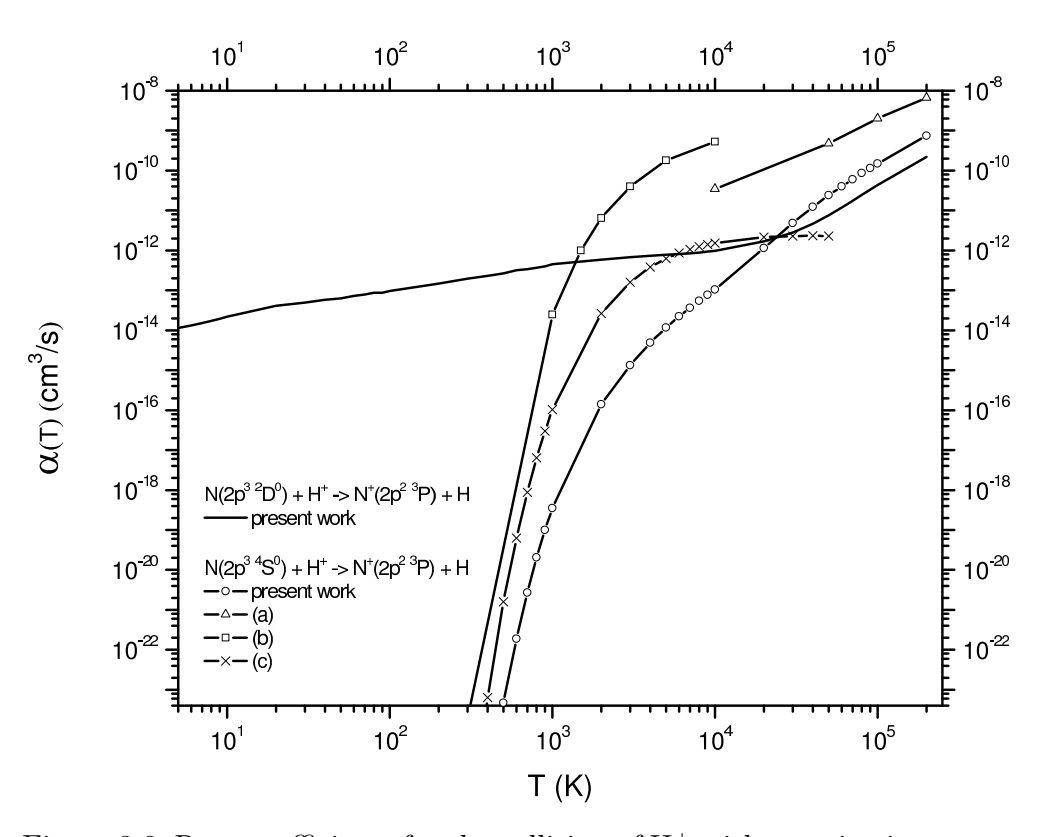


Figure 3.8: Rate coefficients for the collision of H^+ with atomic nitrogen as a function of temperature T. (a), (b), and (c) refer to calculations of Kimura et~al.~[42], Steigman et~al.~[45], and Kingdon and Ferland [47], respectively.

Table 3.2: Rate coefficients for electron capture from collisions of (a): $N(2p^3\ ^2D^o)$ and (b): $N(2p^3\ ^4S^o)$ with H^+ , and for electron capture into (c): $N(2p^3\ ^4S^o)$ and (d): $N(2p^3\ ^2D^o)$ from $N^+(2p^2\ ^3P)$ + H. (e): total rate coefficients for reactions (c) and (d).

T(V)	Rate Coefficients $\alpha(T)$ (cm ³ /s)							
T(K)	(a)	(b)	(c)	(d)	(e)			
6	$1.32(-14)^a$		1.08(-14)		1.08(-14)			
8	1.73(-14)		1.12(-14)		1.12(-14)			
10	2.20(-14)		1.13(-14)		1.13(-14)			
20	4.09(-14)		1.09(-14)		1.09(-14)			
40	5.82(-14)		9.36(-15)		9.36(-15)			
60	7.31(-14)		8.21(-15)		8.21(-15)			
80	8.68(-14)		7.42(-15)		7.42(-15)			
100	9.60(-14)		6.90(-15)		6.90(-15)			
200	1.47(-13)		5.83(-15)		5.83(-15)			
400	2.33(-13)		5.64(-15)		5.64(-15)			
600	3.20(-13)	1.88(-22)	6.00(-15)		6.00(-15)			
800	3.72(-13)	2.05(-20)	6.55(-15)	1.44(-22)	6.55(-15)			
1000	4.49(-13)	3.52(-19)	7.19(-15)	1.14(-20)	7.19(-15)			
2000	5.89(-13)	1.40(-16)	1.12(-14)	6.13(-17)	1.13(-14)			
4000	7.28(-13)	4.91(-15)	2.41(-14)	4.71(-15)	2.89(-14)			
6000	8.08(-13)	2.24(-14)	4.31(-14)	2.02(-14)	6.35(-14)			
8000	8.87(-13)	5.49(-14)	6.65(-14)	4.43(-14)	1.11(-13)			
10000	9.84(-13)	1.06(-13)	9.62(-14)	7.39(-14)	1.70(-13)			
20000	1.68(-12)	1.14(-12)	5.64(-13)	2.92(-13)	8.56(-13)			
40000	4.64(-12)	1.24(-11)	4.65(-12)	1.31(-12)	5.96(-12)			
60000	1.17(-11)	4.00(-11)	1.39(-11)	4.06(-12)	1.80(-11)			
80000	2.46(-11)	8.59(-11)	2.87(-11)	9.37(-12)	3.81(-11)			
100000	4.33(-11)	1.51(-10)	4.94(-11)	1.73(-11)	6.68(-11)			
200000	2.18(-10)	7.50(-10)	2.40(-10)	9.63(-11)	3.37(-10)			

^aThe notation A(-B)= $A \times 10^{-B}$.

and Dalgarno [46] for these two processes. Further, the relevant temperatures are between ~9000 and 18,000 K. The current rate coefficients, due to radial and rotational coupling, are significantly smaller than the spin-orbit results of Butler and Dalgarno, which were obtained with an approximate spin-orbit coupling value. If this value proves to be overestimated, the discrepancy in the Seyfert 2 galaxy line ratios would be resolved, but the role of charge exchange heating would be reduced. A complete close-coupling calculation involving radial, rotational, and spin-orbit coupling is needed which would be the first of its type that we are aware of. Further, we are unaware of measurements in an energy regime where spin-orbit coupling dominates.

3.6 Summary

We have investigated electron capture in collisions of N⁺ with H and H⁺ with N. Comparison with the existing experimental data suggests that total cross sections from the quantum-mechanical MOCC approach gives reasonable results. The discrepancies at low energy with the measurements of Stebbings *et al.* may be due to considerable experimental uncertainties in the knowledge of the reactant and product species. Further, comparison of the two state-selective cross sections, reveals that $N^+(2p^2 \,^3P^o) + H \rightarrow N(2p^3 \,^4S^o) + H^+$ dominates the total cross section in the low energy regime. However, it becomes nearly equal to capture to the excited state $N(2p^3 \,^2D^o)$ at higher energies. For the collision of N with H⁺, our calculation is very similar to the theoretical results of Cabrera-Trujillo *et al.* and is in good agreement with the calculation of Kimura *et al.* at the highest energies, but not for energies less than $100 \, \text{eV/u}$. Total and state-selective measurements are needed for these collision systems.

Rate coefficients given by our calculations are smaller than those reported by Steigman et al. and Kimura et al. Comparisons with the work of Butler and Dalgarno suggests that radial and rotational coupling is the dominant mechanism for temperatures above $\sim 20,000$ K, while spin-orbit coupling dominates at lower temperatures.

Chapter 4

Elastic and inelastic processes in collisions of Na(3s,3p) with He from thermal energies to the ultracold

Elastic and inelastic low-energy collisions of sodium due to helium are investigated using the quantum-mechanical close-coupling method with molecular wave functions. The calculations adopt adiabatic potentials and nonadiabatic radial and rotational couplings obtained with the MRD-CI approach. The potentials are fitted to long-range dispersion coefficients and adjusted with a model interaction in the van der Waals well region. Collisional cross sections for energies between 0.1 peV and 10 eV and rate coefficients as a function of temperature between 10 μ K and 10,000 K are obtained for elastic scattering, Na(3 $p \rightarrow 3s$) quenching, and Na(3 $s \rightarrow 3p$) excitation. The variation of the scattering lengths with reduced mass and collision energy at ultracold temperatures for the 1 $^2\Sigma^+$ and 2 $^2\Sigma^+$ states are presented and their relation to vibrational bound states are illustrated. The results are relevant to studies of cold atom collisions between alkali and rare-gas pairs and, in the thermal regime, modeling NLTE effects in Na D absorption lines in extrasolar planets and brown dwarfs.

4.1 Introduction

In 2001, Charbonneau et al. [50] made the first observation of an atmospheric constituent in an extrasolar planet. In a transit observation, they detected sodium absorption in the extrasolar giant plant (EGP) HD 209458b. However, the inferred absorption was only half the expected value leading Barman et al. [51] to suggest that the electronic states of Na were not in equilibrium. In order to explore the mechanism for the decrease in sodium absorption, well-determined collisional cross section for interactions of Na with the main atmospheric

constituents, H_2 and H_2 are necessary. In particular, electronic excitation processes by neutral species become dominant in cool atmospheric environments due to the small electron abundance.

Although the electronic excitation process of ground state sodium atoms in collisions with ground state helium has been investigated in a number of theoretical [52, 53, 54, 55] and experimental [56, 57, 58] studies, the available data are all above 100 eV. The thermal regime has been relatively unexplored except for studies on fine-structure branching fractions in optical collisions [59] and collisional broadening of Na resonance lines [60]. To shed further light on this problem, we apply the quantum-mechanical coupled-channel (CC) method, which adopts a perturbed stationary state expansion of the molecular wave functions, to this collision system with the ultimate aim of extending the cross section down to threshold to provide data relevant for astrophysical modeling.

Collisions of alkali and rare-gas atoms are also of interest in the ultracold regime as highlighted in the recent special issue on cold collisions and cold molecules [61]. In this work, we explore the elastic scattering processes

$$Na(3s {}^{2}S) + He \rightarrow Na(3s {}^{2}S) + He,$$
 (4.1)

$$Na(3p\ ^2P^o) + He \rightarrow Na(3p\ ^2P^o) + He,$$
 (4.2)

and inelastic quenching and excitation

$$\operatorname{Na}(3s {}^{2}S) + \operatorname{He} \leftrightarrow \operatorname{Na}(3p {}^{2}P^{o}) + \operatorname{He},$$
 (4.3)

for energies between 0.1 peV and 10 eV. Total elastic cross sections are analyzed by partial-wave contributions to illustrate the significance of small partial waves in the low-energy regime. For Σ states, elastic cross sections are characterized by scattering lengths at the zero-energy limit. In addition, the sign of the scattering length reflects features of the potential curves. The sensitivity of the scattering length to the potential is investigated by varying the reduced mass of the system. The dramatic variation of the scattering length due to bound states produced by mass-scaled potentials is also illustrated.

A description of the theoretical method was presented in Chapter 2 for scattering calculations and in Section 4.2 for the current molecular structure. In Section 4.3, the adiabatic potentials and nonadiabatic couplings of Na-He are discussed. The resulting cross sections and rate coefficients are given in Sections 4.4.1 and 4.4.2. The variation of the scattering lengths with reduced mass and collision energy are displayed and discussed in Section 4.4.3. Sections 4.5 and 4.6 discuss astrophysical implications and summarize this chapter, respectively.

4.2 Electronic Structure Calculations

The *ab initio* adiabatic potentials and nonadiabatic couplings are obtained with the MRD-CI method which has been detailed previously by Buenker and coworkers [35, 63, 37, 62, 63]. Here only descriptions relevant to the present calculation is specified. The basis functions for the molecular calculations consist of contracted Gaussian-type functions which have the form,

$$N_n r^{n-1} e^{-\zeta r^2} Y_{lm}(\Omega), \tag{4.4}$$

where N_n is the normalization constant and Y_{lm} is a spherical harmonic. The (5s4p3d) basis for the helium atom [64] is contracted to [4s4p2d] including one s-, one p-, and one d-type diffuse functions with exponents which are 0.027, 0.023, and 0.020 respectively. For the sodium atom [65], the (15s9p5d) basis is contracted to [9s7p5d] including one s-, one p-, and one d-type diffuse functions with exponents which are 0.023, 0.021, and 0.018, respectively. The finite difference technique [38, 39] has been applied to obtain radial couplings (matrix elements of $\partial/\partial R$), while rotational couplings have been calculated by employing appropriate pairs of CI eigenfunctions. All couplings have been computed with the electronic coordinate origin at the center of mass of the Na-He system.

4.3 POTENTIALS AND COUPLINGS

For low-energy collisions of Na(3s,3p) with He, the major effects and interactions for this system are dominated by three molecular states, $1^{2}\Sigma^{+}$, $1^{2}\Pi$, and $2^{2}\Sigma^{+}$, and three couplings connecting them. For the present scattering calculations, adiabatic potentials for these states are fitted to long-range dispersion coefficients and adjusted with a model interaction in the van der Waals well region. We used *ab initio* data calculated with the MRD-CI method as a function of internuclear distance R from 0.2 to 9.5 a.u. For R greater than 9.5 a.u., the model potential proposed by Cvetko *et al.* [66],

$$U(R) = \frac{C_6}{120} \left(\frac{b}{3}\right)^6 \left(ae^{-bR} - \chi e^{-(2/3)bR} - e^{-(1/3)bR}\right), \qquad bR \le 16.6, \tag{4.5}$$

was used to join the van der Waals well region smoothly to the long-range part of the potentials, while the long-range potential is described by

$$U(R) = \frac{C_6}{120} \left(\frac{b}{3}\right)^6 a e^{-bR} - \frac{C_6}{R^6} - \frac{C_8}{R^8} - \frac{C_{10}}{R^{10}} \qquad bR \ge 16.6.$$
 (4.6)

The parameters adopted for each molecular state are listed in Table 4.1, where the C_6 coefficients are taken from Zhu et~al.~[67] and the others are obtained by fitting to the ab~initio data. We also present in Table 4.1, the equilibrium separations r_m and well depths ϵ obtained from our fits. Compared to other theoretical predictions of the dispersion coefficients [68, 69, 70], the C_6 , C_8 and C_{10} that we utilize for the 1 $^2\Sigma^+$ state are in good agreement. We are unaware of other determinations of C_8 and C_{10} for the excited states. r_m and ϵ for the ground state are within 1% and 3%, respectively, of the values computed in Refs. [66] and [69]. While similar parameters have not been previously reported for the 2 $^2\Sigma^+$, our r_m is within the uncertainty of the measurement of Havey, Frolking, and Wright [71] for the 1 $^2\Pi$ state. However, our well depth is 38% larger than the experimental value [71]. As the internuclear distance approaches infinity, these three molecular states degenerate into two separated-atom states which are Na(3s 2S) + He and Na(3p $^2P^o$) + He as given in Table 4.2.

For couplings driving the transitions between different molecular states, there are two nonadiabatic rotational couplings, which result from the interaction between molecular states

Table 4.1: Parameters of long-range potentials for 1 $^2\Sigma^+$, 1 $^2\Pi$, and 2 $^2\Sigma^+$ corresponding to Eqs. (4.5) and (4.6). Also listed are the equilibrium distances r_m and well depths ϵ . All values are given in atomic units.

Molecular	a	b	χ	C_6	C_8	C_{10}	r_m	ϵ
$\frac{\text{States}}{1^{2}\Sigma^{+}}$	4345.27	1.00	86.763	25.1	1328.00	95140.00	12.0	$5.95(-6)^{b}$
$1 \ ^2\Pi$						10712.99		()
$2^{2}\Sigma^{+}$	8400.00	0.63	86.031	79.5	10656.51	1856973.87	21.5	5.82(-7)

^bThe notation A(-B)= $A \times 10^{-B}$.

Table 4.2: Comparison of asymptotic separated-atom energies between the MRD-CI calculations and experiment for the lowest three molecular states of Na-He.

110 110.				
Separated-atom	Experimental	Theoretical	Molecular	United-atom
States	Energies ^{c} (eV)	Energies (eV)	States	States
$Na(3s^2S) + He$	0.0	0.0	$1^{2}\Sigma^{+}$	$Al(3p^2P^o)$
$Na(3p^2P^o)+He$	2.1037	2.0768	$1^2\Pi$	$Al(3p^2P^o)$
		2.0868	$2^2\Sigma^+$	$Al(4s^2S)$

^cNIST Atomic Spectra Database, http://physics.nist.gov/PhysRefData/ASD/index.html.

with different symmetry $(\Lambda = \Lambda' \pm 1)$, and one nonadiabatic radial coupling, which is due to the interaction between molecular states with the same symmetry $(\Lambda = \Lambda')$.

A unitary transformation [23] is applied to transform the potentials and couplings into a diabatic representation as described in Section 2.3. The adiabatic and diabatic potentials are displayed in Fig. 4.1. The largest modification due to the unitary transformation is for the 1 $^{2}\Sigma^{+}$ and 2 $^{2}\Sigma^{+}$ potentials. In Fig. 4.2, the nonadiabatic radial coupling, 1 $^{2}\Sigma^{+}$ -2 $^{2}\Sigma^{+}$,

and the corresponding diabatic potential coupling are displayed. Two rotational couplings are presented in Fig. 4.3, where the coupling between states $2^{2}\Sigma^{+}$ and $1^{2}\Pi$ approach a constant with increasing R. This will be seen to have a great influence on the collision dynamics of the $2^{2}\Sigma^{+}$ state in the low-energy region.

4.4 RESULTS AND DISCUSSION

4.4.1 Cross Sections

For the elastic scattering process (4.1), the molecular state 1 $^2\Sigma^+$ dominates the interaction in the low-energy region. For the elastic scattering process (4.2), the collision cross sections of 1 $^2\Pi$ and 2 $^2\Sigma^+$ are not only dominated by their individual potentials, but also affected by the nonadiabatic couplings. The total and partial-wave elastic cross sections for the 1 $^2\Sigma^+$ are displayed in Fig. 4.4. The s-wave (J=0) contribution dominates at ultracold energies with the cross section becoming constant for $E<10^{-8}$ eV. The peak of the total cross section at 5 μ eV results from the contribution of the partial wave, J=1, while the J=2 term is responsible for the slight shoulder in the total cross section. The inset of Fig. 4.4 shows the comparison of the present calculations to the theoretical prediction of Bottcher et al. [52] for energies between 0.01 and 1 eV. The small discrepancy is a consequence of the difference in adopted potentials where Ref. [52] used a model potential method with a Hartree-Fock core.

Fig. 4.5 illustrates the total cross sections and the variation with energy of the partial-wave cross sections with J=1-5 for elastic collisions in the 1 $^2\Pi$ state. For this state, we made the approximation that the centrifugal potential is given in Hund's case (b) by $V^c = [J(J+1) - \Lambda^2]/(2\mu R^2)$. The maximum of each partial-wave cross section is primarily influenced by three factors. The partial-wave cross sections are proportional to the inverse of the collision energy, at very low energy, and the total angular momentum. In addition, the orbiting resonances increase the magnitude of partial-wave cross sections dramatically. In Fig. 4.5, it is apparent that there is a resonance due to a quasi-bound state for J=2. As a result of this resonance, a sharp peak is observed in the total cross section. The cross

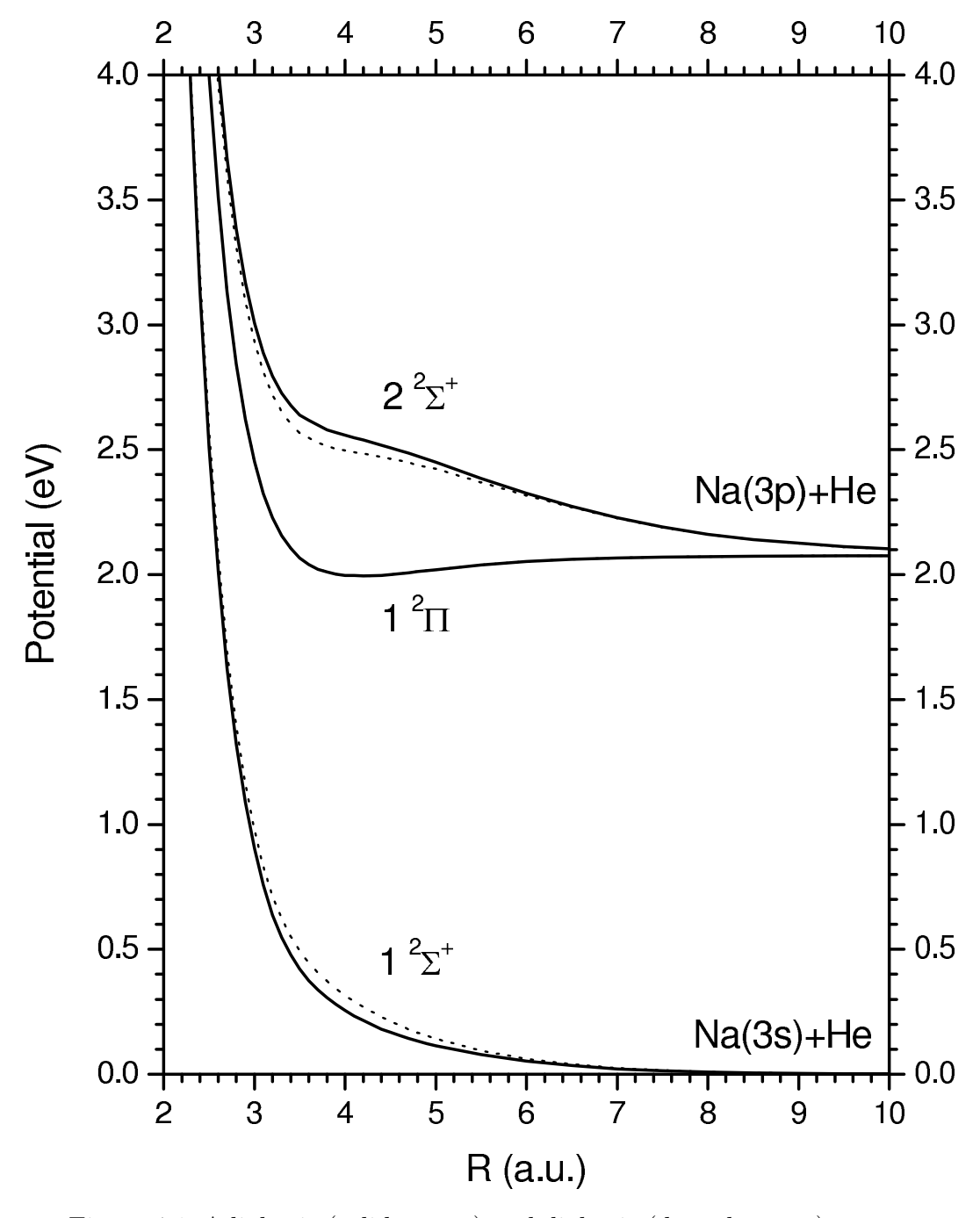


Figure 4.1: Adiabatic (solid curves) and diabatic (dotted curves) potentials for Na-He as functions of internuclear distance R. The adiabatic and diabatic potentials for the $1^2\Pi$ state are indistinguishable.

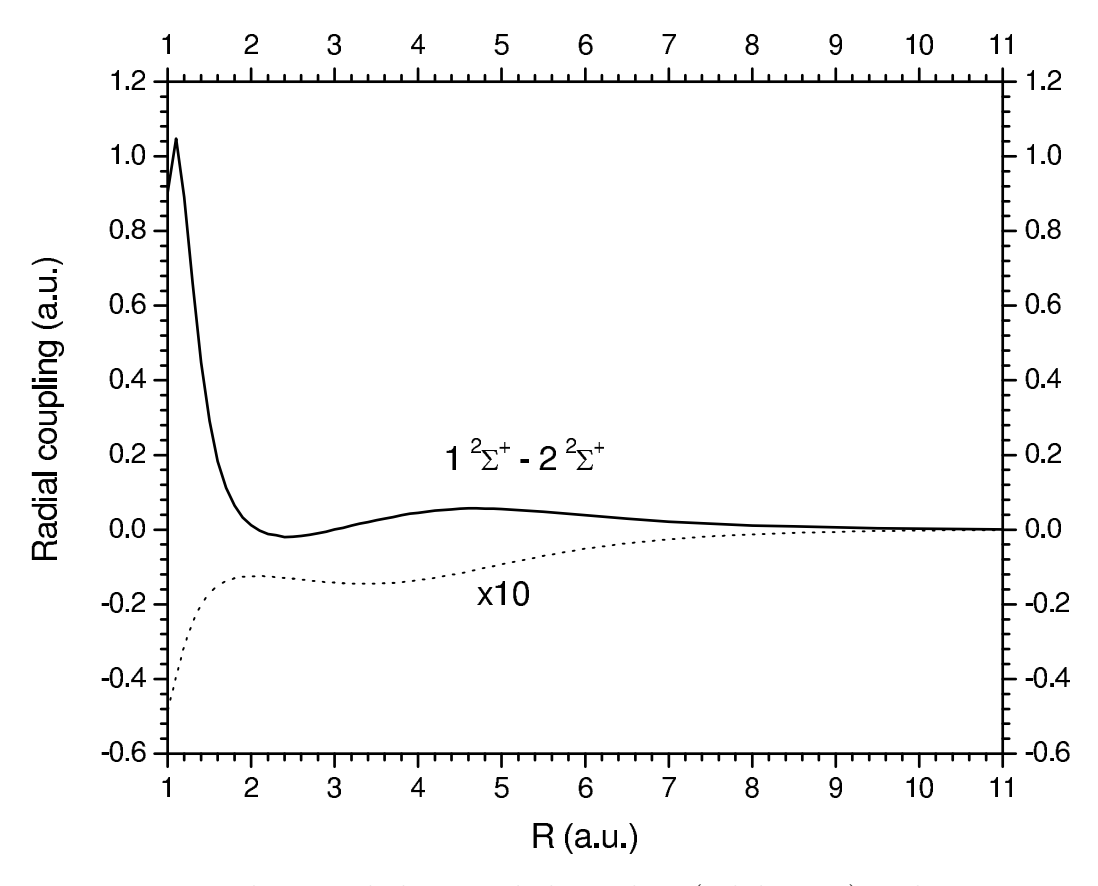


Figure 4.2: The nonadiabatic radial coupling (solid curve) and its corresponding off-diagonal diabatic potential coupling (dotted curve) for Na-He as a function of internuclear distance R. The diabatic coupling is magnified by a factor of 10.

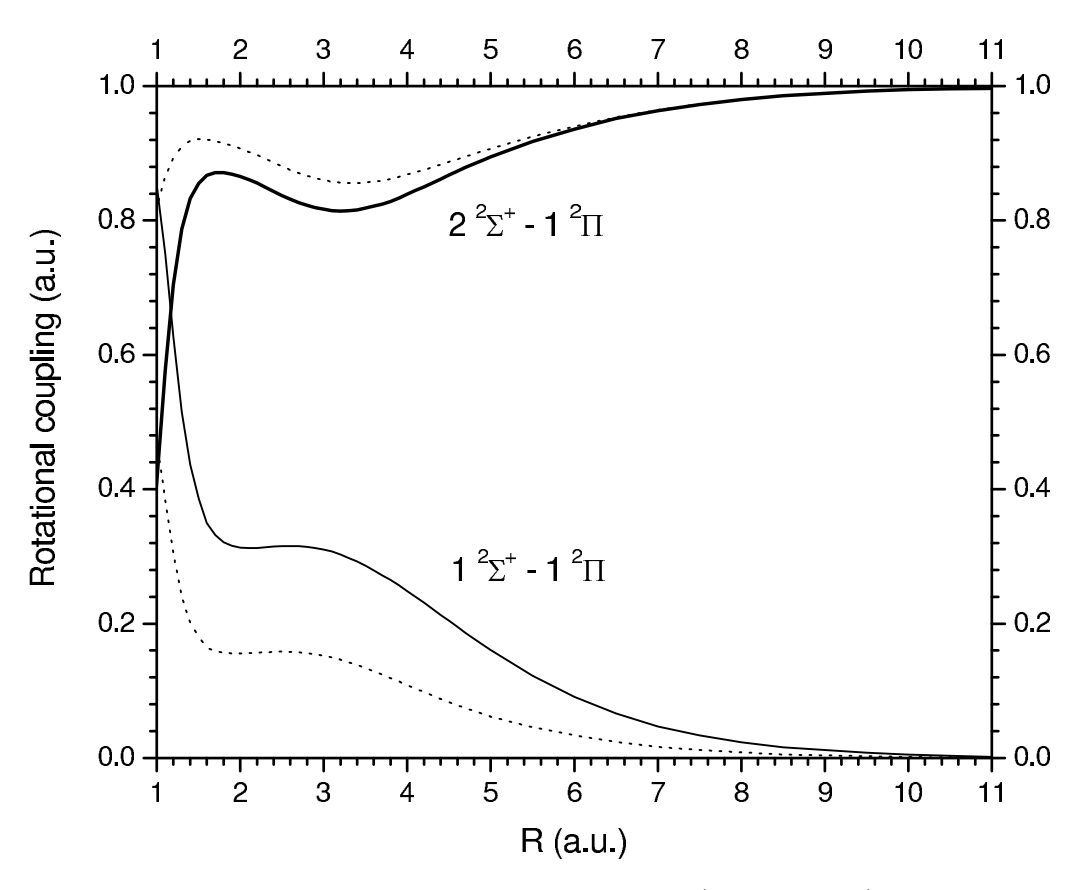


Figure 4.3: Nonadiabatic rotational couplings (solid curves) and their corresponding off-diagonal diabatic couplings (dotted curves) for Na-He as functions of internuclear distance R.

section drops abruptly at energies between 10^{-9} and 10^{-8} eV due to the centrifugal barriers, which increase in height with increasing J. In the higher energy region, the contribution of higher partial waves to the total cross section increases in importance with several hundreds or thousands of partial waves contributing at each energy. Although the maximum of the individual partial-wave cross sections gradually reduces, the sum of thousands of partial waves (not shown) causes the large total cross section at high energy.

For elastic collisions in the 2 $^2\Sigma^+$ state, the total and the J=0-5 partial-wave cross sections are presented in Fig. 4.6. Because the contribution of the J=0 partial wave is small compared with other partial waves, the J=0 term is displayed in the inset which illustrates that J=0 becomes prominent in the low-energy region with the total cross section reaching a finite value in the zero-energy limit. Partial-wave analysis shows that the J=2 term, similar to that of the 1 $^2\Pi$, has a resonance which results in the peak in the total cross sections. The sensitivity of resonances to the potentials and couplings has been discussed by Krems and Dalgarno [72]. We find that the resonances in the 2 $^2\Sigma^+$ cross section disappear if we turn off the 1 $^2\Pi$ -2 $^2\Sigma^+$ coupling; meanwhile, the total cross sections of both the 1 $^2\Pi$ and 2 $^2\Sigma^+$ will be diminished greatly at high energy. Therefore, the resonance in the cross sections of the 2 $^2\Sigma^+$ state is due to a quasi-bound state supported by the 1 $^2\Pi$ potential, which causes the effect through the 1 $^2\Pi$ -2 $^2\Sigma^+$ coupling.

The cross sections for inelastic collision processes (4.3), which include quenching and excitation reactions, are displayed respectively in Fig. 4.7 and Fig. 4.8. The quenching process from Na(3p) to Na(3s) due to collisions of He includes two de-excitation paths, $1^{2}\Pi$ to $1^{2}\Sigma^{+}$ and $2^{2}\Sigma^{+}$ to $1^{2}\Sigma^{+}$. Fig. 4.7 displays the total and state-to-state cross sections compared to the state-to-state results neglecting the $1^{2}\Pi$ -2 $^{2}\Sigma^{+}$ coupling. For energies less than 1 eV, quenching from $1^{2}\Pi$ to $1^{2}\Sigma^{+}$ is the dominant process. Several distinct orbiting resonances appearing in the cross sections are due to quasi-bound states of the quasimolecule. It is worth noting that both different quenching processes have the same resonance position. However, the resonances at energies lower than 0.01 eV have mostly disappeared for the $2^{2}\Sigma^{+}$ to

 $1\ ^2\Sigma^+$ transition when the $1\ ^2\Pi$ - $2\ ^2\Sigma^+$ coupling is set to zero, but they still appear in the $1\ ^2\Pi$ to $1\ ^2\Sigma^+$ quenching cross sections, though reduced in magnitude. This implies that these resonances are due to quasi-bound states supported by the $1\ ^2\Pi$ potential. In addition, for energies less than 10^{-4} eV, the $2\ ^2\Sigma^+$ - $1\ ^2\Sigma^+$ cross section obeys the Wigner threshold law [73] (see thin dotted line in Fig. 4.7), when the $1\ ^2\Pi$ - $2\ ^2\Sigma^+$ coupling is removed. The broad resonance in the quenching cross sections near 10^{-8} eV and the main resonance in the elastic cross sections of the $1\ ^2\Pi$ and $2\ ^2\Sigma^+$ states are close in energy as both are due to the same quasi-bound state provided by the $1\ ^2\Pi$ potential. The broad width of this resonance indicates that the corresponding quasi-bound state has a short lifetime because its position is near the top of the potential barrier. On the other hand, the resonance position is sensitive to the couplings which will shift the position of the quasi-bound state. The magnitude of the resonance near 10^{-8} eV becomes less pronounced when the $1\ ^2\Pi$ - $2\ ^2\Sigma^+$ coupling is removed (see thin dashed line in Fig. 4.7).

The excitation cross sections of Na(3s) to Na(3p) due to He collisions are given in Fig. 4.8. The most significant contribution to total excitation cross sections is through the excitation of molecular state 1 $^2\Sigma^+$ to 2 $^2\Sigma^+$ for energies larger than 2.8 eV. Because of the 2 $^2\Sigma^+$ threshold at 2.1 eV, the cross sections go to zero abruptly as the threshold is approached. The inset details the orbiting resonances occurring near the threshold.

4.4.2 Rate coefficients

The rate coefficients $\alpha(T)$, where T is the temperature, are determined by averaging over the cross section $\sigma(E)$ with the Maxwellian energy distribution, as given by Eq (3.3). In Fig. 4.9, rate coefficients for elastic scattering processes, (4.1) and (4.2), are presented as functions of temperatures between 1 μ K and 100 K for each of the molecular states. The behavior of the rate coefficients for the 1 $^2\Sigma^+$ state is proportional to $T^{1/2}$ because the elastic cross section is constant as the collision energy approaches zero. Similarly, due to nearly constant cross sections in the higher energy region for the 2 $^2\Sigma^+$ and 2 $^2\Pi$ states, the rate coefficients are

$\frac{1}{1}$ (3p \rightarrow 3s) quenching due to comsions with the and 11.					
		$Na(3s \rightarrow 3p)$		$Na(3p \rightarrow 3s)$	
		He	Н	He	Н
		(4,000-10,000 K)	(3,000-10,000 K)	(10-10,000 K)	(3,000-10,000 K)
$\overline{a_1}$	(cm^3/s)	$7.53(-12)^d$	9.567(-12)	4.80(-20)	1.175(-12)
b_1		10.00	10.458	0.39	5.440
c_1	(K)	723.44	1097.773	2000.00	3341.270
a_2	(cm^3/s)	1.55(-9)	2.469(-9)	1.80(-16)	2.108(-11)
b_2		21.00	22.352	3.83	4.198
c_2	(K)	551.40	674.551	3500.00	1279.273

Table 4.3: Fitting parameters of inelastic rate coefficients for Na(3s \rightarrow 3p) excitation and Na(3p \rightarrow 3s) quenching due to collisions with He and H.

also approximately proportional to $T^{1/2}$. On the other hand, the sudden decline of the rate coefficients at temperatures lower than 10^{-4} K for these two states indicates the influence of the centrifugal barrier from the J=1 term. Fig. 4.10 illustrates the variation of rate coefficients with T from 10^{-6} to 10^4 K for inelastic collisions. The rate coefficients are larger for the exoergic reaction, $\text{Na}(3p\ ^2P^o) + \text{He} \rightarrow \text{Na}(3s\ ^2S) + \text{He}$, than for the endoergic reaction, $\text{Na}(3s\ ^2S) + \text{He} \rightarrow \text{Na}(3p\ ^2P^o) + \text{He}$, as expected. For convenience we have fitted the inelastic rate coefficients to the relation

$$\alpha(T) = \sum_{i} a_i \left(\frac{T}{10000}\right)^{b_i} \exp\left(-\frac{T}{c_i}\right). \tag{4.7}$$

The fit coefficients are given in Table 4.3 and are valid for T < 10,000 K.

4.4.3 Scattering Lengths and Ultracold Collisions

As the collisional energy achieves the regime of the zero-energy limit, the scattering length can be used to characterize the scattering. In the present work of multi-channel scattering, taking advantage of the complex scattering length formalism [75, 76] is an useful way to

^dThe notation A(-B)= $A \times 10^{-B}$.

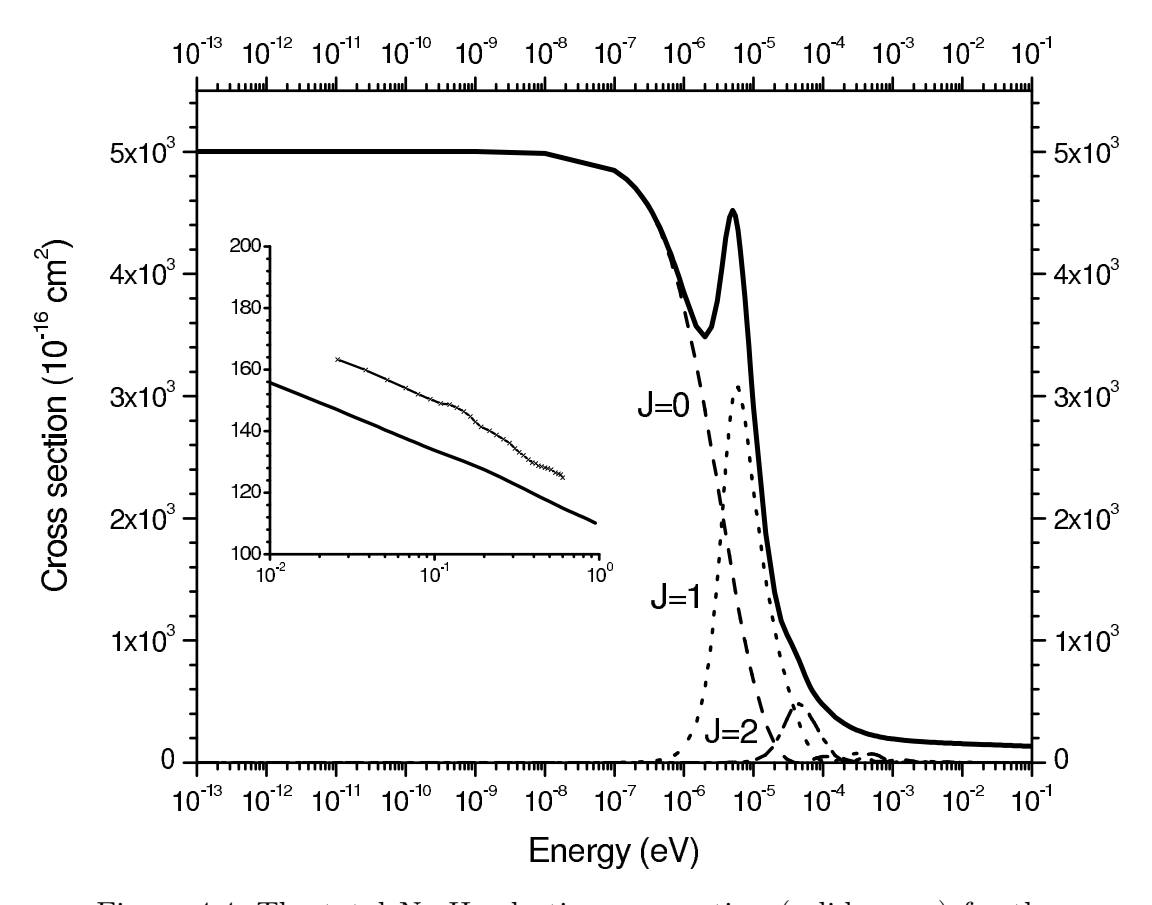


Figure 4.4: The total Na-He elastic cross section (solid curve) for the $1\ ^2\Sigma^+$ state and its partial-wave cross sections for J=0-2 as functions of collision energy. The inset shows the comparison of the total elastic cross section to the results of Bottcher *et al.* [52] (line with x's).

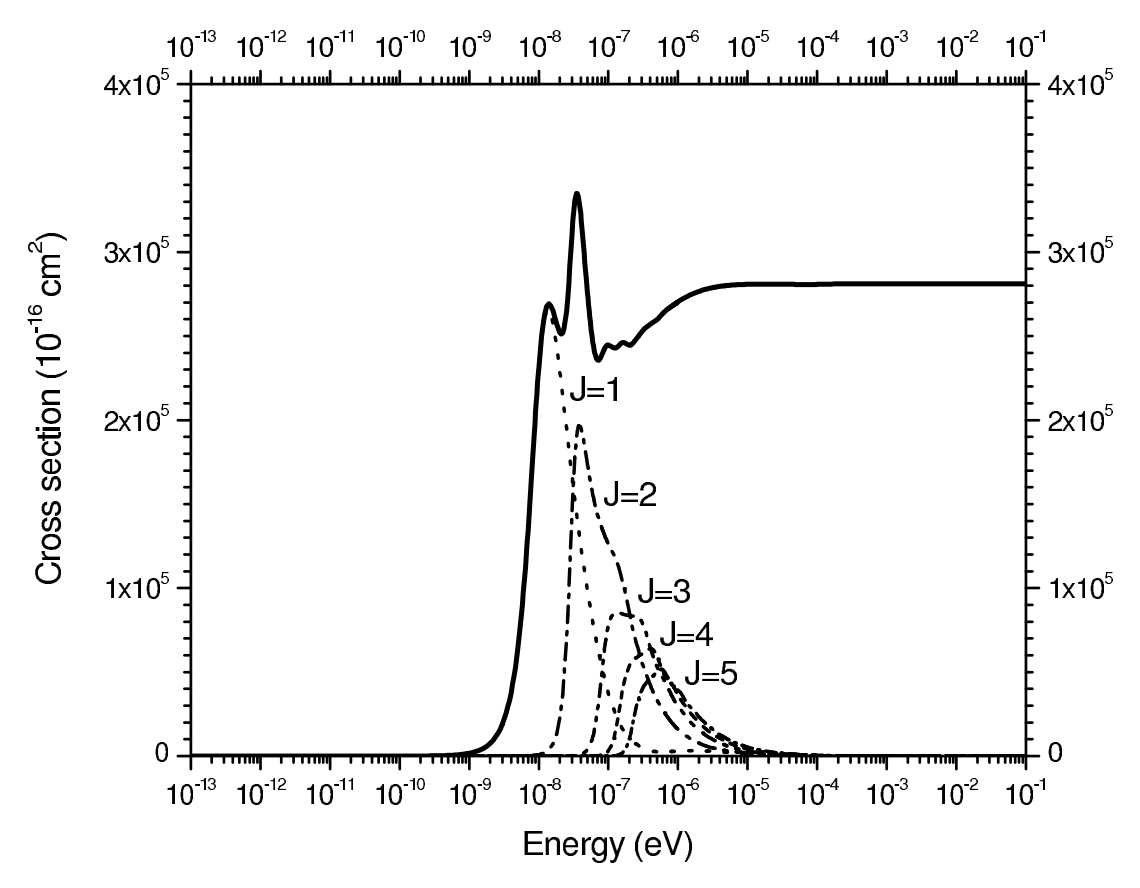


Figure 4.5: The total Na-He elastic cross section (solid curve) for the 1 $^2\Pi$ state and its partial-wave cross sections for J=1-5.

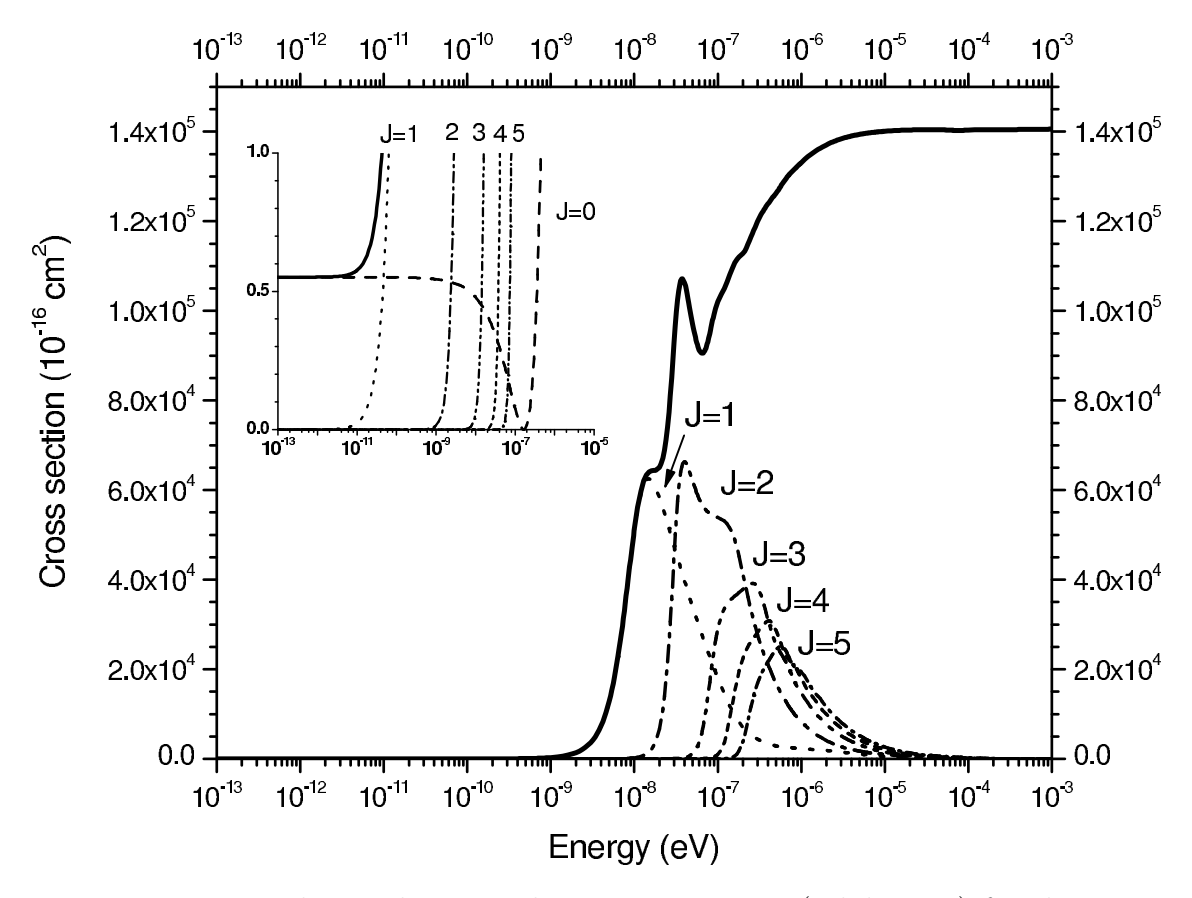


Figure 4.6: The total Na-He elastic cross section (solid curve) for the 2 $^2\Sigma^+$ state and its partial-wave cross sections for $J{=}1{-}5$. The inset shows the zero-energy limit with the J=0 contribution

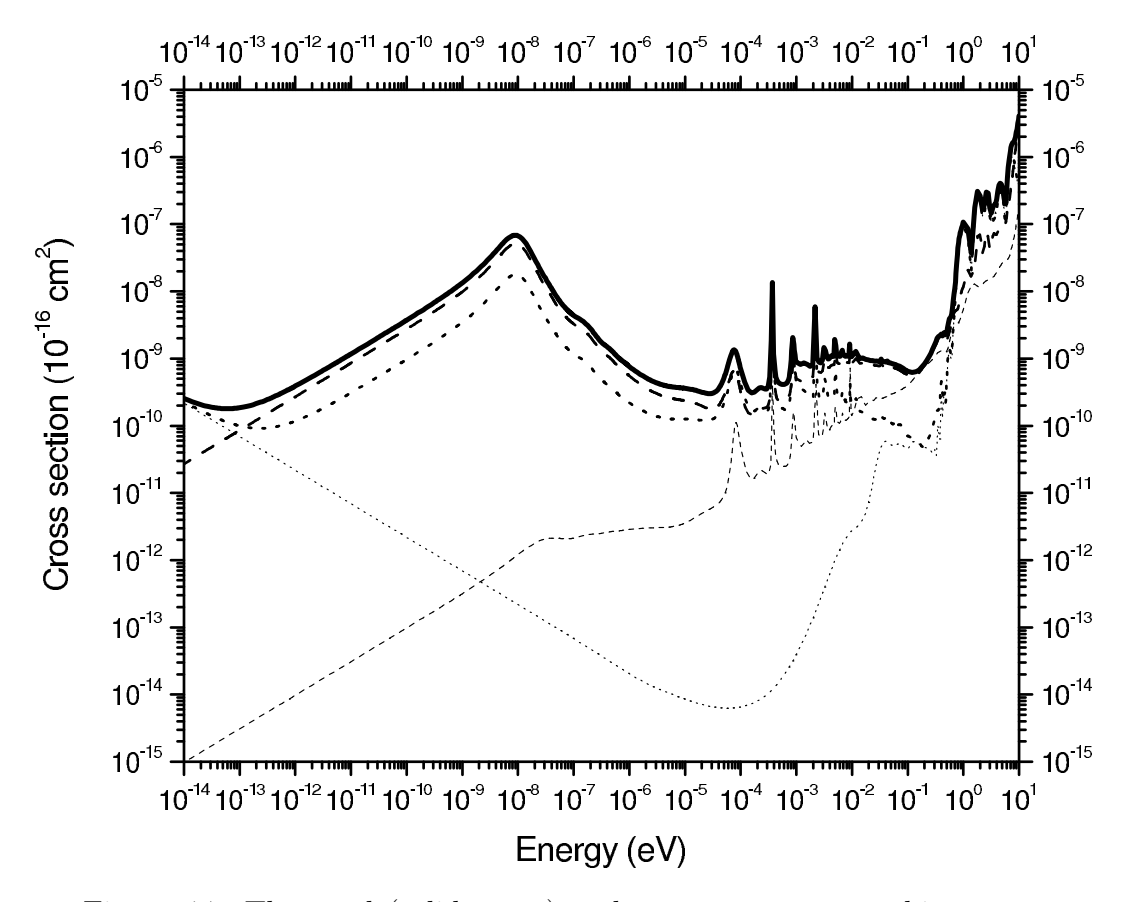


Figure 4.7: The total (solid curve) and state-to-state quenching cross sections for Na-He. The thick dashed curve corresponds to the deexcitation of molecular states from 1 $^2\Pi$ to 1 $^2\Sigma^+$ and thin dashed curve corresponds to the same process, but without including the 1 $^2\Pi$ -2 $^2\Sigma^+$ coupling. The thick dotted curves corresponds to 2 $^2\Sigma^+$ to 1 $^2\Sigma^+$ and thin dotted curve corresponds to the same process, but without 1 $^2\Pi$ -2 $^2\Sigma^+$ coupling.

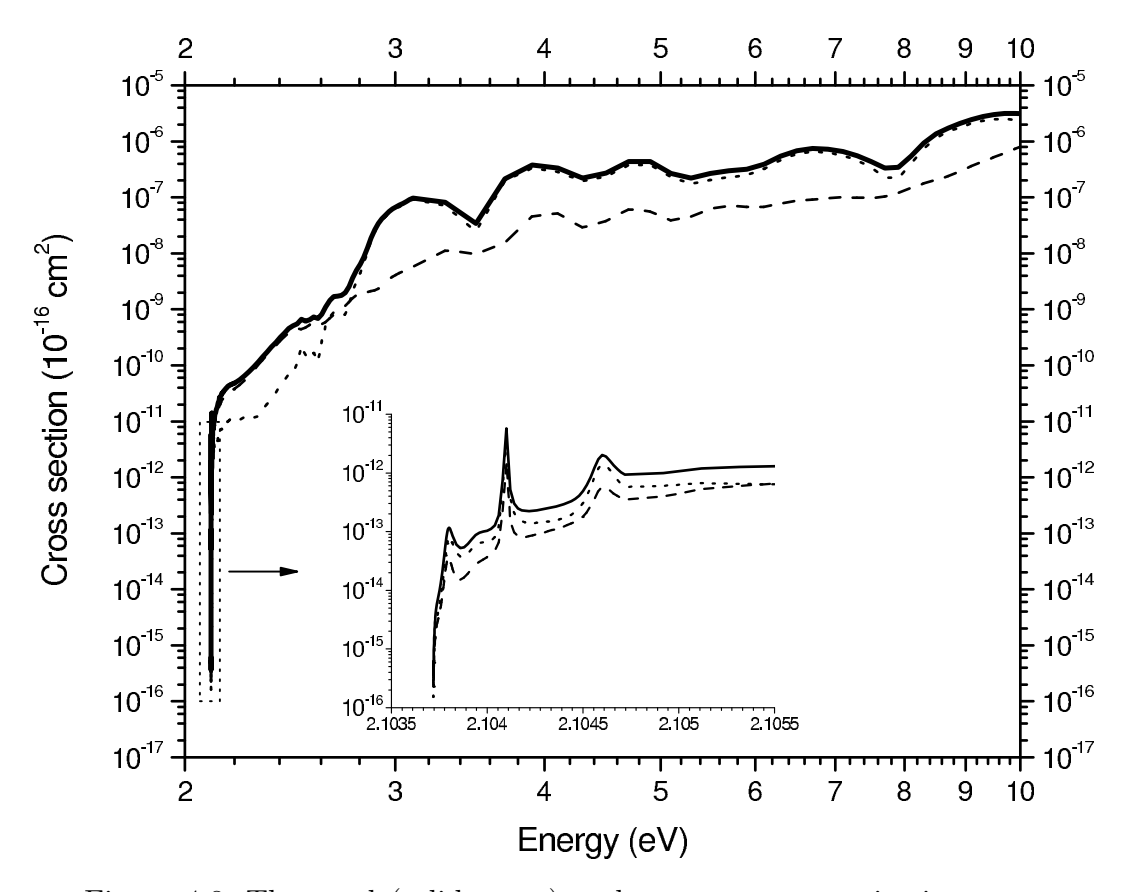


Figure 4.8: The total (solid curve) and state-to-state excitation cross sections for Na-He. The dashed curve corresponds to the excitation of molecular states from 1 $^2\Sigma^+$ to 1 $^2\Pi$ and dotted curves corresponds to that from 1 $^2\Sigma^+$ to 2 $^2\Sigma^+$. The inset shows the energy region near threshold

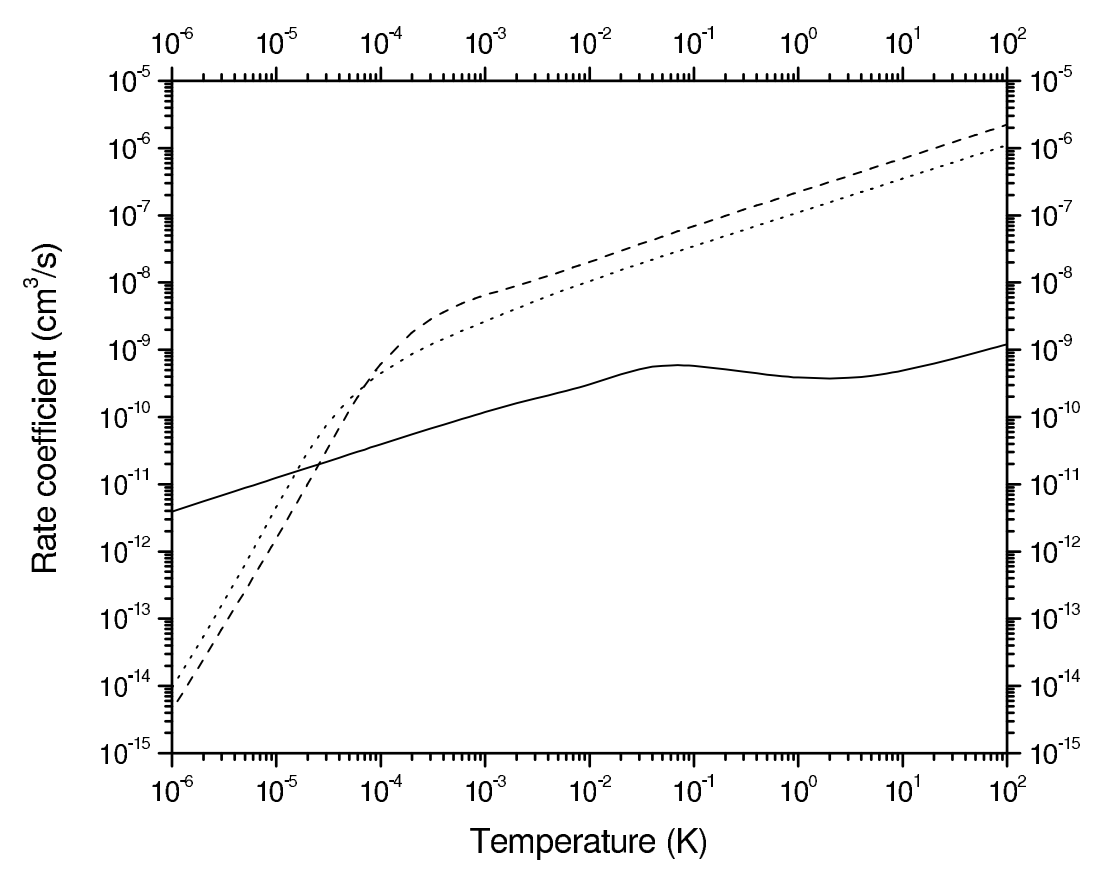


Figure 4.9: Rate coefficients of elastic collision processes as functions of temperature T for Na-He. The solid curve corresponds to the 1 $^2\Sigma^+$, the dashed curve to the 1 $^2\Pi$, and the dotted curve to the 2 $^2\Sigma^+$.

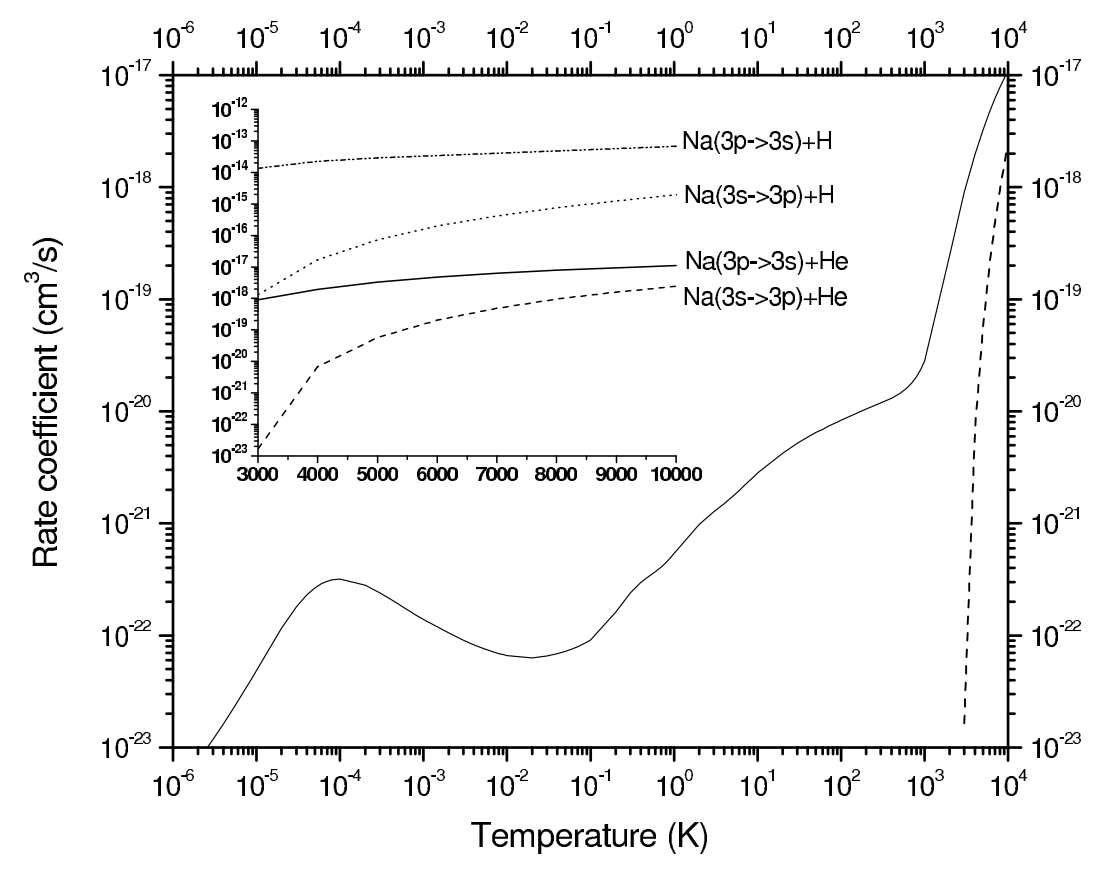


Figure 4.10: Rate coefficients of inelastic collision processes, $\text{Na}(3p\ ^2P^o) + \text{He} \rightarrow \text{Na}(3s\ ^2S) + \text{He}$ (solid curve) and $\text{Na}(3s\ ^2S) + \text{He} \rightarrow \text{Na}(3p\ ^2P^o) + \text{He}$ (dashed curve), as functions of temperature T. The inset displays the rate coefficients for the same Na-He processes compared to those deduced for Na-H collisions from Belyaev *et al.* [74].

incorporate the effect of inelastic collisions into the equivalent one-channel problem. The complex scattering length is defined as

$$a = a^r - ia^i. (4.8)$$

With the relations for the s-wave phase shift, $\delta^0 = -ka$, in the low-energy limit and the S-matrix element,

$$S^{J}_{\alpha\alpha} = e^{i2\delta^{J}_{\alpha}},\tag{4.9}$$

we can obtain

$$Re(S_{\alpha\alpha}^0) = e^{-2k_{\alpha}a_{\alpha}^i}\cos(2k_{\alpha}a_{\alpha}^r)$$
(4.10)

and

$$\operatorname{Im}(S_{\alpha\alpha}^0) = -e^{-2k_{\alpha}a_{\alpha}^i}\sin(2k_{\alpha}a_{\alpha}^r), \tag{4.11}$$

and the complex scattering length can be expressed in terms of the real part of the S-matrix element, $\text{Re}(S_{\alpha\alpha}^0)$, and the imaginary part, $\text{Im}(S_{\alpha\alpha}^0)$, as

$$a_{\alpha}^{r} = \frac{-1}{2k_{\alpha}} \tan^{-1} \left(\frac{\operatorname{Im}(S_{\alpha\alpha}^{0})}{\operatorname{Re}(S_{\alpha\alpha}^{0})} \right)$$
(4.12)

and

$$a_{\alpha}^{i} = \frac{-1}{4k_{\alpha}} \ln\{[\operatorname{Re}(S_{\alpha\alpha}^{0})]^{2} + [\operatorname{Im}(S_{\alpha\alpha}^{0})]^{2}\}.$$
 (4.13)

In the low-energy regime, s-wave scattering dominates. Therefore, for a specific entrance channel α , the elastic and inelastic cross sections, σ_{α}^{el} and σ_{α}^{in} , can be reduced to (see also Eq. (2.110))

$$\sigma_{\alpha}^{el} = \frac{\pi}{k_{\alpha}^2} |1 - S_{\alpha\alpha}^0|^2 \tag{4.14}$$

and

$$\sigma_{\alpha}^{in} = \frac{\pi}{k_{\alpha}^2} \sum_{\alpha < \beta} |S_{\alpha\beta}^0|^2 = \frac{\pi}{k_{\alpha}^2} \left(1 - |S_{\alpha\alpha}^0|^2 \right). \tag{4.15}$$

In the zero-energy limit, both cross sections have simple relations in terms of the complex scattering length components

$$\sigma_{\alpha}^{el} \longrightarrow 4\pi [(a_{\alpha}^{r})^{2} + (a_{\alpha}^{i})^{2}] \tag{4.16}$$

and

$$\sigma_{\alpha}^{in} \longrightarrow \frac{4\pi}{k_{\alpha}} a_{\alpha}^{i}.$$
 (4.17)

To illustrate the stability and convergence of the scattering lengths and also, to explore the dependence of the scattering length on the potentials (see for example Jamieson and Zygelman [77]), we present the real part of the scattering length as a function of collisional energy and reduced mass for the 1 ${}^2\Sigma^+$ and 2 ${}^2\Sigma^+$ states (see Fig. 4.11 and Fig. 4.12). In both cases, the scattering length reaches stable values for each reduced mass as the energy is reduced down to 10^{-13} eV. The variation of the scattering length with reduced mass is seen to be quite different for the two cases. According to Fig. 4.13 and Fig. 4.14, the scattering lengths for both states change from positive to negative with increase of the reduced mass. However, for the 1 ${}^2\Sigma^+$ state, the scattering length has singularities near reduced masses of 2 and 16.5 u, at ${\sim}7.5$ u for the 2 ${}^2\Sigma^+$ state.

The sign and the singularities of the scattering length are strongly related to the character of the potential. The sign depends on many factors including whether the potential is dominated by an attractive or repulsive interaction and whether bound states are supported [22]. Single-channel binding energies of bound vibrational states with J=0 for different reduced masses, which are shown in Fig. 4.15 and Fig. 4.16, indicate that zero-energy resonances exist at ~ 2 and ~ 16.5 u for the 1 $^2\Sigma^+$ state and at ~ 7.5 u for the 2 $^2\Sigma^+$ state. They are consistent with the reduced masses for which singularities are found in the scattering lengths. In the case of 23 Na- 4 He with reduced mass of 3.41 u, it is capable of producing one s-wave bound state near the 1 $^2\Sigma^+$ dissociation limit such that the sign of the scattering length is positive (37.3 a₀). On the other hand, it is impossible to support a bound state in the 2 $^2\Sigma^+$ potential for a reduced mass less than ~ 8 u. Therefore, the scattering length is negative for the 2 $^2\Sigma^+$ state of Na-He. The reason its value is close to zero (-0.686 a₀) is due to the strong repulsive interaction of 2 $^2\Sigma^+$ potential. The repulsive portion of the potential gives a positive contribution to the scattering length which reduces the negative contribution due to the bound-state-less attractive well. With decrease in reduced mass, which is

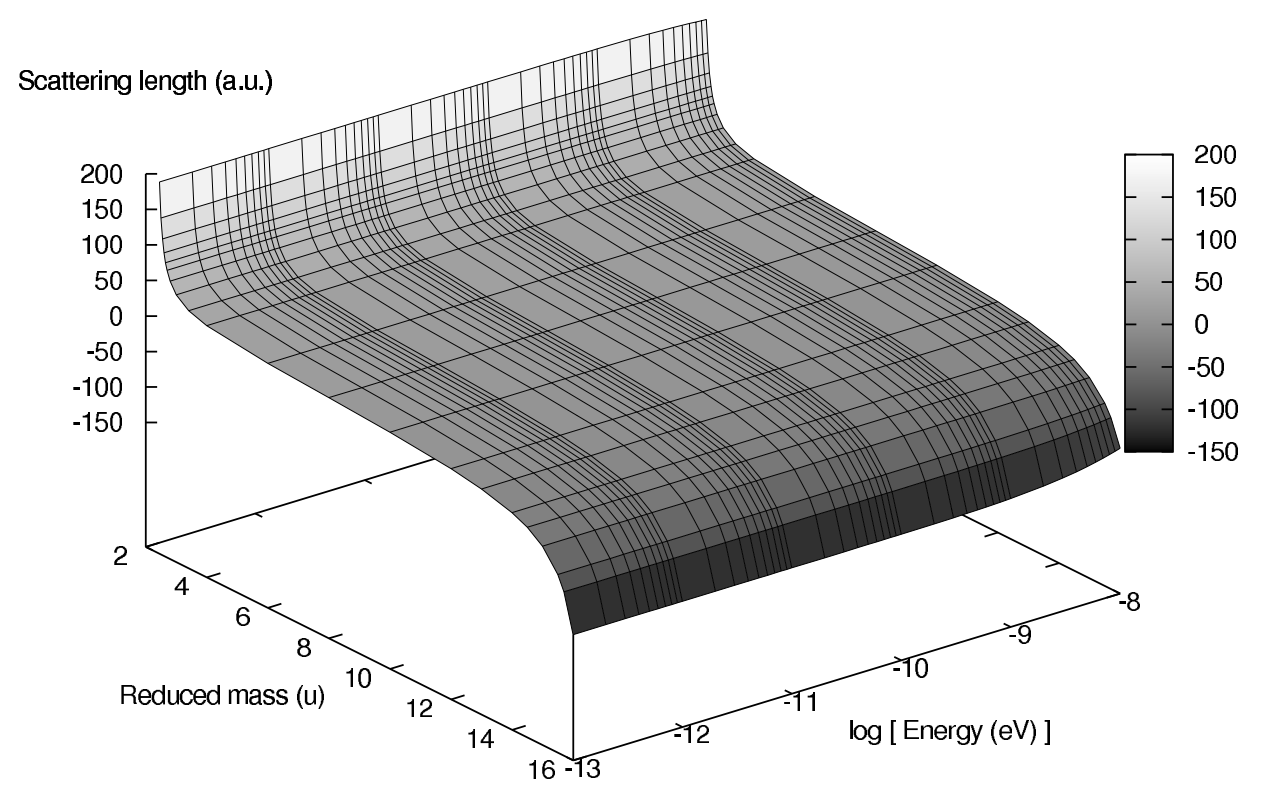


Figure 4.11: The Na-He scattering length as a function of reduced mass and collision energy for the 1 $^2\Sigma^+$ (J=0).

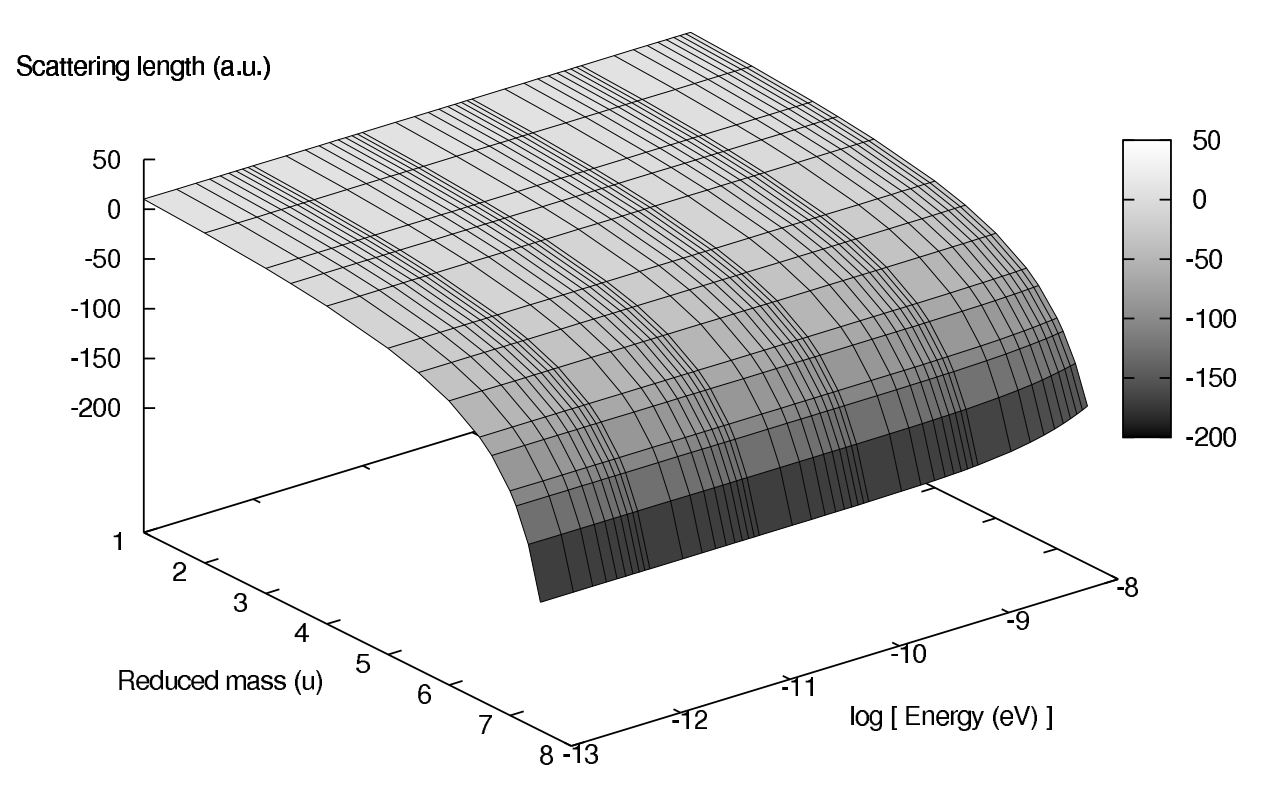


Figure 4.12: The Na-He scattering length as a function of reduced mass and collision energy for the 2 $^2\Sigma^+$ (J=0).

equivalent to reducing the depth of the van der Waals well since the effective potential is $2\mu V(R)/\hbar^2$, the scattering length becomes positive for the 2 $^2\Sigma^+$ state. It illustrates that repulsive interaction overcomes the attractive interaction to turn the scattering length from negative to positive values.

Finally, we comment that because of the large energy gap between the molecular states correlating to the Na(3s) and Na(3p) the imaginary part of the scattering length a^i for the $2^2\Sigma^+$ state is negligibly small. We defer presenting results of the $1^2\Pi$ scattering length to a future work because such a calculation will require inclusion of coupling of the fine structure terms correlating with the Na(3p), which may also have an influence on the $2^2\Sigma^+$ for energies less than $\sim 10^{-3}$ eV. The accumulation of the dependence of the scattering length on the potential and fine-structure-coupling effects suggest that the magnitude and sign of the $2^2\Sigma^+$ scattering length is uncertain. On the other hand, Fig. 4.13 illustrates that the positive value of the ground state scattering length is robust and that its magnitude is unlikely to varying by more than a factor of two. Therefore, ultracold collisions of ground state Na and He will be dominated by repulsive interactions.

4.5 ASTROPHYSICAL IMPLICATIONS

The Na D line is observed in absorption in a variety of astrophysical sources and in emission when sufficiently energetic electrons are available to populate the 3p levels. In the former case, the density in most objects, e.g. stellar atmospheres, is large enough to ensure that the electronic levels are in LTE.

While the indirect observation of atomic Na in the atmosphere of the transiting EGP HD 209458b was a ground-breaking achievement [50], the observed difference in the transit depth in and out of the region of the Na D line was only about half that expected from model predictions [78, 79, 80]. A number of possibilities to explain this discrepancy was suggested by Charbonneau *et al.* [50] and later expanded on by Fortney *et al.* [81]. They considered the following scenarios: depletion of Na into molecules and or condensates, subsolar metallicity

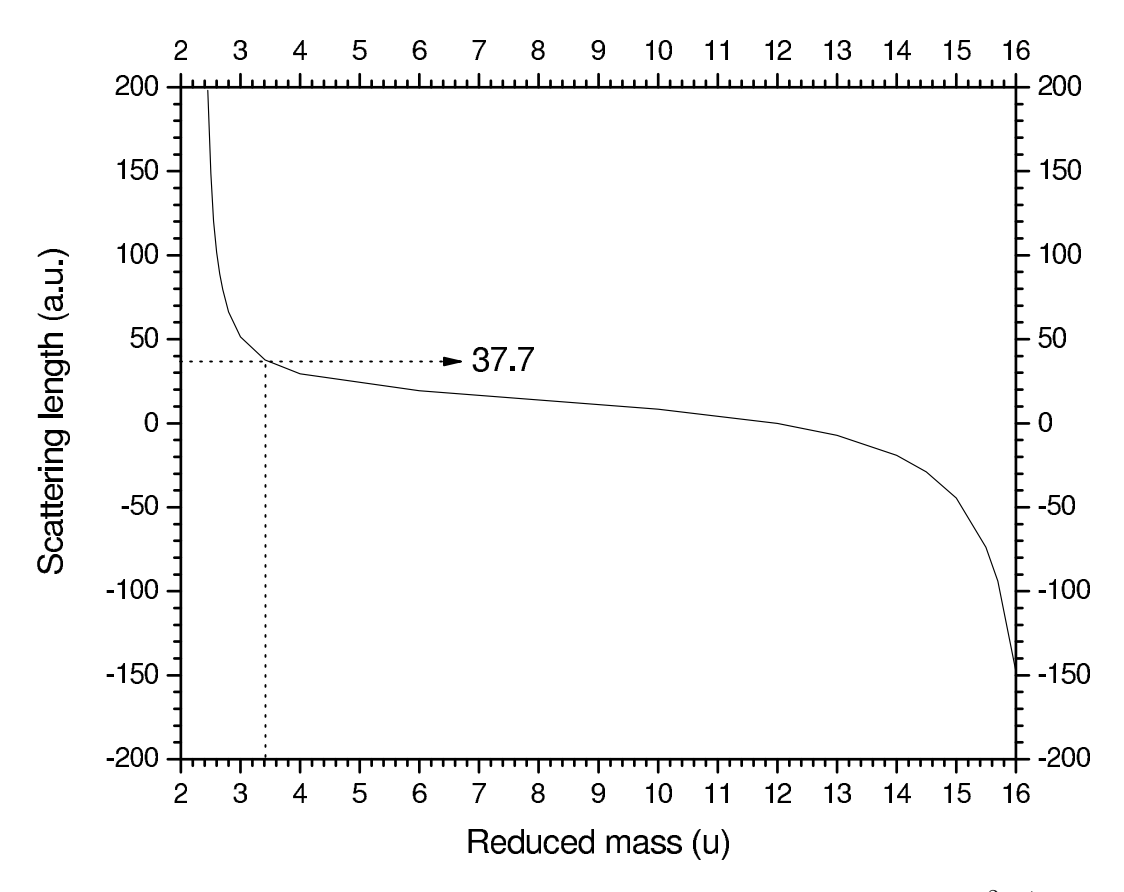


Figure 4.13: The variation of the Na-He scattering length for the 1 $^2\Sigma^+$ with reduced mass ($E=10^{-13}~{\rm eV}$). The dotted lines indicate the values of scattering length and reduced mass for the $^{23}{\rm Na}^{-4}{\rm He}$ system.

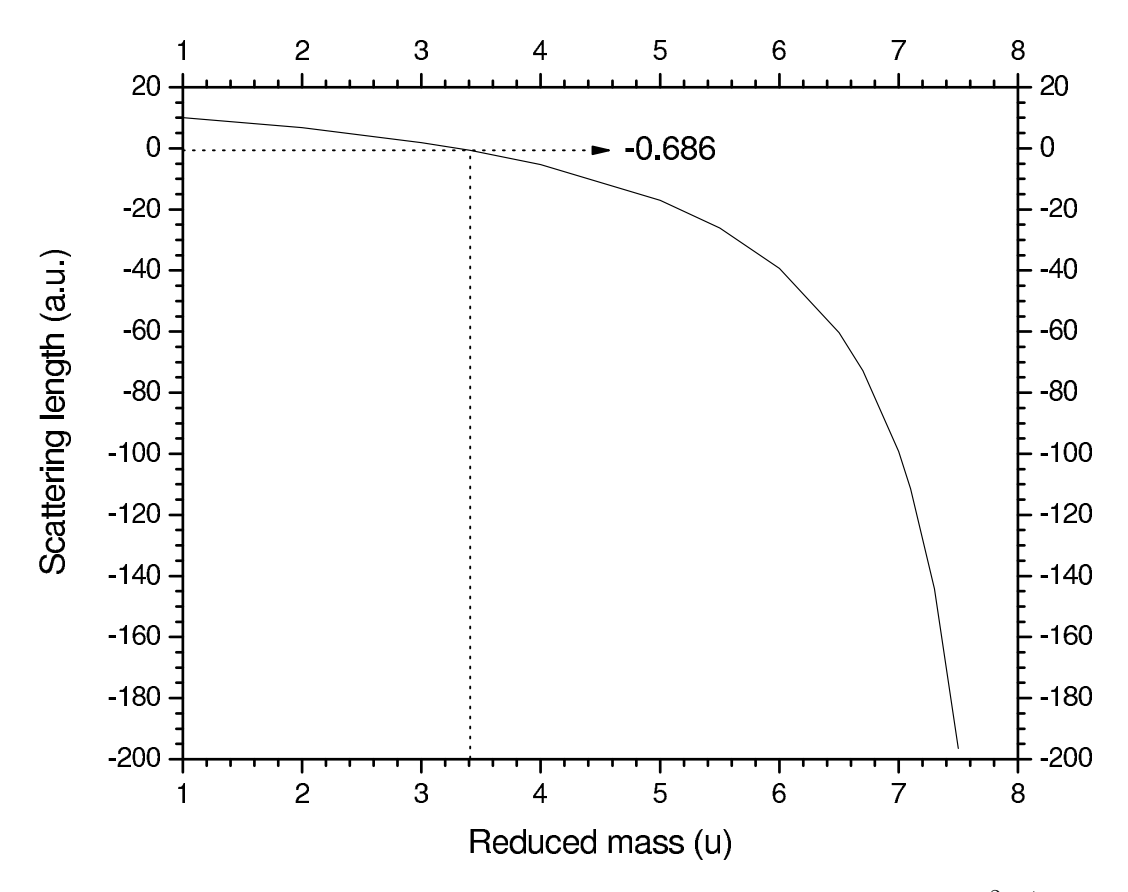


Figure 4.14: The variation of the Na-He scattering length for the 2 $^2\Sigma^+$ with reduced mass ($E=10^{-13}~{\rm eV}$). The dotted lines indicate the values of scattering length and reduced mass for the $^{23}{\rm Na}^{-4}{\rm He}$ system.

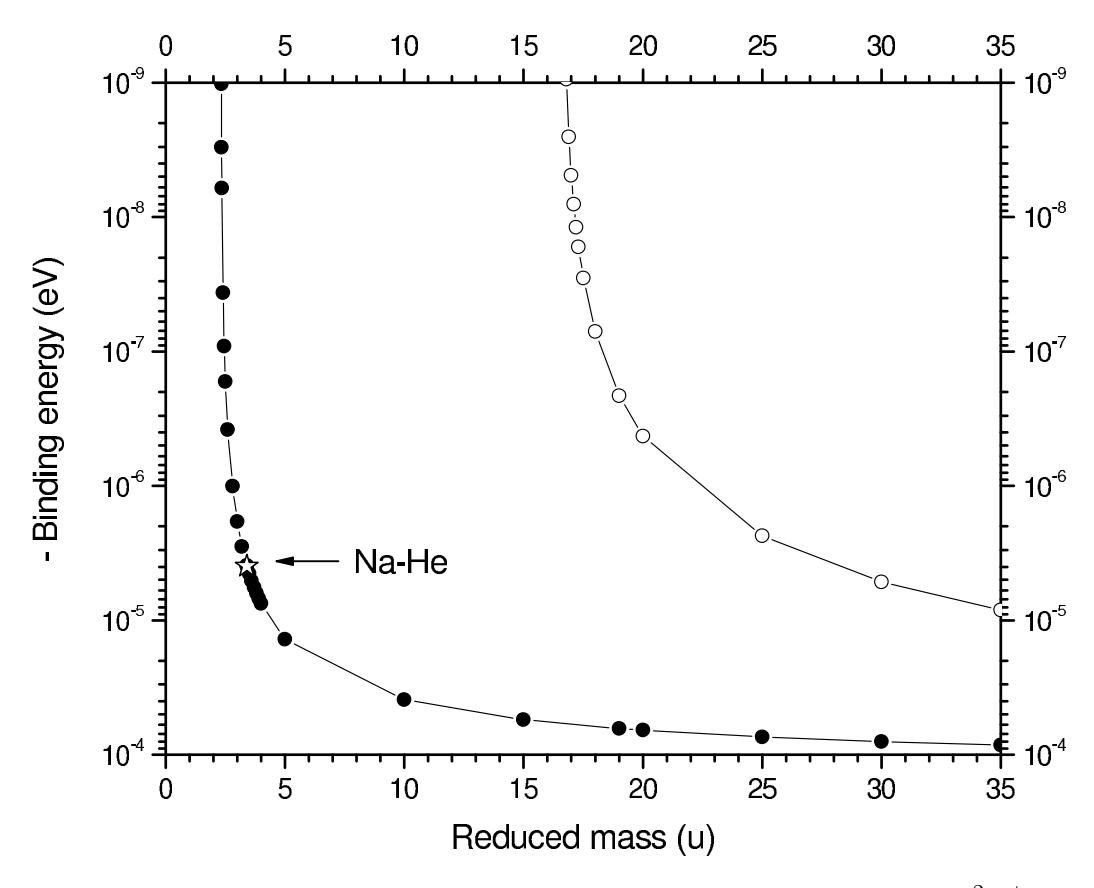


Figure 4.15: The variation of the Na-He binding energies for the 1 $^2\Sigma^+$ with reduced mass. The solid circle curve corresponds to bound states of v=0 and J=0. The open circle curve corresponds to bound states of v=1 and J=0. The star indicates the result for the 23 Na- 4 He reduced mass.

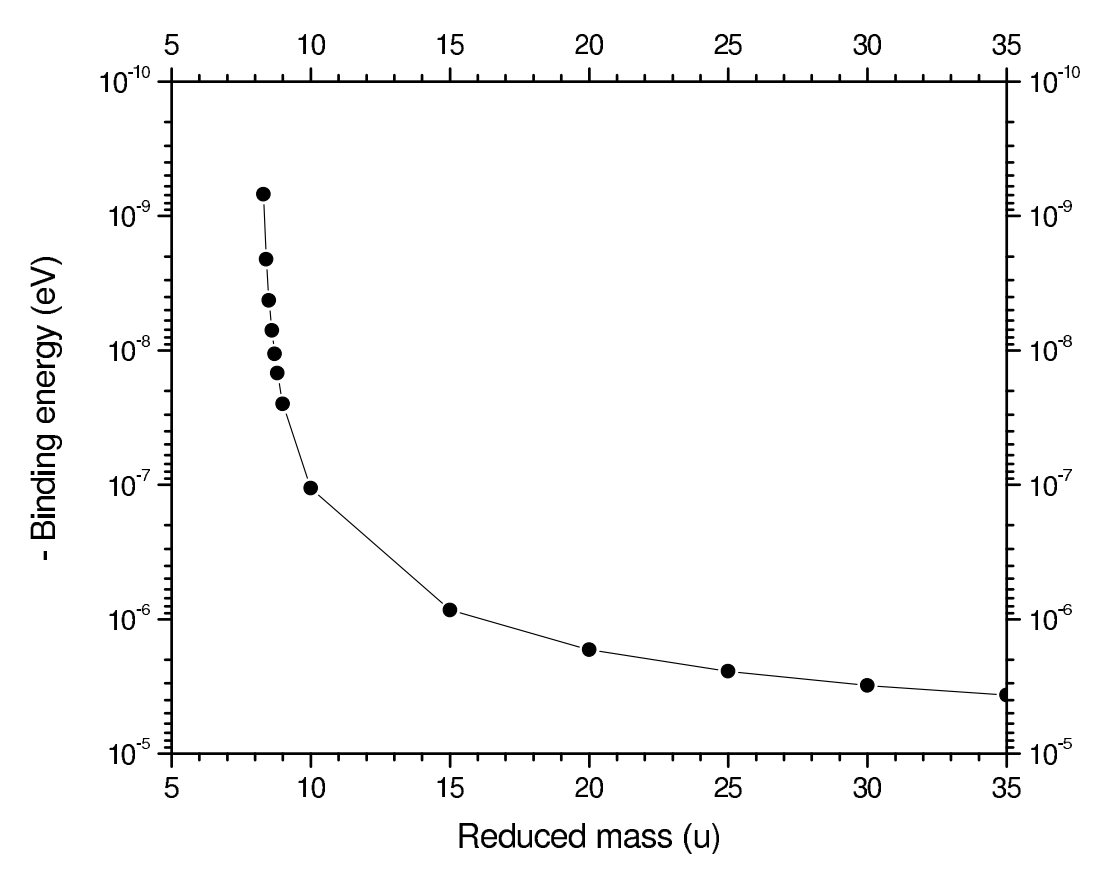


Figure 4.16: The variation of the Na-He binding energies for the 2 $^2\Sigma^+$ with different reduced mass for bound states of v=0 and J=0.

(though its companion star is of solar metallicity), NLTE Na photoionization due to the companion's ultraviolet (UV) flux, and cloud opacity. Using a parameterized description of the cloud's vertical distribution and base, Fortney et al. were able to reproduce the observations as cloud opacity tends to reduce the strength of line absorption features. However, the physics of cloud formation is still in its infancy and a complete, robust description requires a treatment of gravitational settling of the condensate grains which is not yet available.

Barman et al. [51] proposed another possibility for which, in principle, the physics is well known: Na is in NLTE. This explanation has a number of attractive features: exotic processes do not need to be imposed and Na (and other species) is likely to be in NLTE. This is the case due to the low effective temperature of the planet (\sim 1500 K), which results in low electron abundances (\sim 10⁻⁸), and the strong, non-Planckian UV radiation from the primary which is only 0.045 AU away. The lack of electrons means that the Na level populations can only be thermalized by collisions with H₂, He, or H which are expected to have smaller collisional cross sections. Unfortunately, the difficulty in performing NLTE calculations is the lack of collisional rate coefficients for the dominant atmospheric constituent H₂. In their model, Barman et al. [51] used electron excitation rate coefficients as a substitute for H₂ rate coefficients and found significant departures in the 3s and 3p level populations from LTE. This resulted in a reversal in the core of the Na D absorption lines which would appear as a reduced line depth in low resolution.

In the current work, we have obtained rate coefficients for collisional excitation and deexcitation of Na due to He as shown in Fig. 4.10. The rate coefficients are very small for temperatures less than 10^4 K and the process will therefore be very inefficient at thermalizing the Na level populations. In the inset to Fig. 4.10, the Na-He rate coefficients are compared to the same transitions for collisions due to H which were computed from the cross sections of Belyaev et al. [74]. Fit coefficients for Na-H collisions are given in Table 4.3. While the Na-H rate coefficients are 4-5 orders of magnitude larger, atomic hydrogen will mostly be tied-up in H_2 in an EGP, so that the relative efficiently of the Na-H to Na-He processes will

be significantly smaller than the ratio of the rate coefficients. The excitation rate coefficients for collisions due to H_2 are currently unknown, but their magnitude might be expected to be intermediate between the H and He perturber values. As the rate coefficients for all neutral perturbers are smaller than those due to electron impact, the significant departure from LTE obtained by Barman *et al.* would appear to be a robust result and a valid interpretation for a inferred reduced Na abundance in HD 209458b.

4.6 Summary

Elastic and inelastic collisions of Na(3s,3p) with He have been investigated using the quantum-mechanical CC approach. The major results include total cross sections, partial-wave cross sections, and rate coefficients for elastic scattering for processes (4.1) and (4.2); total cross sections, state-to-state cross sections, and rate coefficients for the quenching and excitation processes (4.3); and the scattering length as a function of reduced mass and collision energy for $1^{2}\Sigma^{+}$ and $2^{2}\Sigma^{+}$ states.

The comparison of our results to the theoretical prediction of Bottcher et~al. shows good agreement for the elastic cross sections of the 1 $^2\Sigma^+$ state. In the ultracold region, the elastic total cross sections of 1 $^2\Sigma^+$ and 2 $^2\Sigma^+$ states are determined solely by s-wave scattering. Through partial-wave analysis, the orbiting resonances due to quasi-bound states resulting in sharp peaks imposed upon total cross sections are illustrated. The quenching cross sections are dominated mostly by the de-excitation from 1 $^2\Pi$ to 1 $^2\Sigma^+$, while the excitation from the 1 $^2\Sigma^+$ to 2 $^2\Sigma^+$ has the main contribution for the excitation cross sections for energies larger than 2.8 eV. The comparison with results without the 1 $^2\Pi$ -1 $^2\Sigma^+$ rotational coupling illustrates that this coupling has significant influence on both elastic and inelastic cross sections and resonances. The scattering lengths are sensitive to the reduced mass. In other words, a change in the potential could cause dramatic variation of the scattering length which is primarily controlled by the location of a zero-energy resonance. The large positive value for the 1 $^2\Sigma^+$ state of the Na-He system reveals that there is a bound state supported

by the 1 $^2\Sigma^+$ potential, while the scattering length of small negative value close to zero for the 2 $^2\Sigma^+$ state manifests that, based on the lack of a bound state for the 2 $^2\Sigma^+$ potential, the attractive part of potential slightly overcomes the repulsive part of the potential.

Finally, the small rate coefficients obtained for inelastic collisions of Na with He strengthens the argument made by Barman *et al.* [51] that the sodium electronic level populations are out of equilibrium in the atmosphere of the extrasolar giant planet HD 209458b.

Chapter 5

VIBRATIONALLY-RESOLVED CHARGE TRANSFER FOR PROTON COLLISIONS WITH CO AND H COLLISIONS WITH CO⁺

In this chapter, ion-molecule collisions are illustrated by an application of a quantal MOCC method utilizing the IOSA [82] to electron capture processes for proton collisions with carbon monoxide, and reverse processes for collision energies between 0.5 and 1000 eV/u. The potential surfaces and couplings, computed with the MRD-CI method for a range of H⁺-CO orientation angles and C-O separations, are adopted in the scattering calculations. Results including vibrationally-resolved and orientation-angle-dependent cross sections are presented for a range of CO and CO⁺ vibrational levels. Comparison with experiment is made where possible and the relevance of the reaction in astrophysics and atmospheric physics is discussed.

5.1 Introduction

Electron capture processes are well known to be of great interest in many fields of study and are relevant to planetary atmospheres, the interstellar medium, and controlled-thermonuclear fusion. In particular, many investigations are focused on collisions of protons with atoms or molecules, since the major constituent of the solar wind are protons. For example, the interaction of the solar wind with the atmospheres of planets or comets plays a crucial role in understanding X-ray emission from these objects and the interface between the solar wind and their atmospheres. X-ray emission from charge exchange also has the potential to provide information on the composition of the atmospheres and the solar wind.

For the specific case of electron capture by protons in collisions with CO, numerous measurements have been carried out over the past five decades [44, 83, 84, 85, 86, 87], but the number of theoretical studies [88, 89, 90] are sparse. The effect of molecular orientation, the so-called steric effect, for proton-CO collisions was discussed in the theoretical work of Kimura et al. [88] and Kumar et al. [90]. In Kimura et al., a quantal MOCC calculation was performed which considered three orientation angles ($\gamma = 0^{\circ}, 90^{\circ}$, and 180°) of the target molecule. However, CO was held fixed at its equilibrium distance $r_{\rm e} = 2.1~a_0$ throughout the collision; the so-called "electronic approximation" (EA). Kumar et al. also performed a EA calculation, but with a time-dependent wave-packet propagation (TDWP) method. In a preliminary investigation [89], Stancil relaxed this restriction and considered vibrational motion of CO. This allowed for the computation of vibrationally-resolved cross sections within the IOSA [15, 16, 17], which has been discussed in Section 2.6, and demonstrates that an EA calculation is inappropriate for collision energies less than $\sim 100~{\rm eV/u}$.

Extending the earlier investigation [89], the present work includes a significant enhancement in the CO and CO⁺ vibrational bases in order to provide more accurate and more extensive information on vibrationally-resolved electron capture. The collision process considered in this work is

$$H^{+} + CO(X^{1}\Sigma^{+}, \nu) \leftrightarrow H + CO^{+}(X^{2}\Sigma^{+}, \nu'),$$
 (5.1)

which is endoergic by 0.416 eV for $\nu = \nu' = 0$ in the forward direction.

The theoretical approach for the scattering calculation was given in Chapter 2 and particularly, in Section 2.6 for IOSA. The potentials and couplings in the adiabatic and diabatic representation for three collision configurations are discussed in Section 5.2. The results of state-to-state, state-selective, and angle-averaged total cross sections are illustrated in Section 5.3 including the discussion and comparison with the existing experimental data and previous calculations. Section 5.4 addresses the implications to astrophysics and atmospheric physics from the current results, while Section 5.5 briefly gives the summary of the present investigations.

5.2 Electronic Structure Calculations

Ab initio calculations were performed for the potential surfaces and coupling matrix elements of the HCO⁺ molecular ion. The calculations were carried out using the MRD-CI method [35, 36, 37, 62, 63] with the cc-pVTZ basis for H, C, and O atoms of Dunning [65]. In this work we consider three collision configurations defined in Fig. 5.1 with $\gamma = 0^{\circ}$, 90°, and 180°. For each γ , the adiabatic potentials and couplings as functions of the H-CO internuclear distance R are computed with five different fixed C-O internuclear separations of r=1.7, 1.9, 2.1, 2.3, and 2.5 a_0 , where 2.1 a_0 is the equilibrium distance of the CO molecule. For the collision energies computed in this work, we consider the two lowest electronic states only, as the remaining excited states are more than 2.5 eV higher in energy and therefore of secondary importance in the collision dynamics. The two lowest potentials, with CO at its equilibrium geometry $r = r_{\rm e}$, are shown in Fig. 5.2 and correspond to the asymptotes $\mathrm{H^+} + \mathrm{CO}(X^{-1}\Sigma^+)$ and $\mathrm{H} + \mathrm{CO}^+(X^{-2}\Sigma^+)$. For $\gamma = 0^\circ$ and 180° , the $X^{-1}\Sigma^+$ and $2^{-1}\Sigma^+$ states were computed in the C_{2v} subgroup of the $C_{\infty v}$ point group, while for $\gamma = 90^{\circ}$, the 1 $^1A'$ and $2^{1}A'$ were calculated in the C_s point group [88]. The adiabatic potentials of these two states as functions of R and various r are shown in Figs. 5.3, 5.4, and 5.5 for different orientation angles. The nuclear radial coupling matrix elements, which connect these two states, are displayed as functions of R and various r in Figs. 5.6, 5.7, and 5.8 for three different collision geometries.

For convenience in the scattering calculations, we make a unitary transformation from the adiabatic picture to a diabatic representation (see Section 2.3) for the electronic potentials and couplings. The resulting diagonal terms of the electronic diabatic potentials are adjusted to match the experimental asymptotic energies for $\nu = \nu' = 0$. The vibronic diabatic potential energies are then obtained by shifting the appropriate electronic energy by the vibrational excitation energies as shown in Figs. 5.9, 5.10, and 5.11 (see Eq. (2.122)). The vibronic diabatic couplings are obtained by averaging the electronic diabatic couplings over the vibrational wave functions. The dominant vibronic couplings are shown in Figs. 5.12,

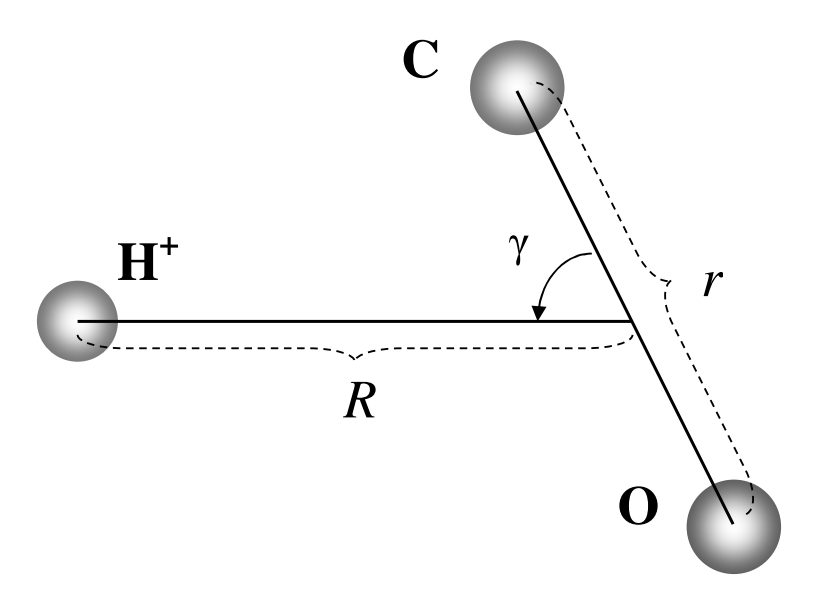


Figure 5.1: Collisions of H⁺ with CO defined in Jacobi coordinates.

5.13, and 5.14 for transitions connecting the states ν with $\nu' = \nu$, and $\nu \pm 1$. The vibronic couplings for larger $|\Delta\nu|$ are significantly smaller. The CO⁺ and CO ground state potentials, used to generate the vibrational wave functions, where taken from Krupenie and Weissman [91] and Borges *et al.* [92], respectively.

5.3 RESULTS AND DISCUSSION

The charge exchange cross sections for collisions of H⁺ with CO and H with CO⁺ were calculated for three orientations, i.e. $\gamma = 0^{\circ}$, 90°, and 180°, of the molecular target and included eleven and nine vibrational channels for CO and CO⁺, respectively. Examples of vibrationally-resolved state-to-state cross sections for H⁺-CO collisions for $\nu = 0 \rightarrow \nu' = 0 - 5$ are illustrated in Fig. 5.15. The difference in the cross sections among three angles becomes more conspicuous with increasing final vibrational excitation. For $\nu' \geq 2$, the angle-averaged results are primarily determined by the behavior of the $\gamma = 0^{\circ}$ cross sections. In Fig. 5.16, angle-averaged state-to-state cross sections for $\nu = 0$ are given as a function of

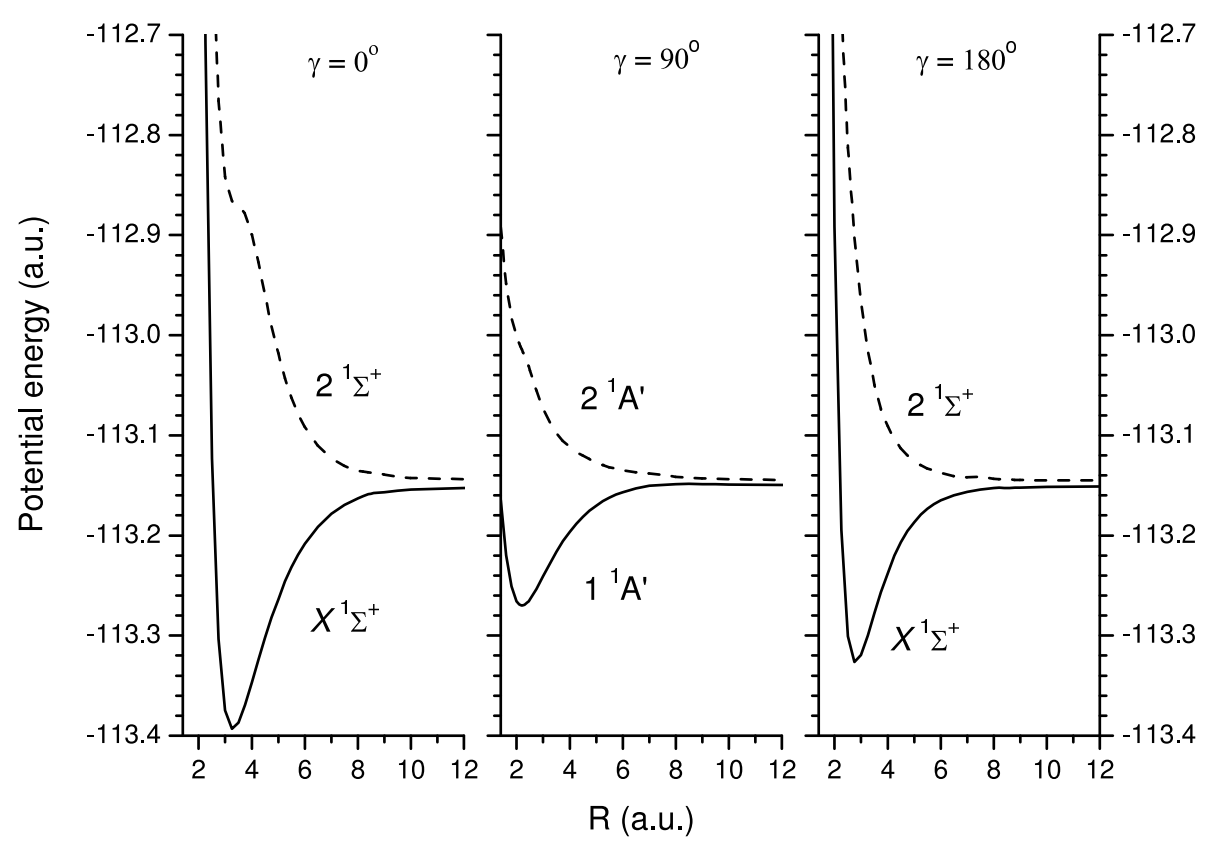


Figure 5.2: Adiabatic potential curves of H-CO⁺ as functions of R with $r=r_{\rm e}.$

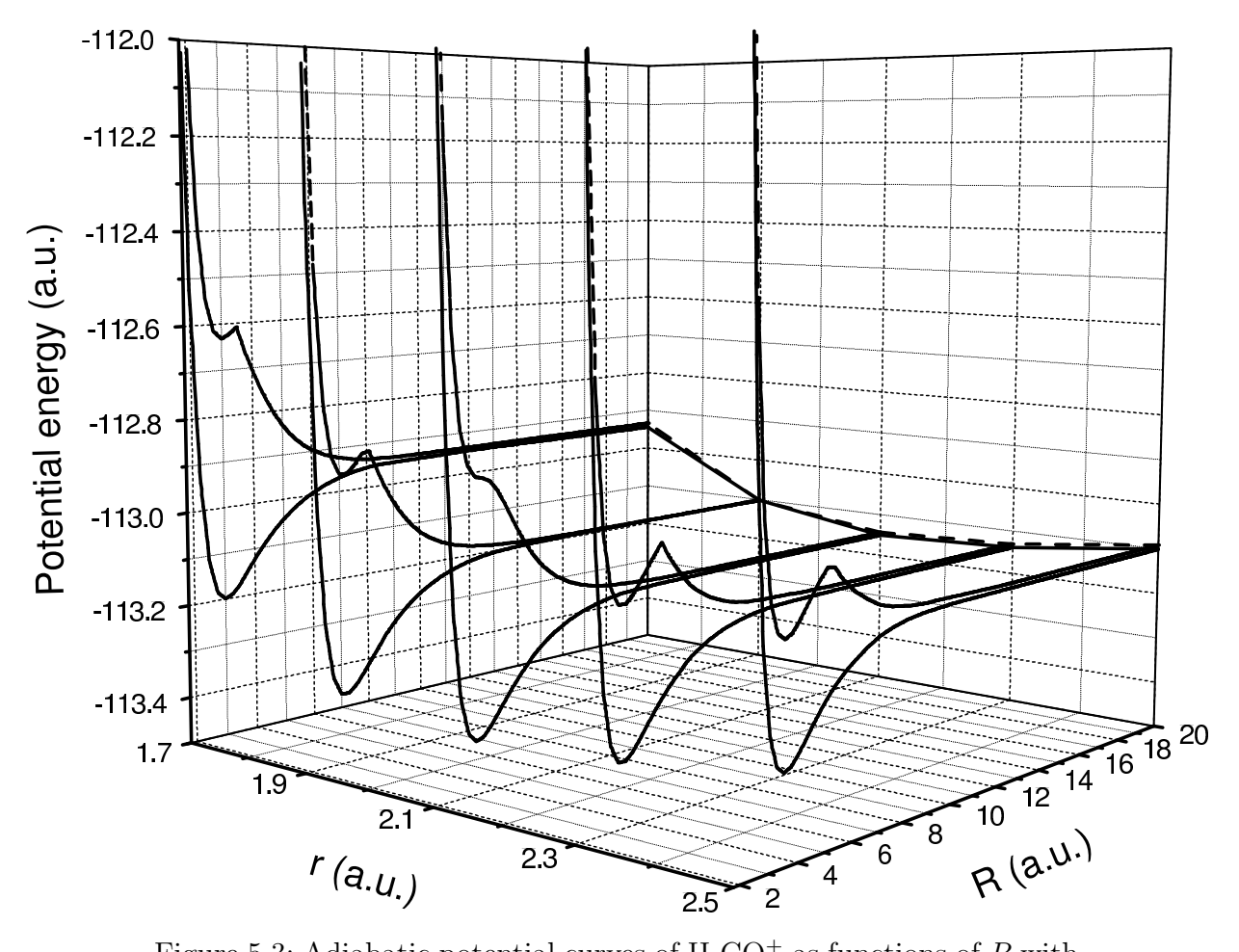


Figure 5.3: Adiabatic potential curves of H-CO⁺ as functions of R with $r=1.7,\ 1.9,\ 2.1,\ 2.3,\ {\rm and}\ 2.5\ a_0$ for $\gamma=0^{\circ}$.

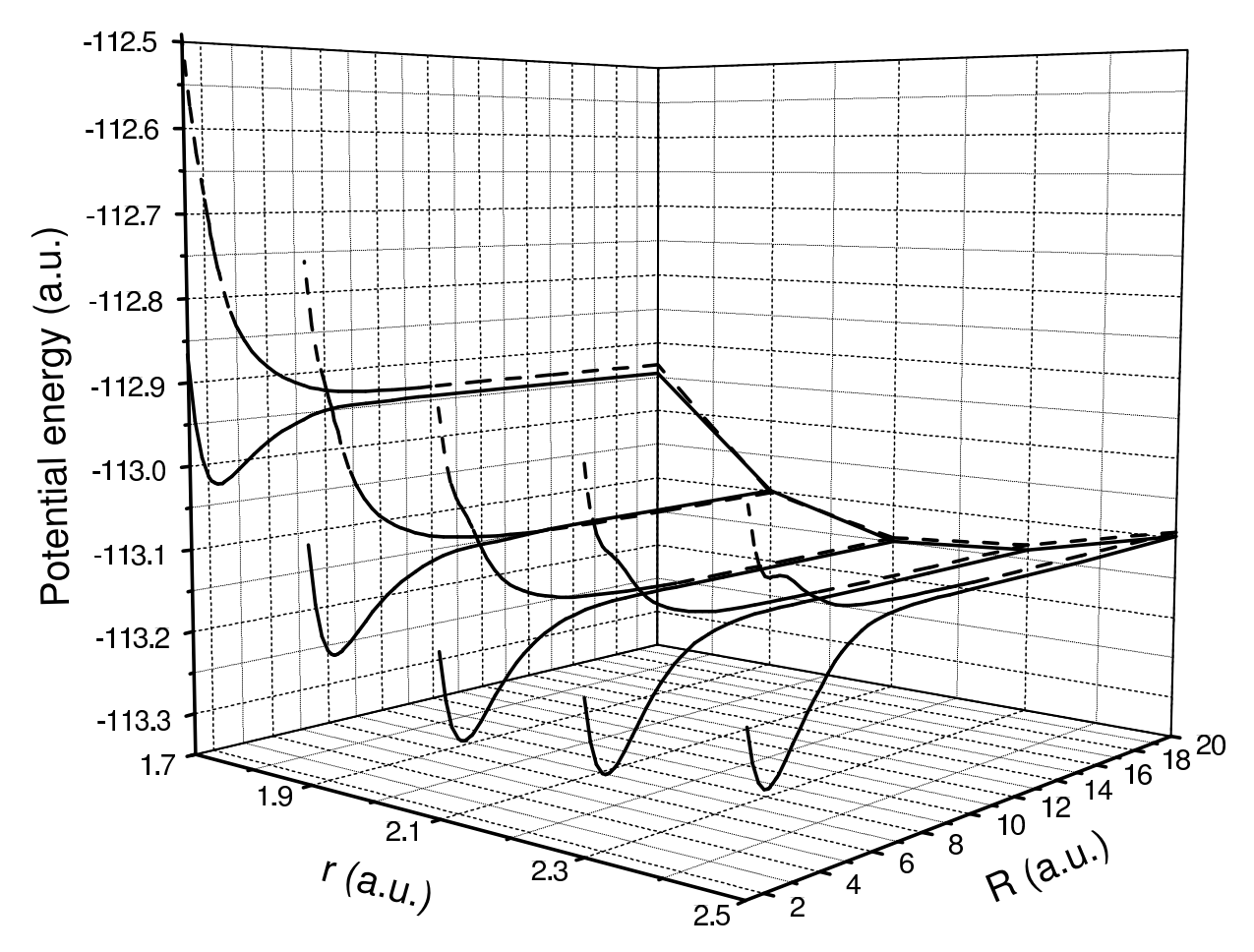


Figure 5.4: Adiabatic potential curves of H-CO⁺ as functions of R with $r=1.7,\ 1.9,\ 2.1,\ 2.3,\ {\rm and}\ 2.5\ a_0$ for $\gamma=90^\circ.$

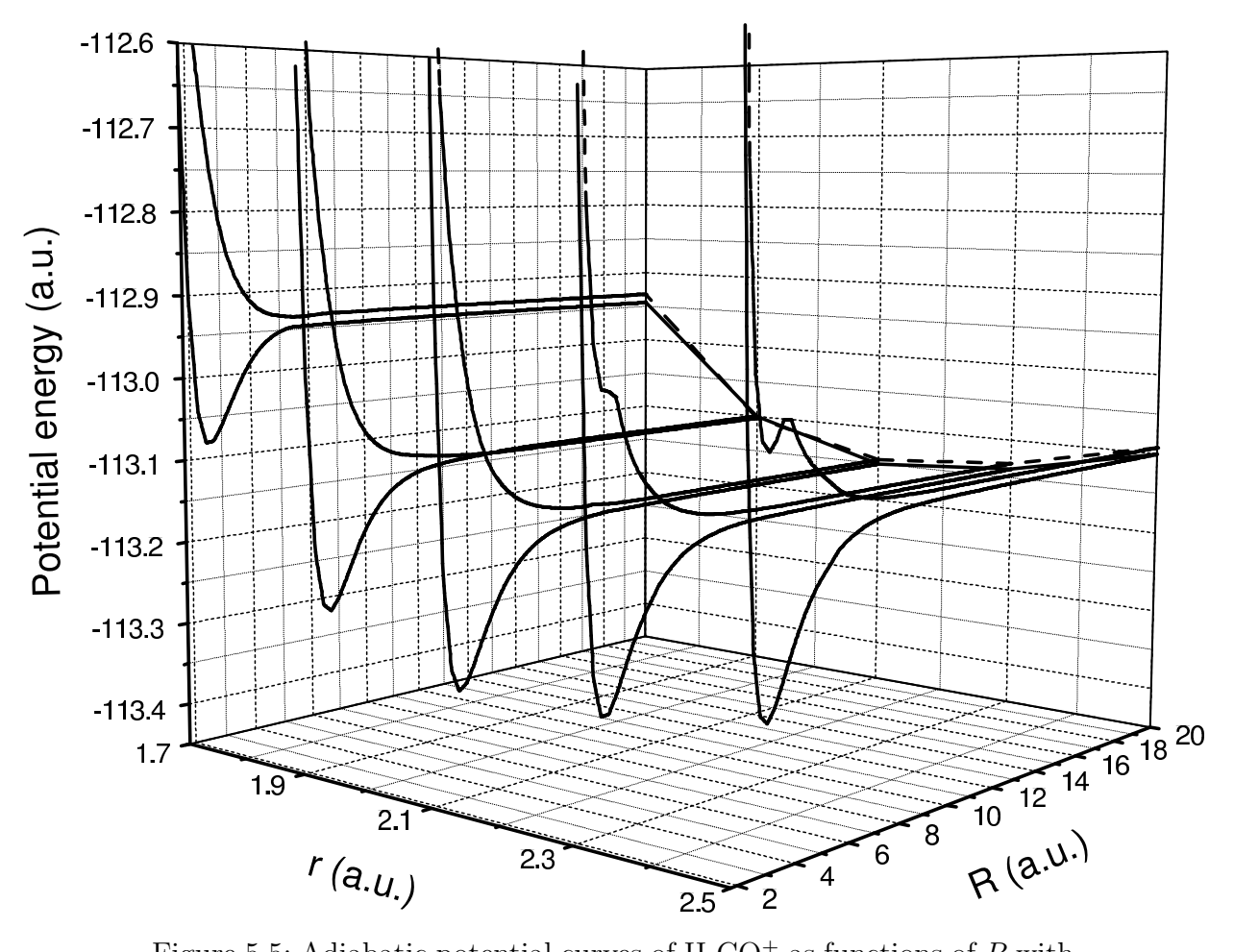


Figure 5.5: Adiabatic potential curves of H-CO⁺ as functions of R with $r=1.7,\,1.9,\,2.1,\,2.3,\,$ and $2.5\,\,a_0$ for $\gamma=180^\circ.$

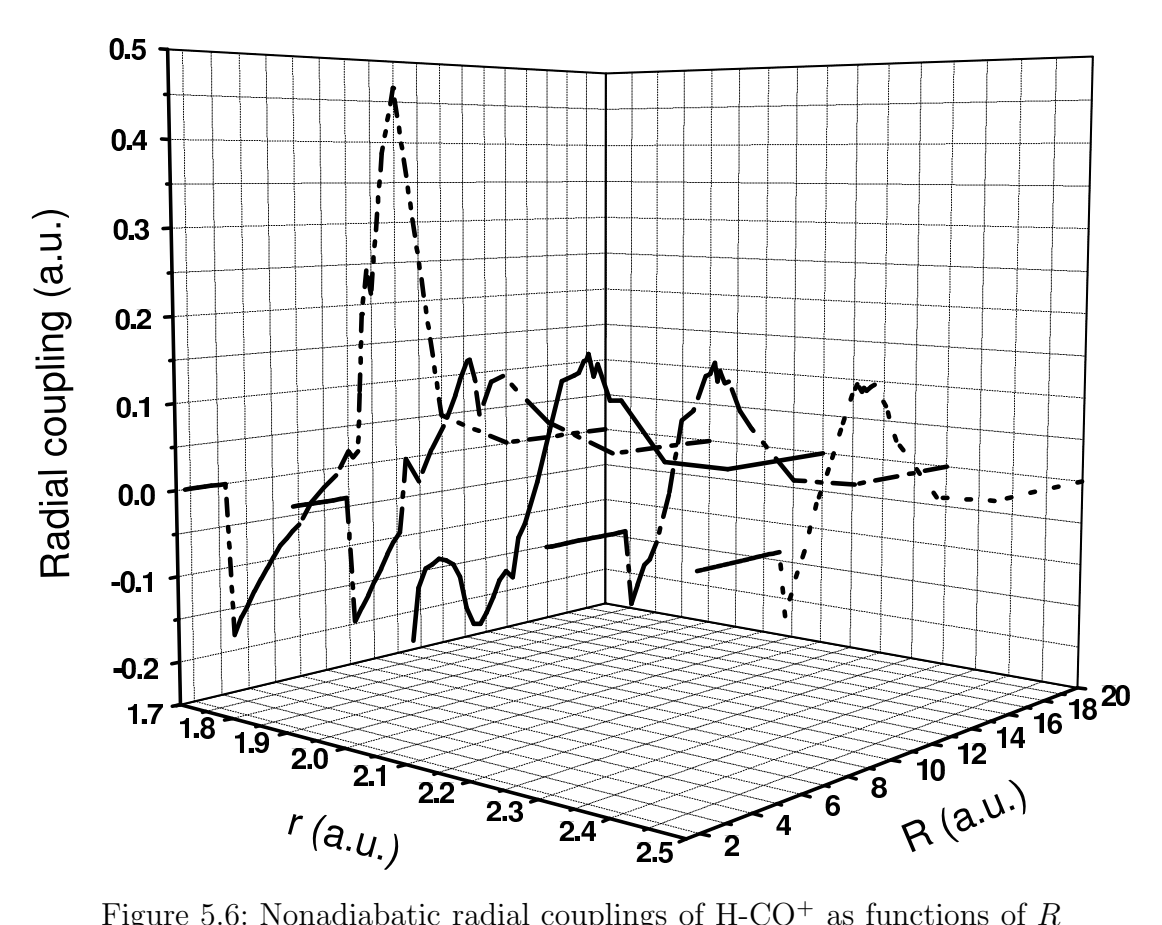


Figure 5.6: Nonadiabatic radial couplings of H-CO⁺ as functions of R with $r=1.7,\,1.9,\,2.1,\,2.3,\,$ and 2.5 a_0 for $\gamma=0^{\circ}.$

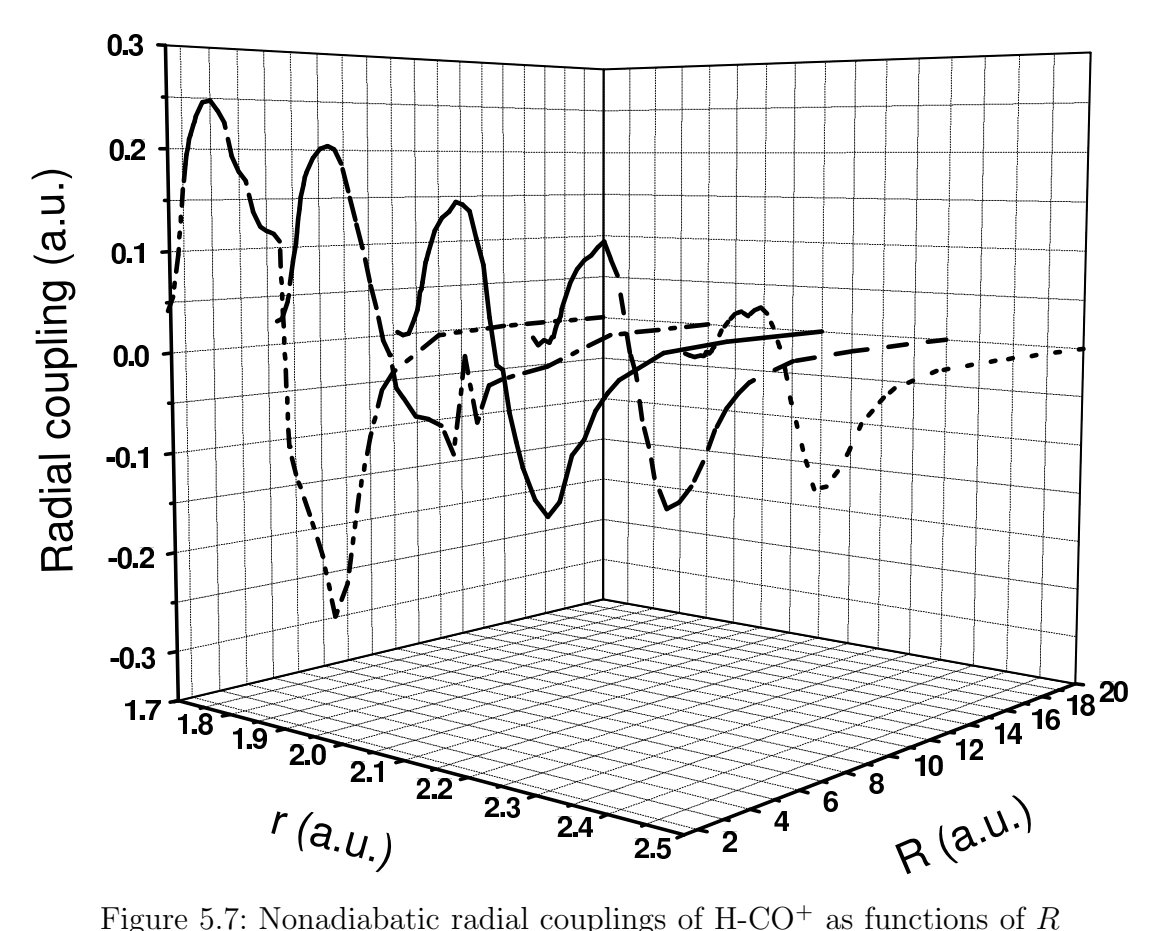


Figure 5.7: Nonadiabatic radial couplings of H-CO⁺ as functions of R with r = 1.7, 1.9, 2.1, 2.3, and $2.5 a_0$ for $\gamma = 90^{\circ}$.

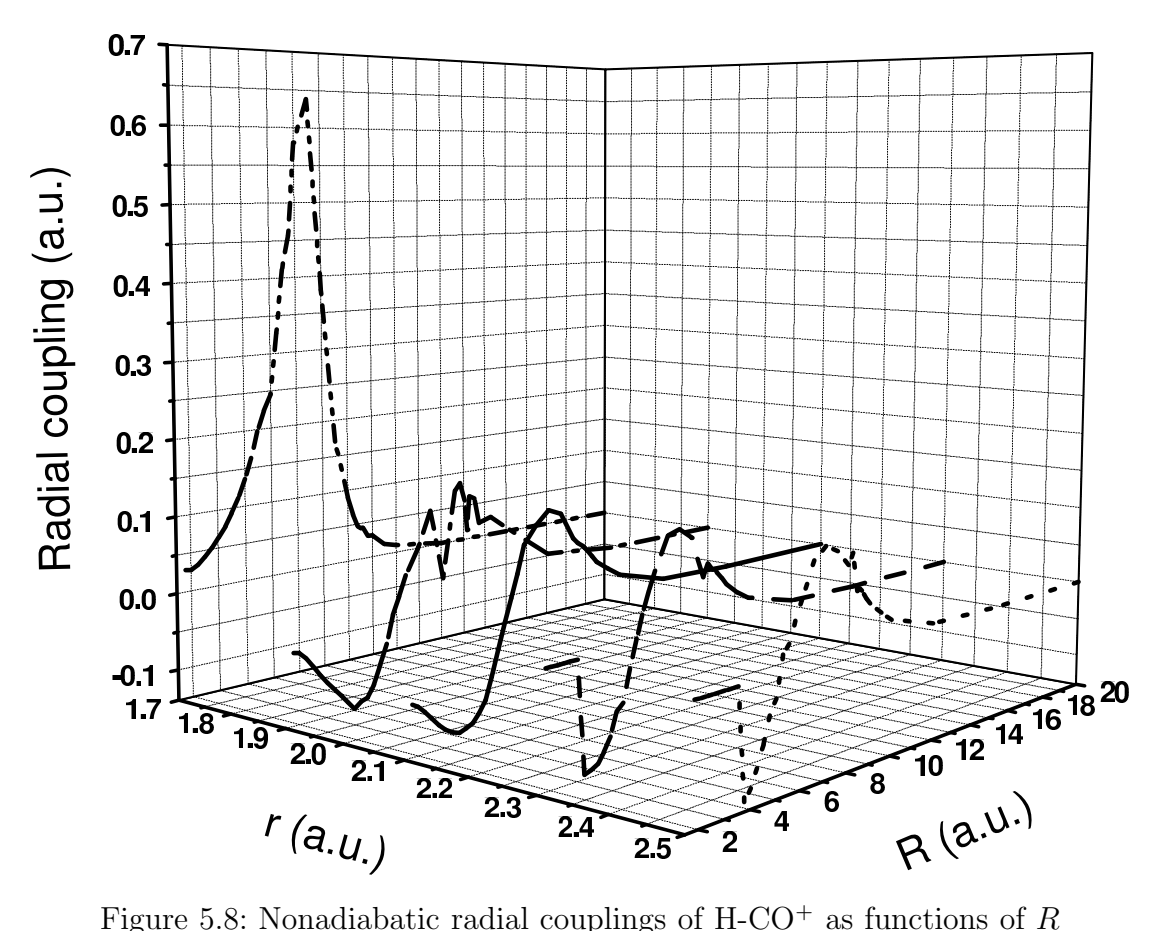


Figure 5.8: Nonadiabatic radial couplings of H-CO⁺ as functions of R with $r=1.7,\,1.9,\,2.1,\,2.3,\,$ and $2.5\,\,a_0$ for $\gamma=180^\circ.$

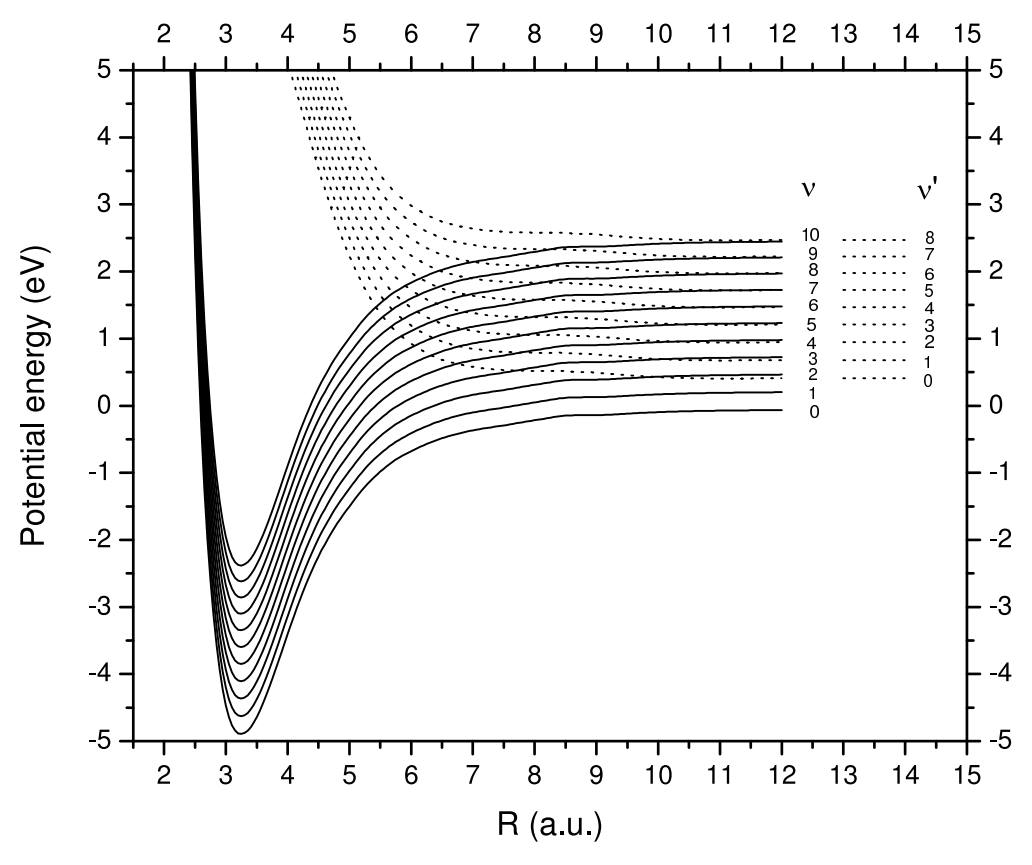


Figure 5.9: Diabatic potentials of H-CO⁺ as functions of R for the vibronic states of $\nu=0-10$ shifted from X $^1\Sigma^+$ and $\nu'=0-8$ from 2 $^1\Sigma^+$ at $\gamma=0^\circ$ with $r=r_{\rm e}$.

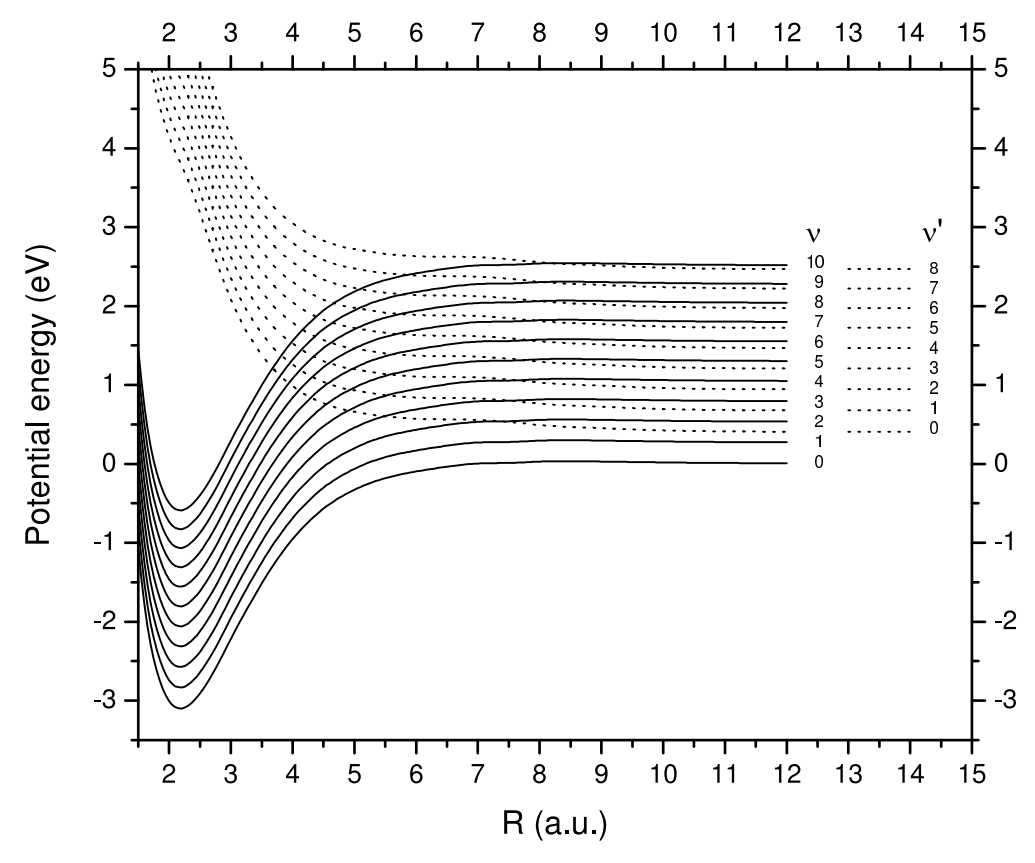


Figure 5.10: Diabatic potentials of H-CO⁺ as functions of R for the vibronic states of $\nu=0-10$ shifted from 1 $^1A'$ and $\nu'=0-8$ from 2 $^1A'$ at $\gamma=90^\circ$ with $r=r_{\rm e}$.

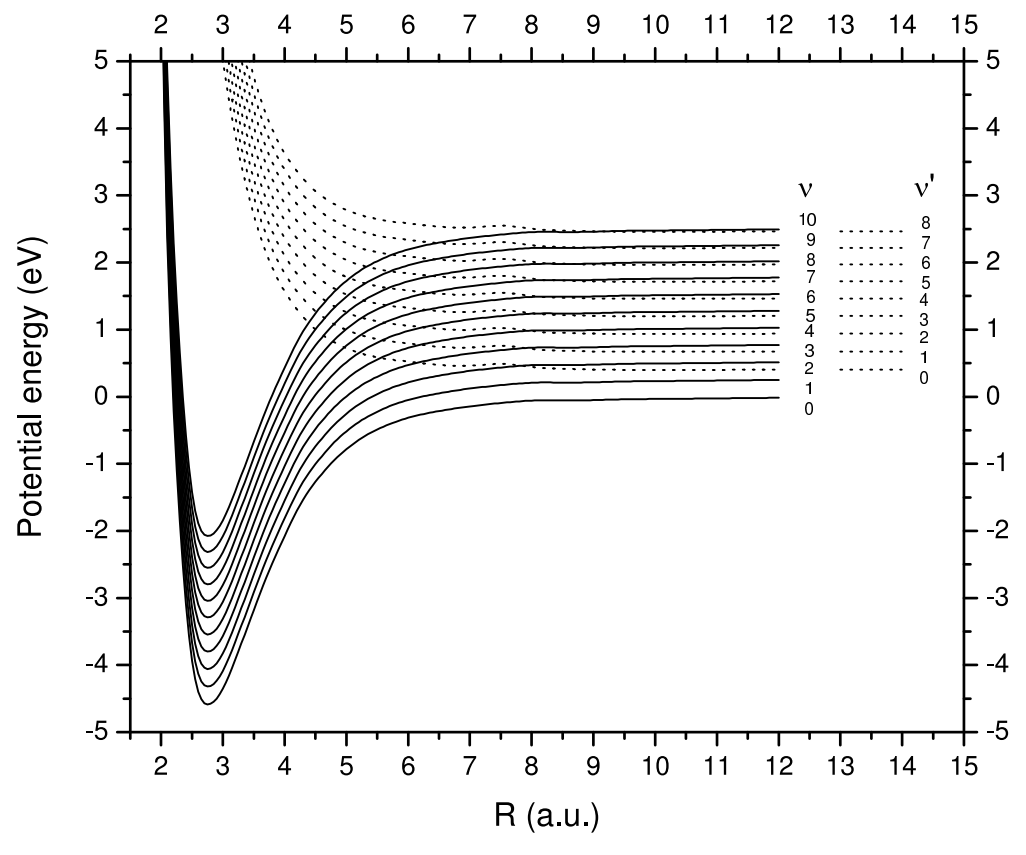


Figure 5.11: Diabatic potentials of H-CO⁺ as functions of R for the vibronic states of $\nu=0-10$ shifted from X $^1\Sigma^+$ and $\nu'=0-8$ from 2 $^1\Sigma^+$ at $\gamma=180^\circ$ with $r=r_{\rm e}$.

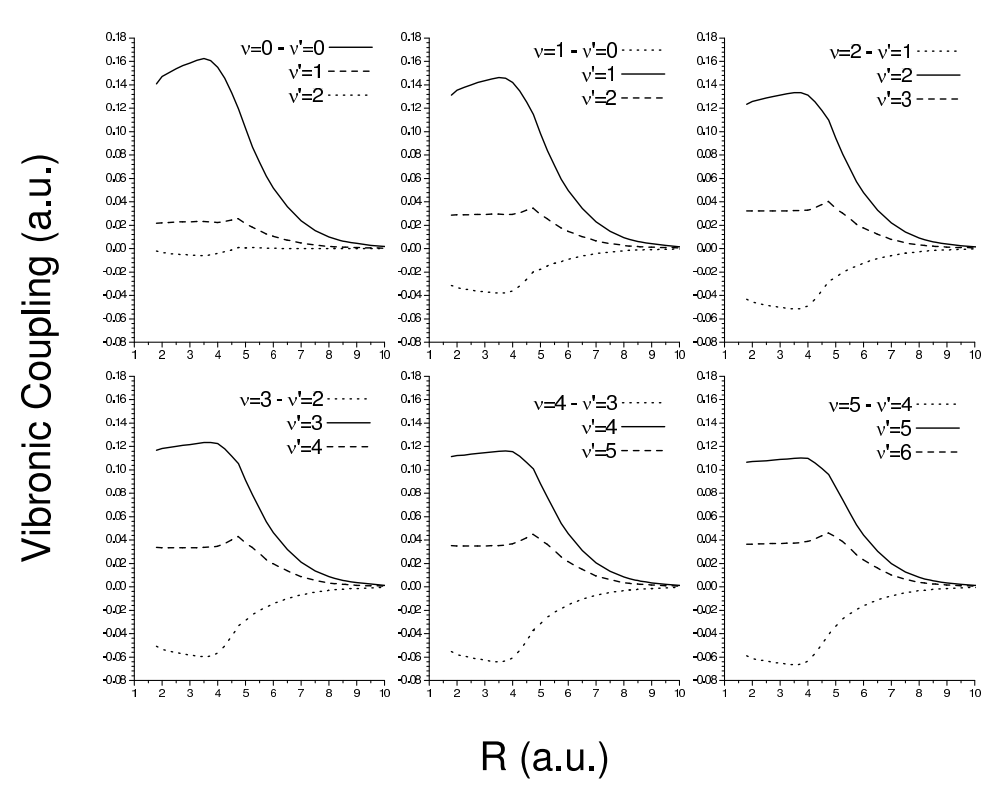


Figure 5.12: Vibronic couplings of H-CO⁺ for $\gamma=0^{\circ}$ as functions of R connecting states $\nu=0-5$ with states $\nu'=\nu$ and $\nu\pm1$.

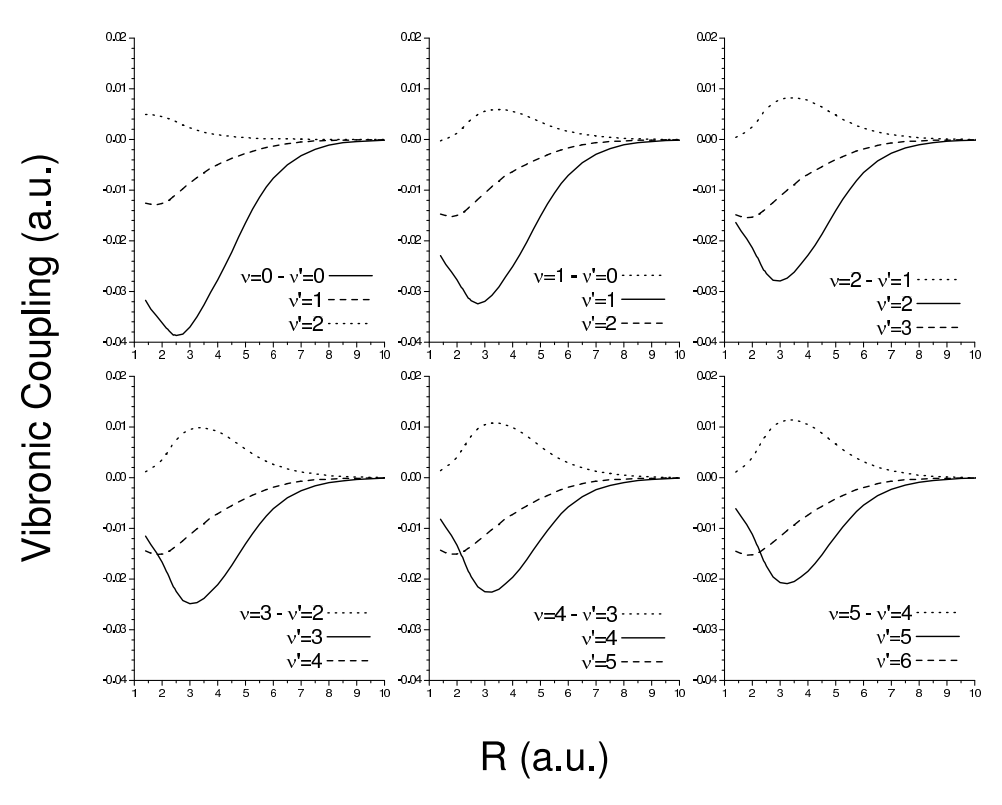


Figure 5.13: Vibronic couplings of H-CO⁺ for $\gamma = 90^{\circ}$ as functions of R connecting states $\nu = 0 - 5$ with states $\nu' = \nu$ and $\nu \pm 1$.

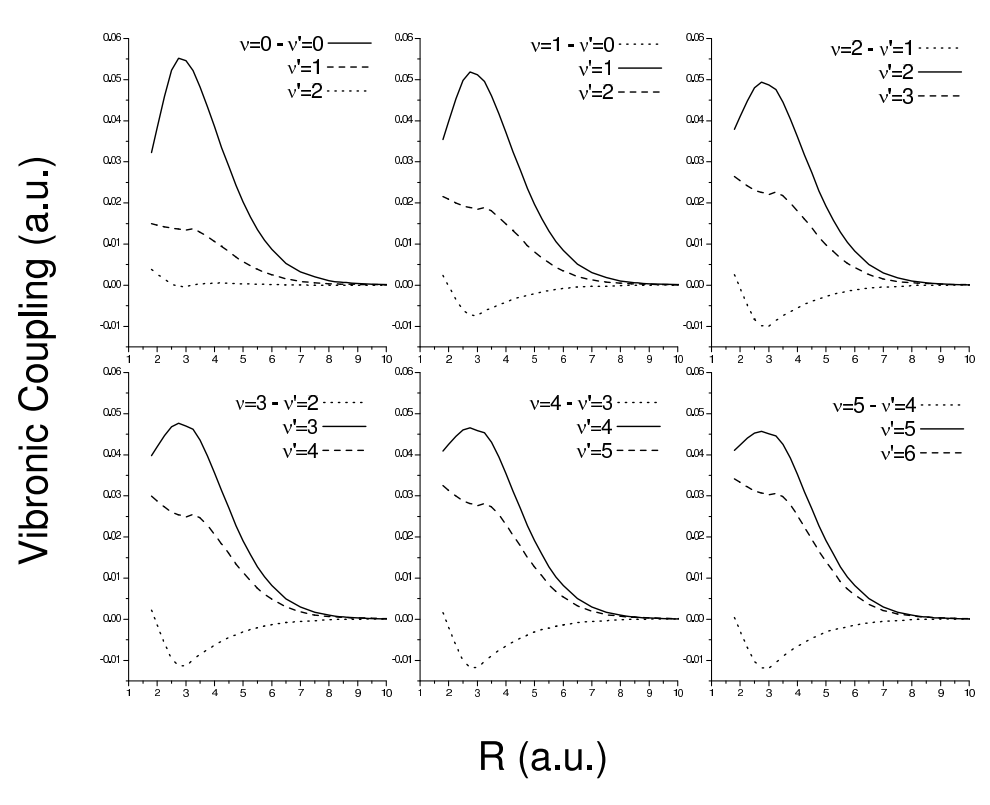


Figure 5.14: Vibronic couplings of H-CO⁺ for $\gamma = 180^{\circ}$ as functions of R connecting states $\nu = 0 - 5$ with states $\nu' = \nu$ and $\nu \pm 1$.

 ν' for two collision energies. The $\Delta\nu=0$ transition is shown to be the dominant process which is a consequence of the dominance of the corresponding vibronic coupling. Further, since the vibronic couplings diminish with increasing ν' , the cross sections tend to decrease as well. This behavior is directly related to the overlap of the initial CO and final CO⁺ vibrational wave functions which is nearly diagonal since the equilibrium separations of the two molecules are very similar. This suggests that to a rough approximation, the so-called centroid approximation (CA) where a purely electronic cross section is multiplied by Franck-Condon-like ionization factors, is valid for this collision system for collision energies above $\sim 100 \text{ eV/u}$.

State-to-state cross sections for H⁺-CO collisions with three orientation angles and $\nu > 0$ are shown in Figs. 5.17-5.19. In the high energy regime, the transition from the initial vibronic state ν to a final vibronic state $\nu' = \nu$ is the most dominant process, while in the low energy limit, i.e. near the threshold, the most significant process is a transition to a final vibronic state which is the nearest state in the asymptotic limit. Referring to the vibronic couplings in Figs. 5.12-5.14, it is obviously illustrated that the most important coupling connects two vibronic states of $\nu = \nu'$. However, since the couplings are largest at short R and the final vibronic potentials are repulsive (see Figs. 5.9-5.11), the peaks in the couplings are only sampled for relatively large collisions energies. For example, in Fig. 5.18(a) the cross section for $\nu = 1 \rightarrow \nu' = 1$ increases with collision energy to become the dominant channel above 10 eV/u. For smaller collision energies, capture to $\nu'=0$ is the primary channel due to a smaller energy gap. For $\nu = 2$, similar trends are seen in Fig. 5.18(b) with the largest cross section to $\nu'=2$ for energies larger than ~ 10 eV/u and to $\nu'=1$ for smaller energies. Capture to $\nu'=0$ is also seen to be significant at low energies and will likely become the dominant channel for energies below the $\nu'=1$ threshold since it is the only exoergic channel. Analogous behavior is seen for other initial $CO(\nu)$ states. Angle-averaged state-to-state cross sections of H⁺-CO collisions are shown in Figs. 5.20(a)-(d), which are dominated by collisions at $\gamma = 0^{\circ}$ for the same reasons as discussed in Fig. 5.15. The behavior of the different ν and ν' channels are the same as presented above.

The initial state-selective cross sections ($\nu=0-10$), given by Eq. (2.124), for $\gamma=0^\circ$, 90°, and 180° collisions of H⁺ with CO are displayed respectively in Figs. 5.21, 5.22, and 5.23. According to the state-to-state cross sections, the convergence of initial state-selective cross sections with respect to the present final states included is reliable except for $\nu=8$, 9, and 10, for which more vibronic states are likely needed. For low energies, the initial state-selective cross sections increase with increasing ν . Because all final states are endoergic for $\nu=0$ and 1 (see Figs. 5.9-5.11), the cross sections are expected to drop sharply due to the threshold. For $\nu>1$, exoergic channels become available which result in the rise of cross sections. For the higher energy region, i.e. energies larger than ~70 eV/u for the case of $\gamma=90^\circ$, the cross sections increase with decreasing ν . For $\gamma=0^\circ$ and 180° and energies larger than ~30 eV/u, the initial state-selective cross sections approach values of similar magnitude. The angle-averaged initial state-selective cross sections are shown in Fig. 5.24, which except for $\nu=9$ and 10, are weakly dependent on ν for energies greater than 50 eV/u.

Figs. 5.25-5.30 are similar to Fig. 5.16 and Figs 5.21-5.24, except for the reverse process of H collisions with CO⁺(ν'). Fig. 5.25 shows angle-averaged state-to-state cross sections which have behaviors similar to H⁺-CO, except that exoergic channels are available for all initial states. As discussed previously, $\nu' = \nu$ transitions eventually become the most important as long as the collision energy is large enough. A comparison of final CO vibrational cross sections at relatively high (\sim 1 keV/u) and low (\sim 10 eV/u) collision energy is presented in Fig. 5.26. Generally, a CA-type trend is evident except at low energy where the capture to ν =0 and 1 are nearly equal. The latter is a result of competition between coupling strengths and asymptotic energy gaps. Initial state-selective cross sections for $\gamma = 0^{\circ}$, 90°, and 180° are shown respectively in Figs. 5.27-5.29. The dominant initial state for electron capture is $\nu' = 0$ in the high energy regime while the cross section decreases with increasing ν' . For the low energy region, capture from larger ν' becomes more important. In addition, because

there are exoergic collision channels involved in the electron capture process for any initial state ν' , all cross sections are expected to rise as the energy approaches zero. In Fig. 5.30, angle-averaged initial state-selective cross sections are presented which demonstrate some dependence of orientation angle by the comparison with Figs. 5.27-5.29.

In Fig. 5.31, orientation-angle-dependent and orientation-angle-averaged total cross sections for single electron capture by protons with CO are displayed and compared with other theoretical and experimental data. The calculations include a Boltzmann average of initial vibrational states at 300 K using Eq. (2.126). The orientation effect of the target molecule CO is elucidated through cross sections at the three specific angles. It's obvious that $\gamma = 0^{\circ}$ has the largest cross section, compared to the other two angles for energies larger than ~ 20 eV/u. The experimental results of Gao et al. [85], Kusakabe et al. [86], and Cadez et al. [87] were primarily measured for energies near or larger than 1 keV/u. For smaller energies, we are only aware of the measurements of Gilbody et al. [44] and Gustafsson et al. [83]. The current orientation-angle-averaged total cross sections are in generally good agreement with the other theoretical and experimental data. The discrepancies between the present IOSA results and the previous EA calculation [89], which neglected vibrational motion, illustrate the significant vibrational effect for the low energy regime. The current IOSA results are generally smaller than the measurements which may be due to the limited number of considered orientation angles or missing contributions from higher excited states. The orientation-angledependent and -averaged total cross sections for H-CO⁺ collisions are displayed in Fig. 5.32. Comparing to Fig. 5.31, the results of H-CO⁺ collisions in the high-energy region have a similar trend to H⁺-CO. Electron capture through collisions at $\gamma = 0^{\circ}$ are most significant, while $\gamma = 180^{\circ}$ has less contribution. We are unaware of other theoretical or experimental results in this collision energy range for this system.

5.4 ASTROPHYSICAL AND ATMOSPHERIC APPLICATIONS

CO is typically the second most abundant molecule, after molecular hydrogen, in a variety of astrophysical objects including interstellar clouds. In comets, CO accounts for about 15% of the gaseous material in the coma with the remainder due mostly to water. As a comet travels through the solar system, it encounters the solar wind which is composed primarily of protons with kinetic energies ranging from 0.2 to 3 keV/u. Collisions of CO with solar wind protons is the dominant mechanism for producing CO⁺, which is observed in fluorescence in comet tails [93], since solar photoionization is inefficient. As indicated in Fig. 5.15, CO⁺ is predominately created in the ground vibrational state. Further, in the earlier study, it was found that electron capture to electronically excited CO⁺ has a cross section more than two orders of magnitude smaller than to the ground state [88]. Therefore, while charge transfer creates CO⁺, the observed fluorescence is likely produced following electron-impact or solar photon excitation. Charge exchange also results in a loss of protons, a process observed in the coma of comet Halley, but previous models only considered proton charge exchange with water [94].

The reverse process of H collisions with CO⁺ may play a role in the chemistry of diffuse interstellar clouds. Federer *et al.* [84] measured the rate coefficient to be 40% of the Langevin value for a collision energy of 0.06 eV. This energy is too low for IOSA to be applicable, but if the trend indicated in Fig. 5.25(a) holds to low energies, the current results suggest that the charge transfer reaction H+CO⁺ would produced CO in ν =1 and 2 even in very cold environments.

5.5 Summary

Calculations for electron capture during proton collisions with CO and H collisions with CO⁺ have been performed for energies between 0.45 eV/u and 1 keV/u using the molecular-orbital coupled-channel approach with the infinite order sudden approximation. The adia-

batic potential curves and nonadiabatic radial couplings were obtained with the MRD-CI method. Taking into account the vibrational motion of the molecules, the vibrationally-resolved state-to-state and state-selective cross sections were obtained. The cross section variation with vibrational states is analyzed and the results of three collision orientations with $\gamma = 0^{\circ}$, 90° , and 180° manifestly elucidate the steric effect for H⁺-CO and H-CO⁺ collisions. The orientation-angle-averaged cross sections are in good agreement with experiments and it is shown that the electronic approximation may not be reliable for energies less than 100 eV/u. The large discrepancy between EA and IOSA calculations in the low-energy regime also reflects the significant influence of molecular vibrational motion. More experimental data for electron capture of protons with CO at energies less than 30 eV/u and for H collisions with CO⁺ are needed.

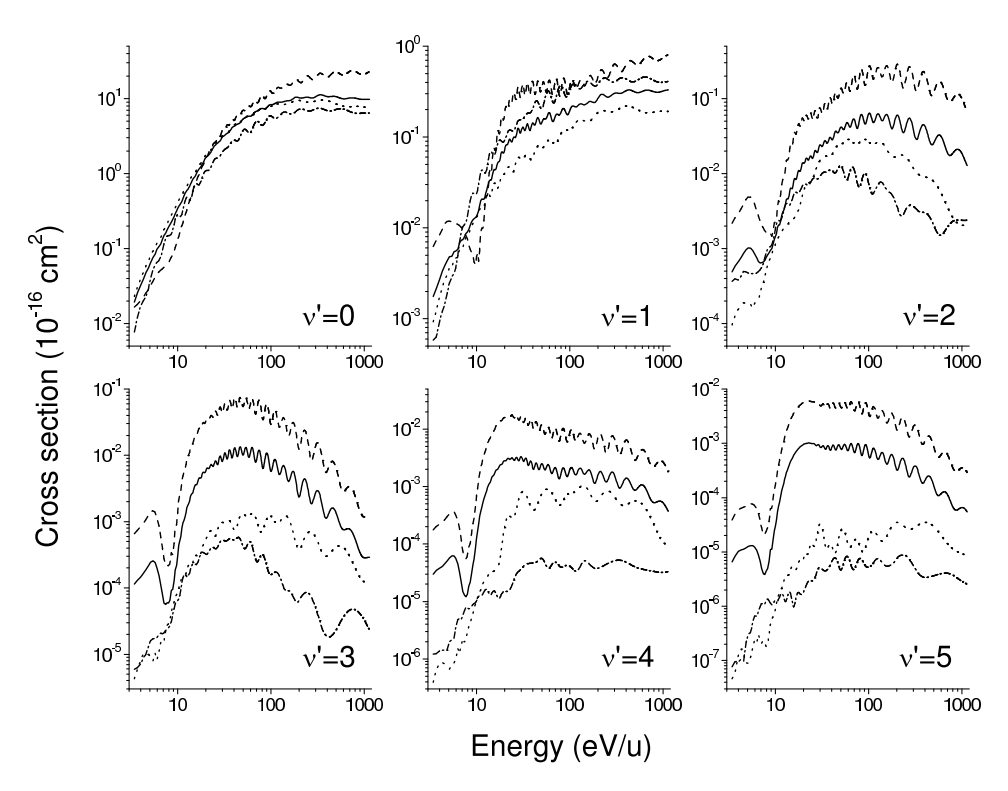


Figure 5.15: State-to-state cross sections for H⁺ + CO($\nu = 0$) \rightarrow H + CO⁺($\nu' = 0 - 5$) with dashed lines for $\gamma = 0^{\circ}$, dotted lines for $\gamma = 90^{\circ}$, dash-dotted lines for $\gamma = 180^{\circ}$, and solid lines for angle-averaged.

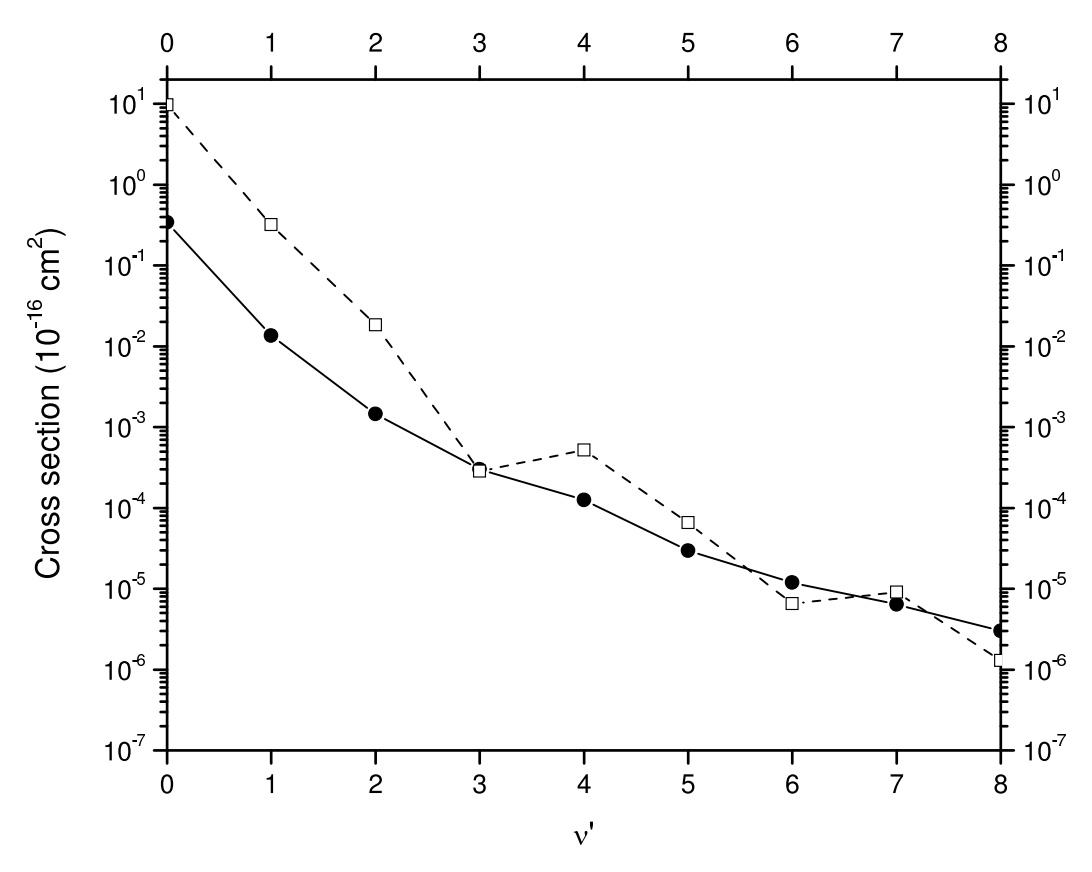


Figure 5.16: Angle-averaged state-to-state cross sections of H⁺ + $\rm CO(\nu=0) \rightarrow \rm H + \rm CO^+(\nu'=0-8)$ for 9.96 eV/u (circle-solid line) and 1001.50 eV/u (square-dashed line).

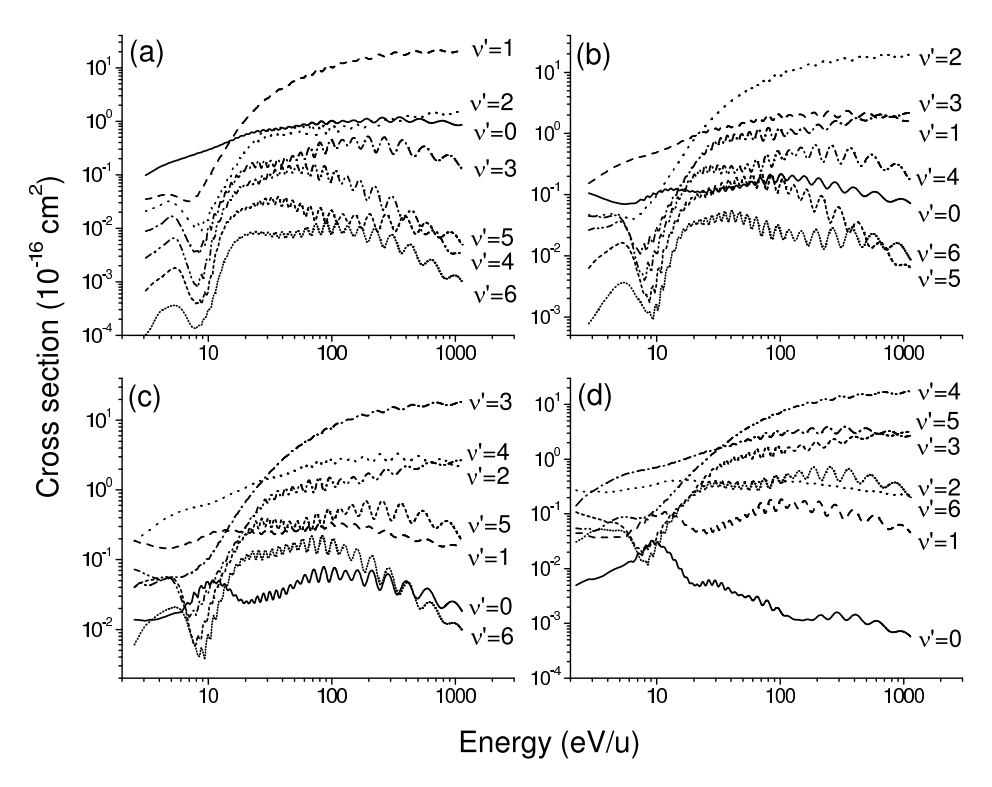


Figure 5.17: State-to-state cross sections of H⁺ + CO(ν) \rightarrow H + CO⁺(ν' = 0 - 6) for γ = 0°: (a) ν = 1, (b) ν = 2, (c) ν = 3, (d) ν = 4.

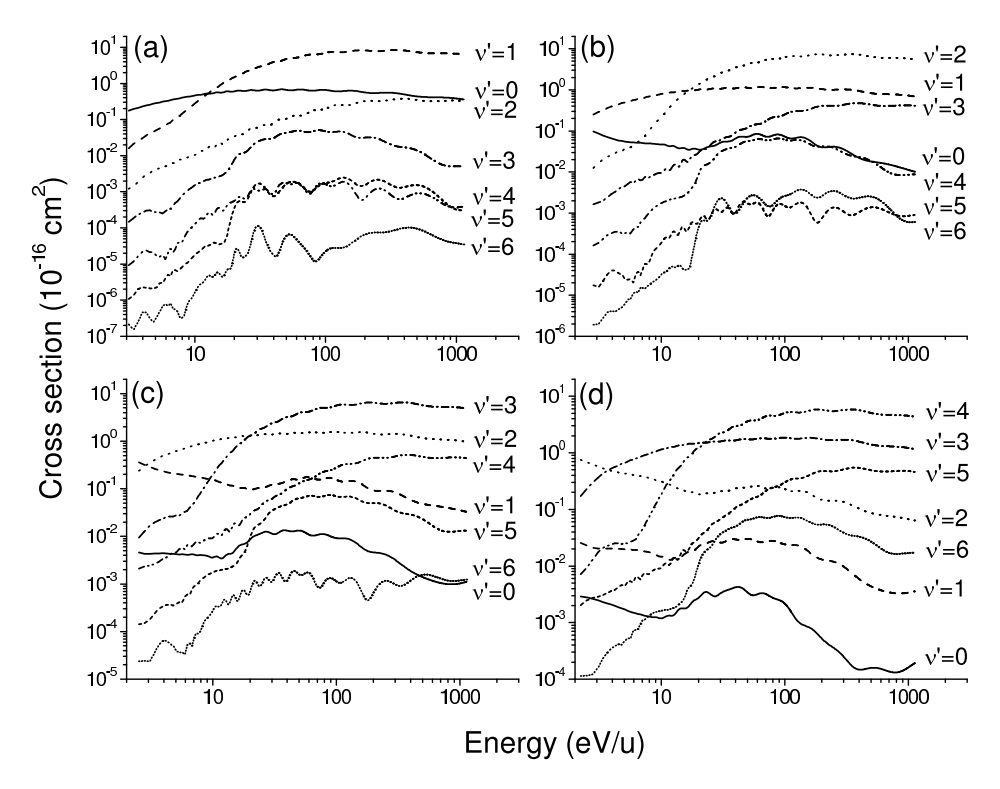


Figure 5.18: State-to-state cross sections of H⁺ + CO(ν) \rightarrow H + CO⁺(ν' = 0 - 6) for γ = 90°: (a) ν = 1, (b) ν = 2, (c) ν = 3, (d) ν = 4.

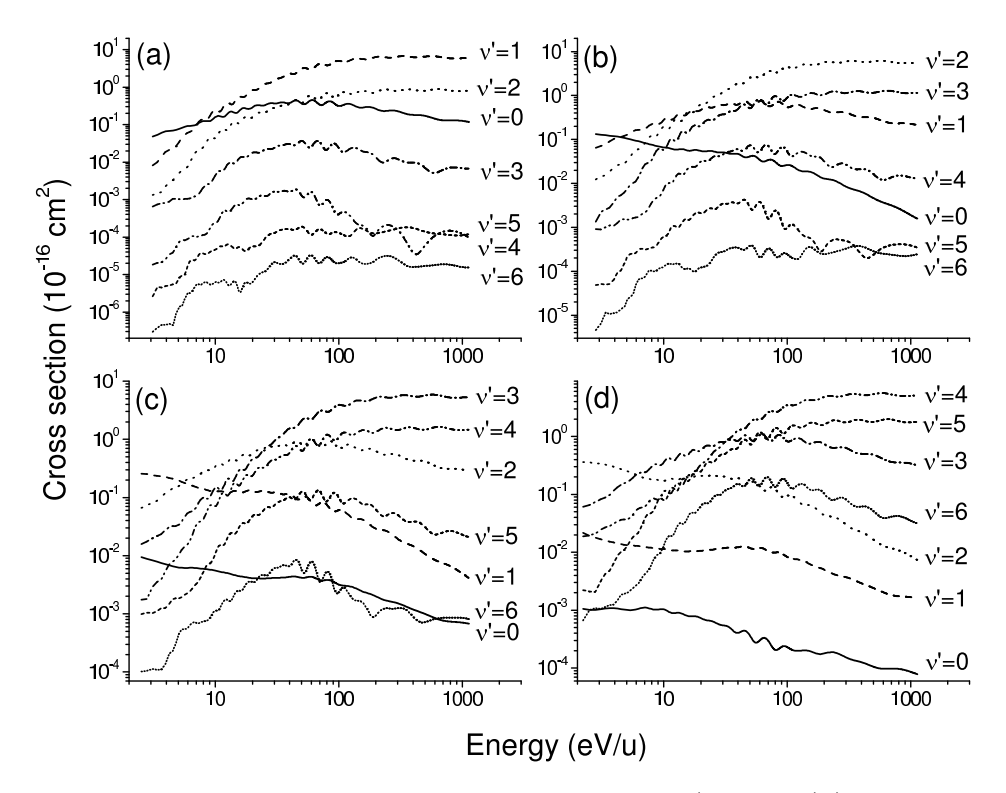


Figure 5.19: State-to-state cross sections of H⁺ + CO(ν) \rightarrow H + CO⁺(ν' = 0 - 6) for γ = 180°: (a) ν = 1, (b) ν = 2, (c) ν = 3, (d) ν = 4.

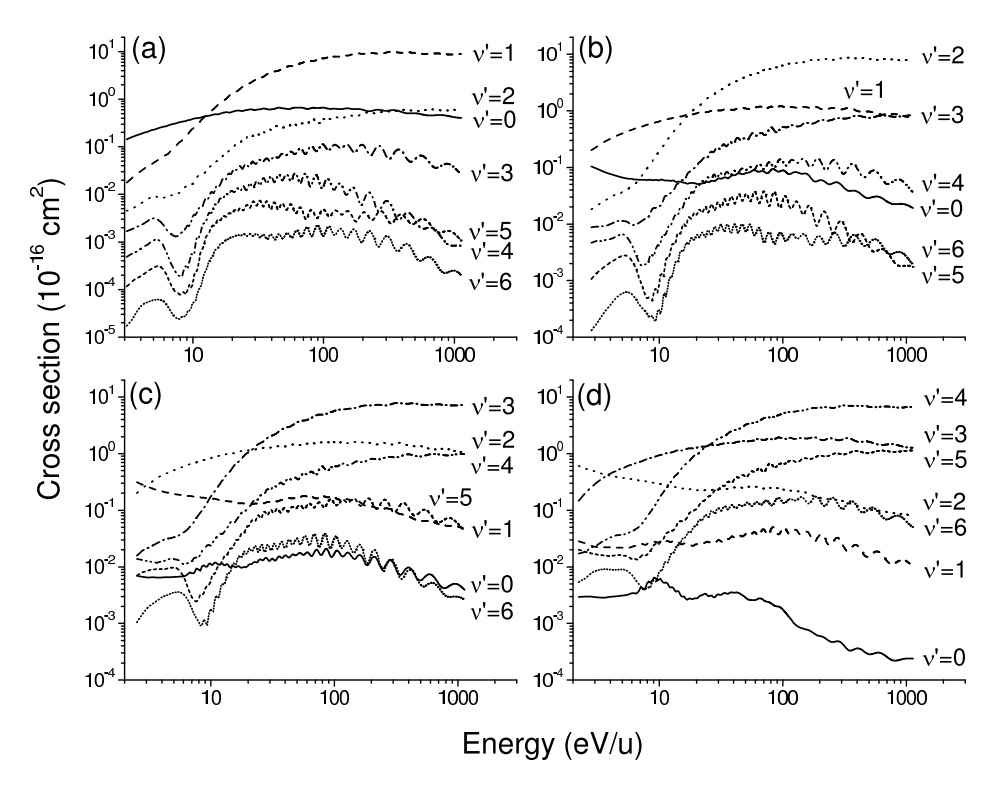


Figure 5.20: State-to-state cross sections of H⁺ + CO(ν) \rightarrow H + CO⁺(ν' = 0 - 6) for angle-averaged: (a) ν = 1, (b) ν = 2, (c) ν = 3, (d) ν = 4.

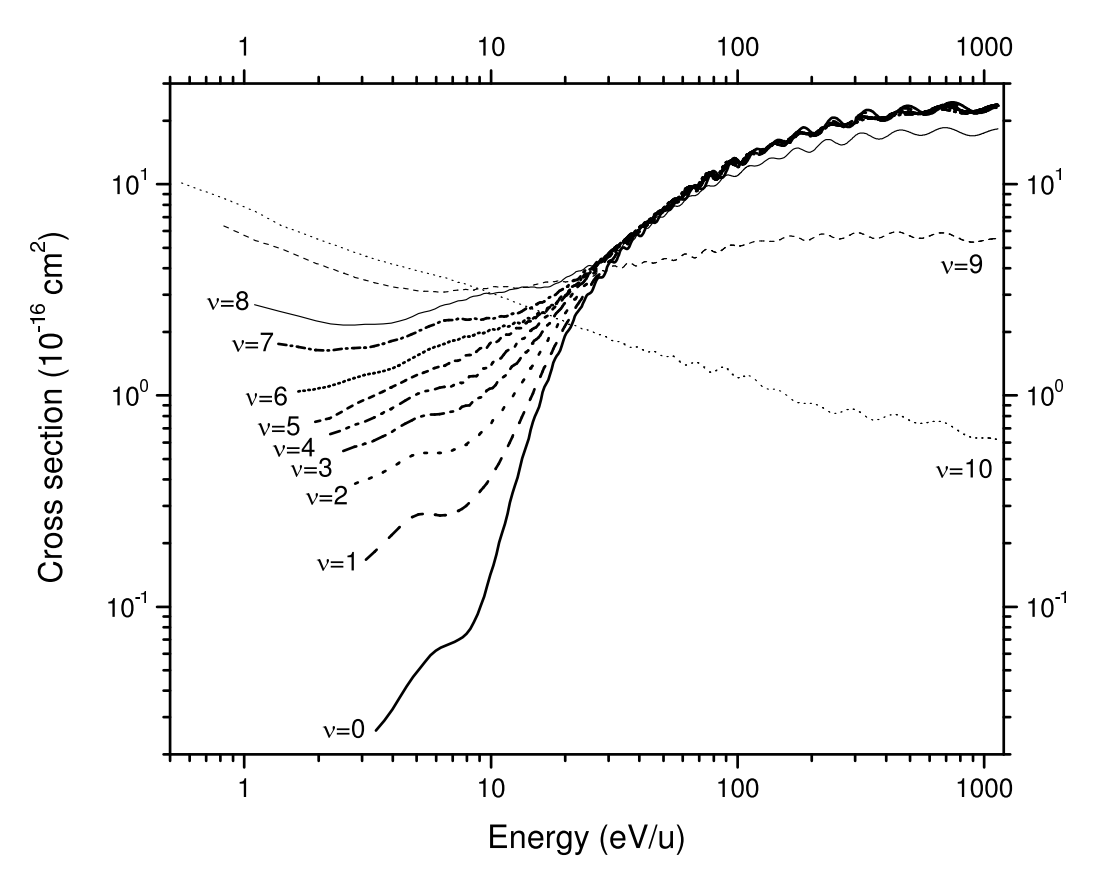


Figure 5.21: Initial state-selective cross sections of H⁺ collisions with CO ($\gamma=0^{\circ}$) for initial states of $\nu=0-10$.

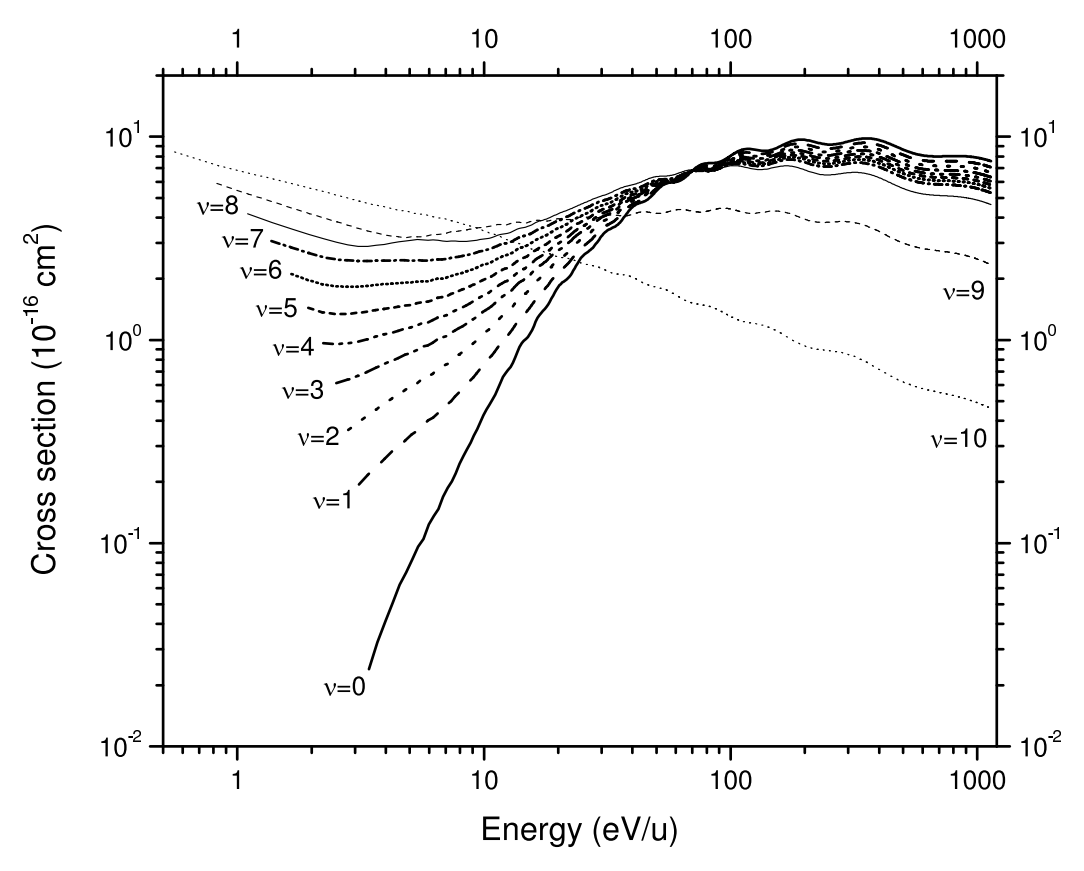


Figure 5.22: Initial state-selective cross sections of H⁺ collisions with CO ($\gamma=90^{\circ}$) for initial states of $\nu=0-10$.

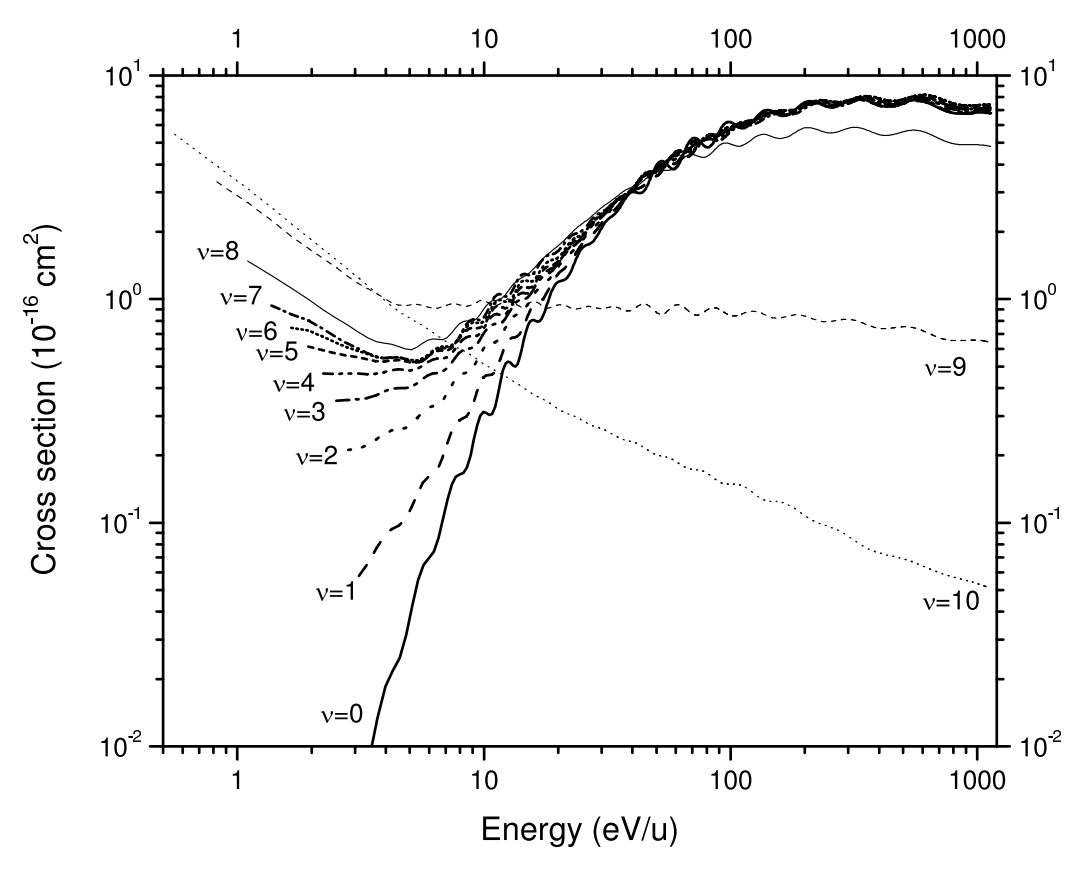


Figure 5.23: Initial state-selective cross sections of H⁺ collisions with CO ($\gamma=180^{\circ}$) for initial states of $\nu=0-10$.

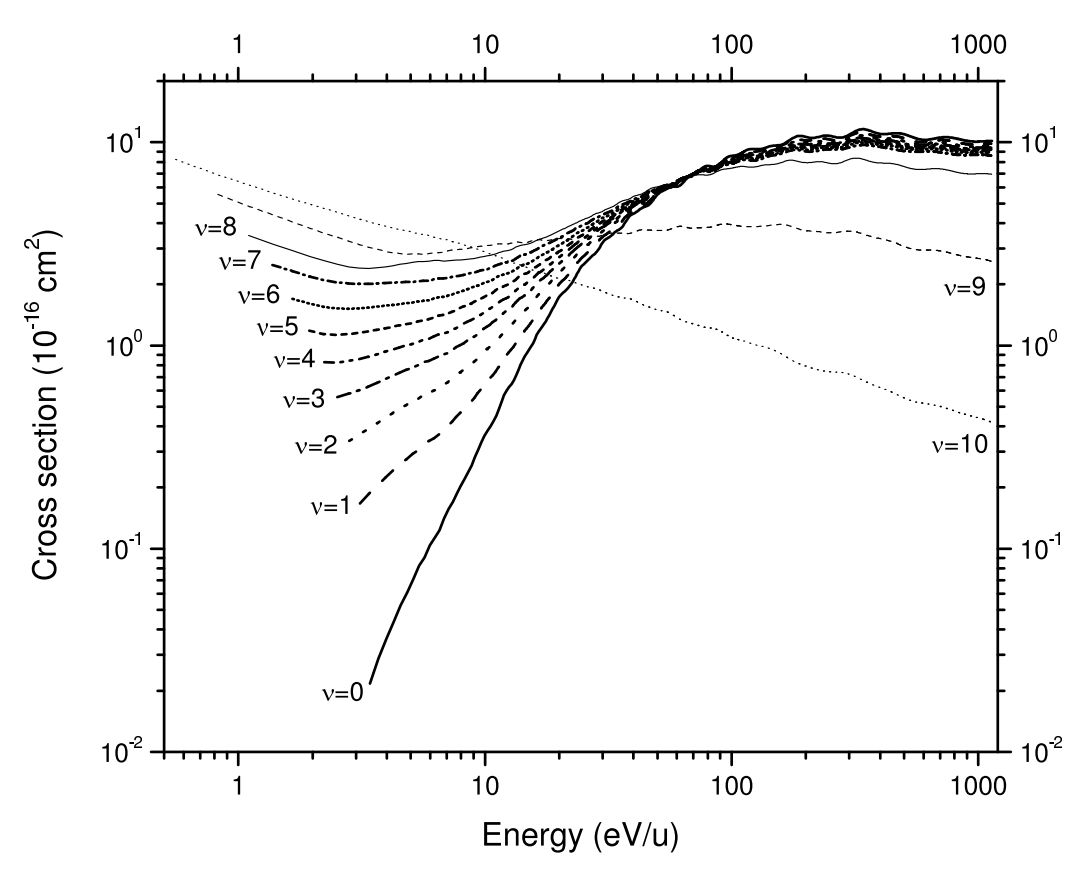


Figure 5.24: Angle-averaged initial state-selective cross sections of H⁺ collisions with CO for initial states of $\nu=0-10$.

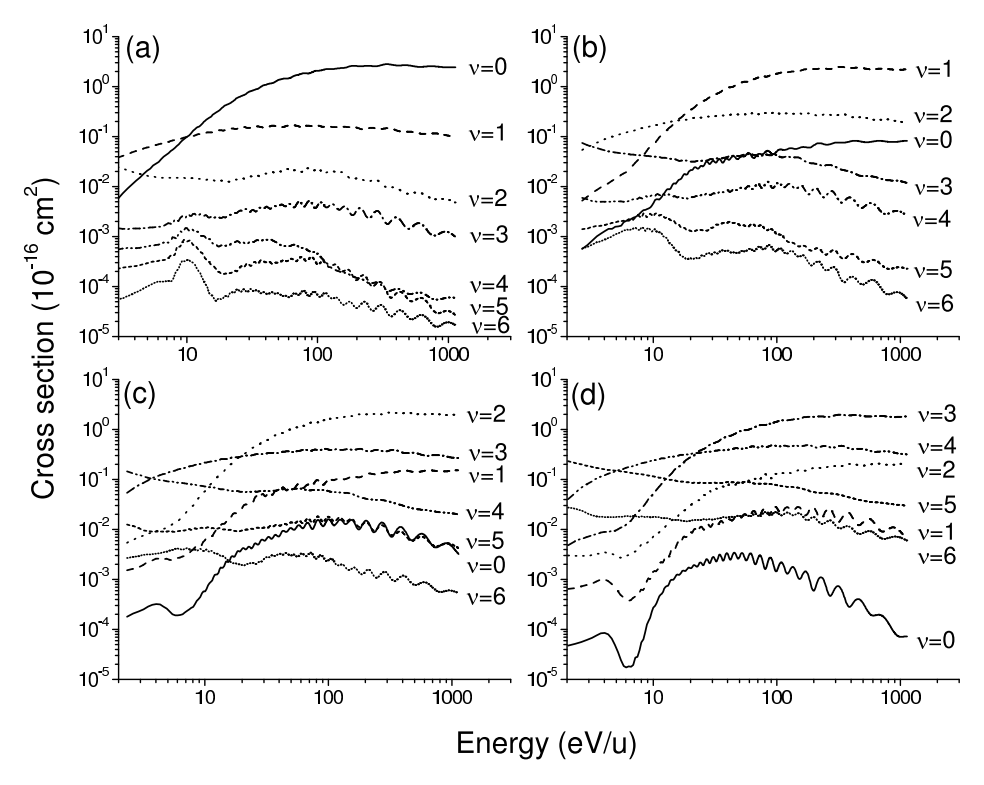


Figure 5.25: Angle-averaged state-to-state cross sections of H + $CO^+(\nu') \rightarrow H^+ + CO(\nu = 0 - 6)$ for (a) $\nu' = 0$, (b) $\nu' = 1$, (c) $\nu' = 2$, (d) $\nu' = 3$.

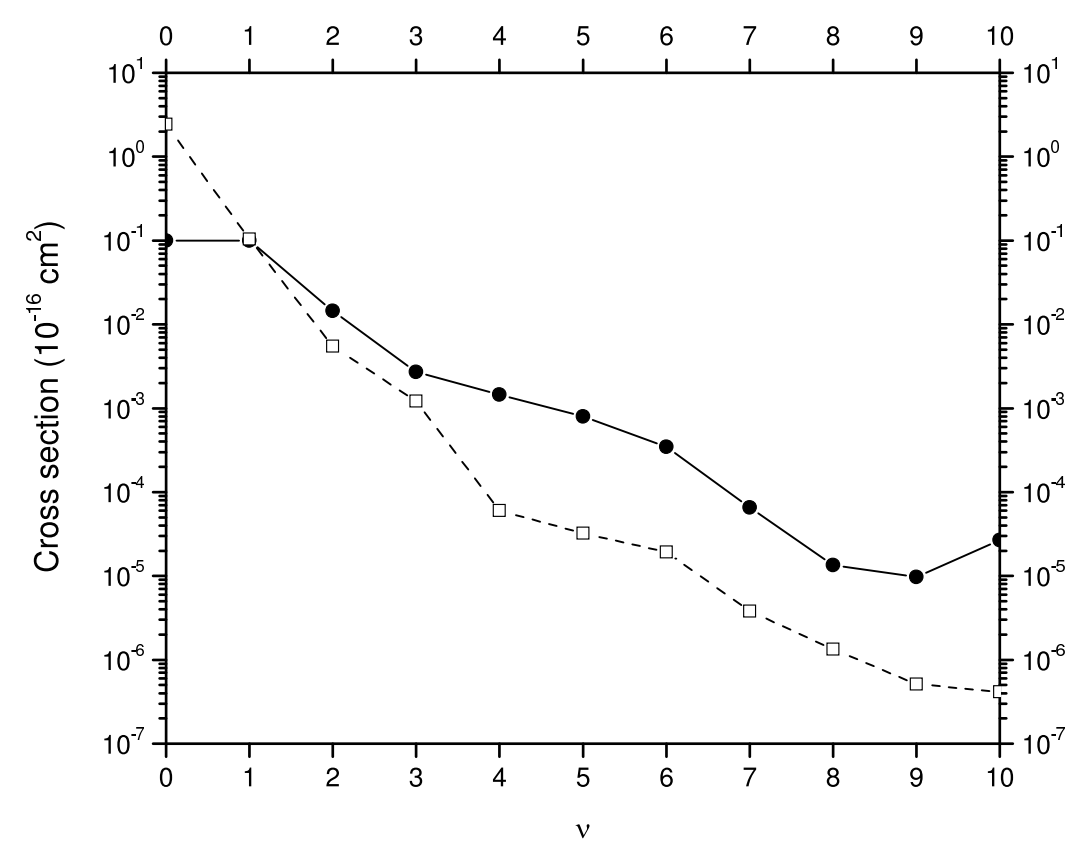


Figure 5.26: Angle-averaged state-to-state cross sections of H + $CO^+(\nu'=0) \rightarrow H^+ + CO(\nu=0-10)$ 10.06 eV/u (circle-solid line) and at 1001.03 eV/u (square-dashed line).

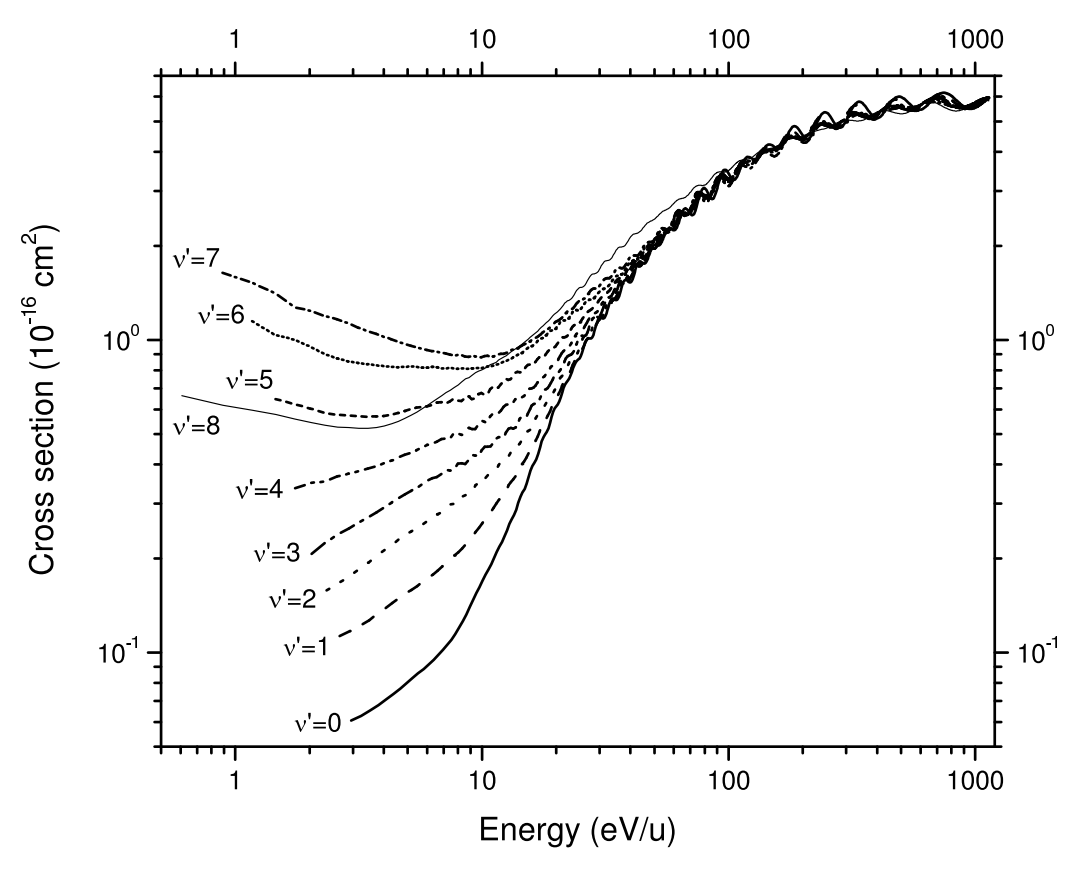


Figure 5.27: Initial state-selective cross sections of H collisions with CO⁺ ($\gamma=0^{\circ}$) for initial states of $\nu'=0-8$.

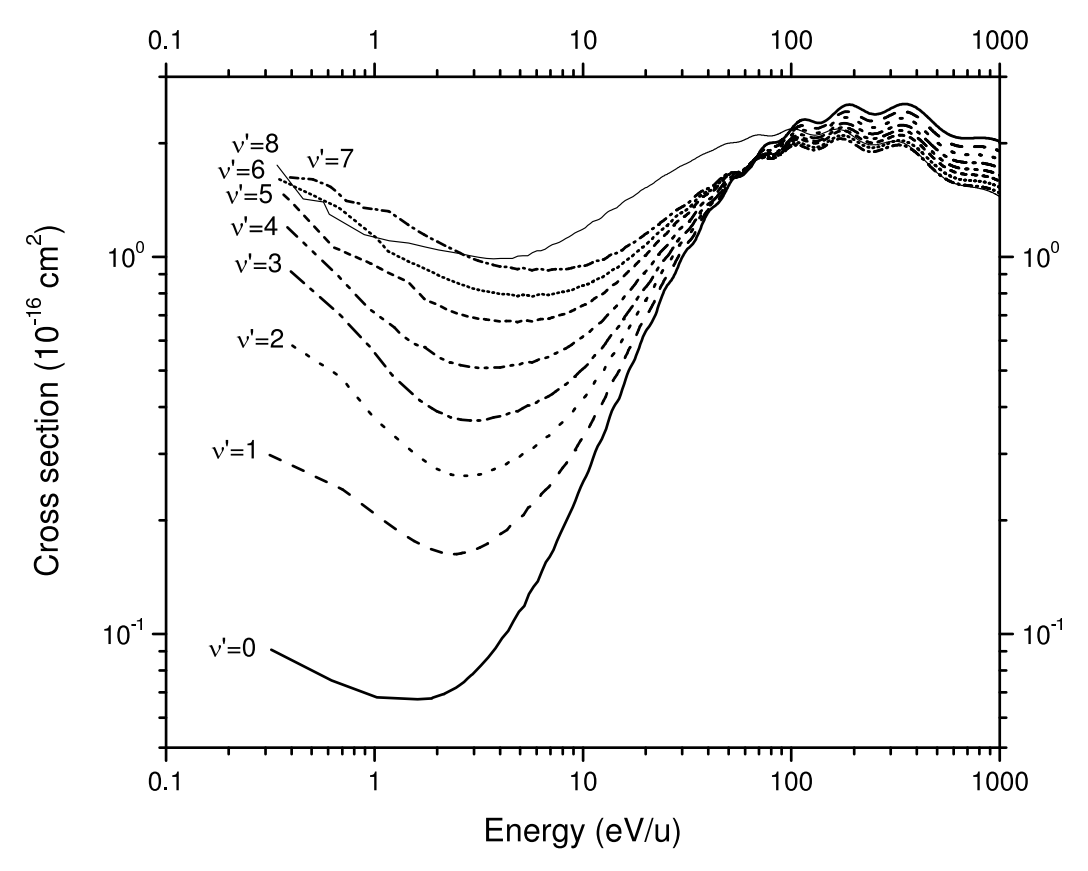


Figure 5.28: Initial state-selective cross sections of H collisions with CO⁺ ($\gamma=90^{\circ}$) for initial states of $\nu'=0-8$.

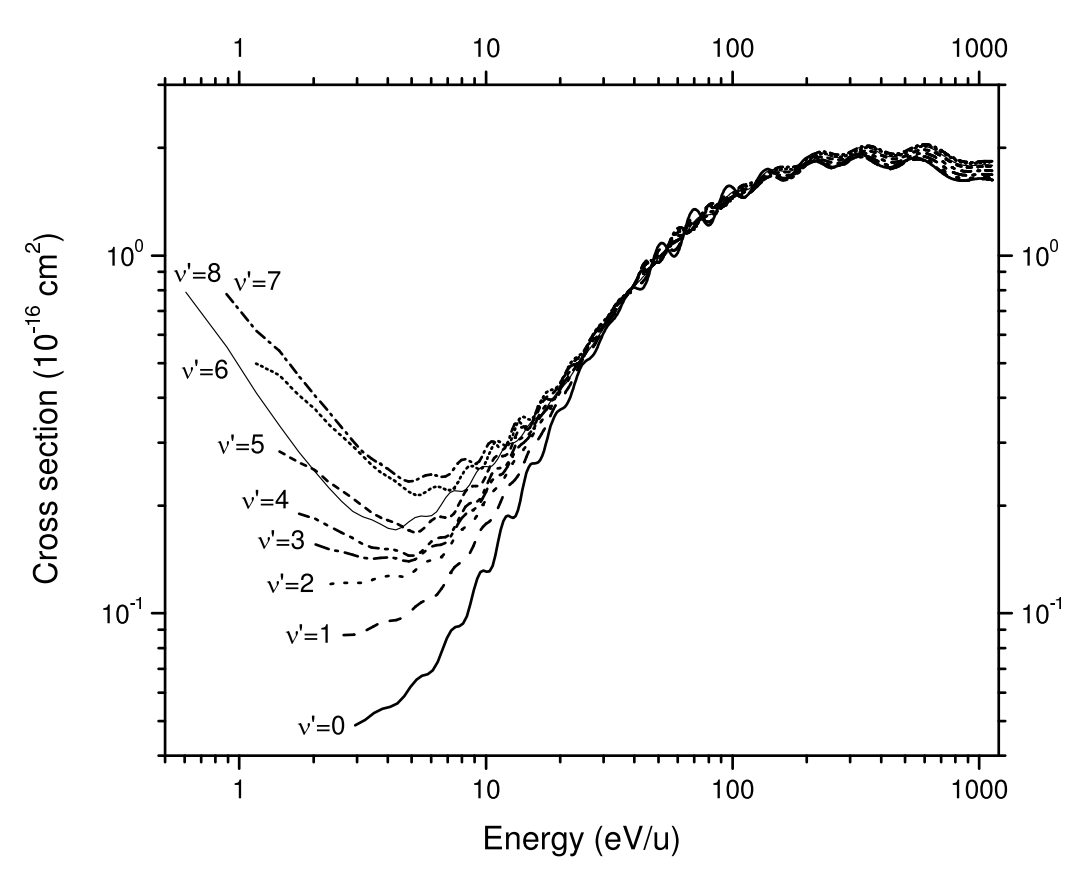


Figure 5.29: Initial state-selective cross sections of H collisions with CO⁺ ($\gamma=180^{\circ}$) for initial states of $\nu'=0-8$.

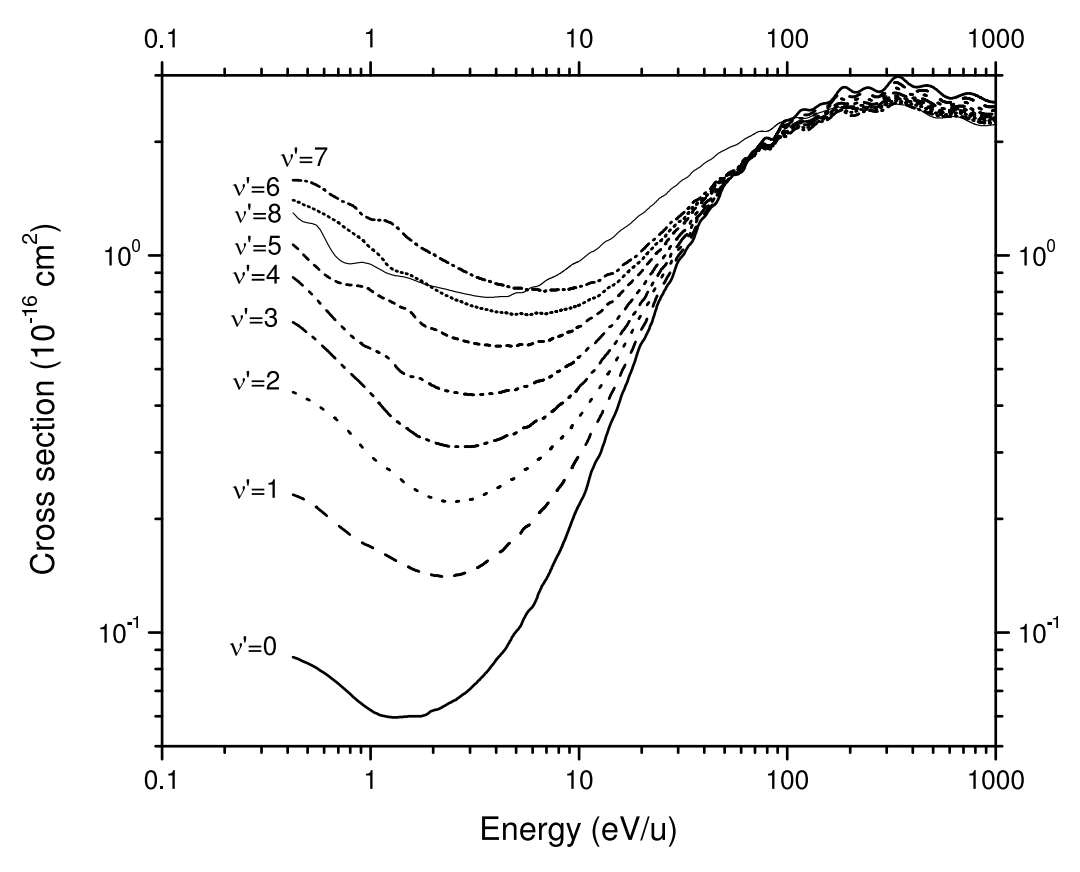


Figure 5.30: Angle-averaged initial state-selective cross sections of H collisions with CO⁺ for initial states of $\nu' = 0 - 8$.

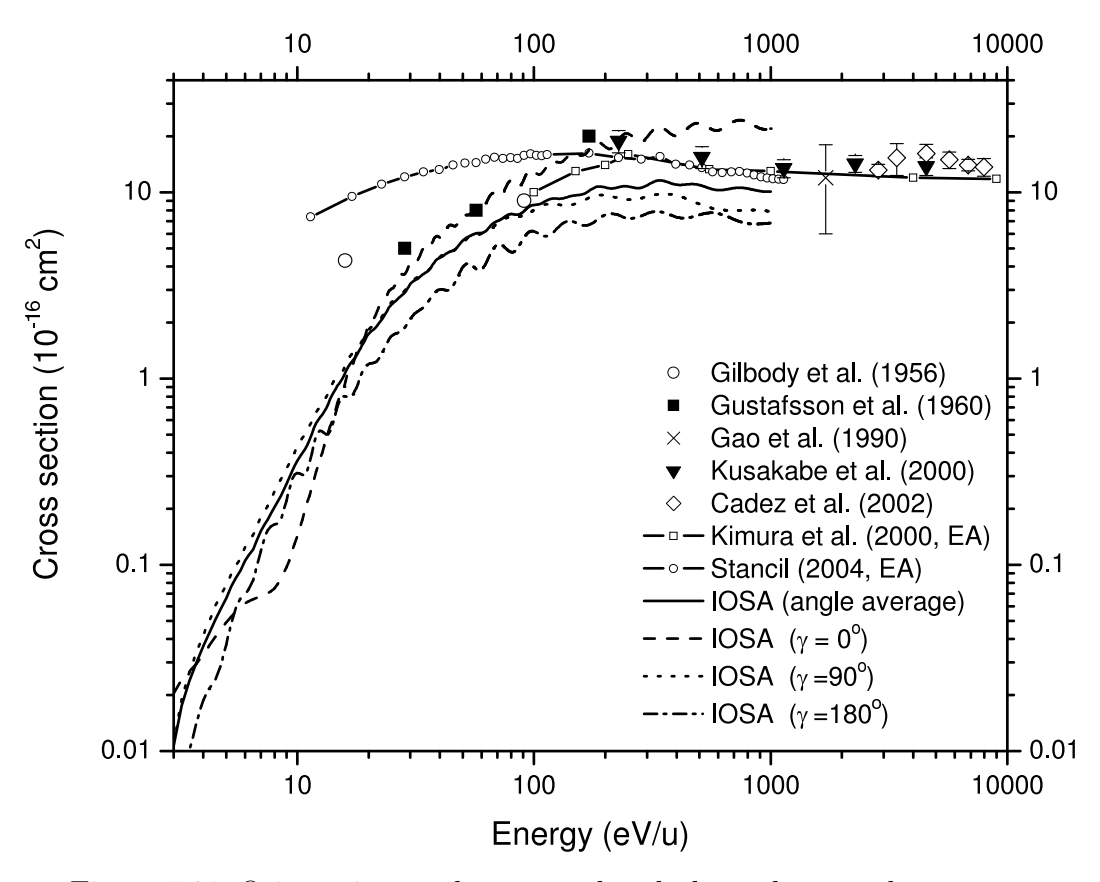


Figure 5.31: Orientation-angle-averaged and -dependent total cross sections for the collisions of ${\rm H^+}$ with CO compared with previous theoretical and experimental data.

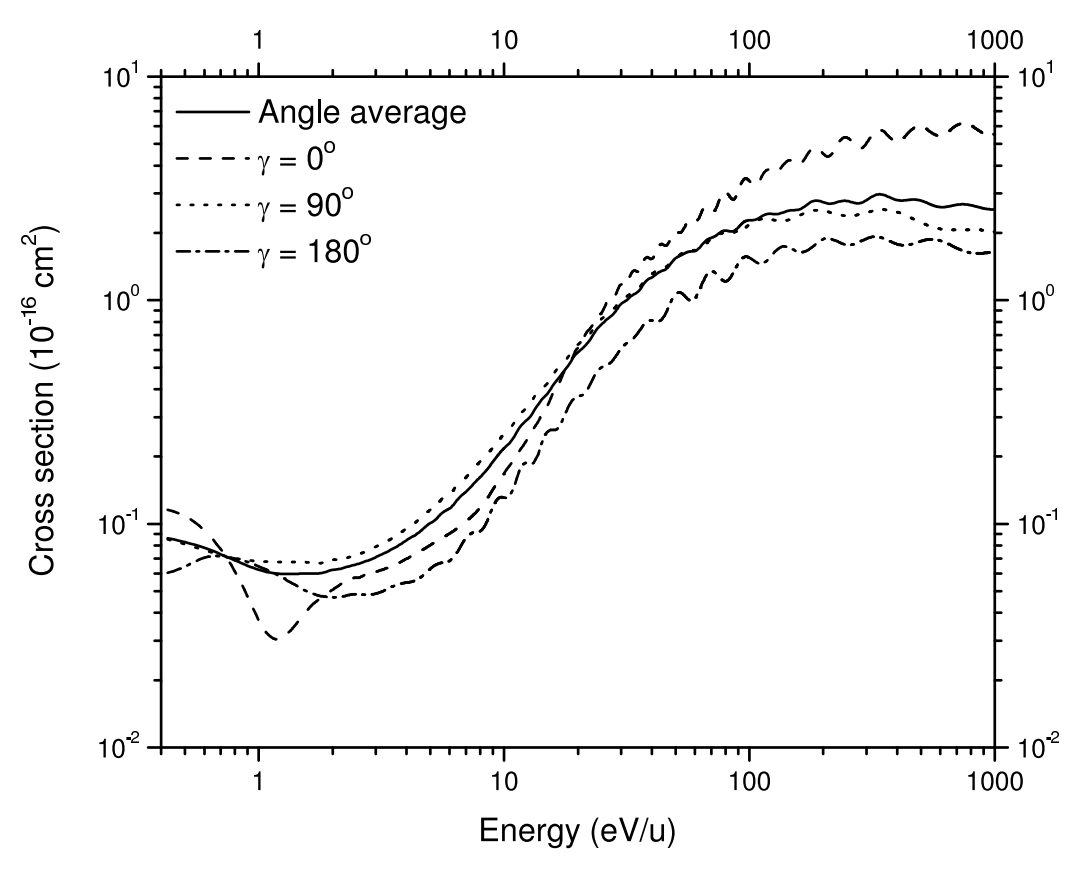


Figure 5.32: Orientation-angle-averaged and -dependent total cross sections for the collisions of H with $\rm CO^+$.

Chapter 6

SUMMARY AND FUTURE RESEARCH

In this dissertation, I have focused on the MOCC method and appplied it to atom-ion, atomatom, and ion-molecule collisions. For ion collisions, the charge transfer process is known to be crucial in many astrophyscial environments. My results for electron capture of N⁺ with H provide the important adiabatic potential energies and couplings calculated by MRD-CI, charge exchange cross sections, and rate coefficients, which could clarify the role played by radial and rotational coupling compared to spin-orbit coupling and the influence of the process in photoionized nebulae and Seyfert 2 galaxies.

Collisions of Na with He are important in the thermal regime for astrophysical implications, but also of interest in the ultracold and at cold temperatures for buffer gas cooling of sodium. The potential curves and couplings provided by the MRD-CI method are presented. The total elastic cross sections compared with partial-wave cross sections are shown to elucidate the dominant channels. Total and state-to-state quenching and excitation cross sections are also given. Thermal rate coefficients for electronic excitation of Na were also obtained and will be used for modeling NLTE effects on Na D absorption lines in extrasolar planets. For ultralow temperatures, my results elucidate the strong relation between the scattering length and the depth of the electronic potential well.

I performed calculations of vibrationally-resolved electron capture due to collisions of protons with CO taking the collision system orientation angle into account for ion-molecule collisions. Adiabatic potentials and couplings as functions of the H-CO separation with five different C-O separations and three orientation angles are provided by the MRD-CI method. The MOCC method was extended to treat molecular targets adopting the IOSA approach.

Vibronic and steric effects for the process were studied and illustrated by the angle-averaged and angle-dependent state-to-state and total cross sections. Because proton collisions with CO is an important process in cometary atmospheres and protons are the dominant species in the solar wind, the reaction may explain the loss of solar wind protons observed at comet Halley.

For my future research, I propose to apply my experience with the close-coupling method to perform computational studies of large molecules, including biomolecules, and solid-state quantum computing devices, as well as to other collisional processes of astrophysical importance. To date, complex molecules have been translationally cooled by Stark deceleration [95]. With the ability to isolate a biomolecule in the gas phase, the potential to realize cold biomolecules by these or other techniques is expected soon. I therefore propose to study nonadiabatic interactions in collisions of cold biomolecules (e.g., uracil, thymine) with various atoms and polar molecules (e.g. NH, OH) which can also be cooled. I will use standard quantum chemistry packages to generate potential surfaces and model the nonadiabatic couplings. Such computational studies will give insight into cold biomolecular dynamics and motivate future measurements.

The use of helium nanodroplets [96] for precision vibrational and electronic spectroscopy has seen significant activity in the past decade with a large number of molecules including C₆₀ and organic polyaromatics, among others, being studied. However, compared to gas-phase spectroscopy, the He superfluid environment does result in line shifts and line broadening which can be modeled by considered the binary He-molecule interaction. So far, line shift and broadening calculations have been limited to HF, CO, and OCS. I propose to perform such calculations for large molecules and ultimately to address biomolecules such as uracil. The scattering calculations will be performed by adapting the general scattering code MOLSCAT [97]. He-molecule potential surfaces will also be calculated with standard quantum chemistry packages.

In my current work on ion-molecule collisions, the IOSA method has been adopted which neglects the internal rotational motion of the diatom. The method is therefore only valid for translational energies much larger than the typical rotational energy spacing, ~ 0.5 eV. To extend the H⁺-CO studies to lower energies, I propose to incorporate the internal rotational angular momentum, say with a coupled-states or full close-coupling approach, with electronic nonadiabatic interactions. Then it would be possible to provide rate coefficients at astrophysical temperatures and to probe the cold temperature regime relevant to Stark deceleration techniques.

BIBLIOGRAPHY

- [1] S. Lepp, P. C. Stancil, and A. Dalgarno, J. Phys. B: At. Mol. Phys. 35, R57 (2002).
- [2] G. J. Ferland, K. T. Korista, D. A. Verner, J. W. Ferguson, J. B. Kingdon, and E. M. Verner, Publications of the Astronomical Society of the Pacific 110, 761 (1998).
- [3] M. C. Bacchus-Montabonel, M. Labuda, Y. S. Tergiman, and J. E. Sienkiewicz, Phys. Rev. A 72, 052706 (2005).
- [4] T. Schlathölter, F. Alvarado, S. Bari, and R. Hoekstra, Phys. Scr. 73 C113 (2006).
- [5] F. Hund, Z. Phys. **36**, 657 (1926).
- [6] R. S. Mulliken, Phys. Rev. **32**, 186 (1927).
- [7] J. E. Lennard-Jones, Trans. Faraday Soc. 25, 668 (1929).
- [8] J. B. Delos, Rev. Mod. Phys. **53**, 287 (1981).
- [9] B. H. Bransden and M. R. C. McDowell, Charge Exchange and the Theory of Ion-Atom Collisions (Clarendon Press, Oxford, 1992).
- [10] N. F. Mott and H. S. W. Massey, The Theory of Atomic Collisions (Clarendon Press, Oxford, 1965), p. 428.
- [11] A. M. Arthurs and A. Dalgarno, Proc. R. Soc. Lond. A **256**, 540 (1960).
- [12] T. P. Tsien and R. T. Pack, Chem. Phys. Lett. 6, 54 (1970).
- [13] S.-I. Chu and A. Dalgarno, Proc. R. Soc. Lond. A **342**, 119 (1975).

- [14] R. D. Levine, Chem. Phys. Lett. 4, 211 (1969).
- [15] R. B. Bernstein, Atom-Molecule Collision Theory (Plenum Press, New York, 1979).
- [16] V. Sidis, in Advances in Atomic, Molecular, and Optical Physics, edited by D. Bates and B. Bederson (Academic, New York, 1990), Vol. 26, p. 161.
- [17] M. Baer, in State-Selected and State-to-State Ion-Molecule Reaction Dynamics, edited by M. Baer and C.-Y. Ng (John Wiley & Sons, New York, 1992), Part 2, p. 187.
- [18] R. M. Häberli, T. I. Gombosi, D. L. D. Zeeuw, M. R. Combi and K. G. Powell, Science 276, 939 (1997).
- [19] T. E. Cravens, Science **296**, 1042 (2002).
- [20] R. P. Feynman, Phys. Rev. **56**, 340 (1939).
- [21] J. von Neumann and E. P. Wigner, Z. Physik **30**, 467 (1929).
- [22] C. J. Joachain, Quantum Collision Theory, 3rd ed., (North-Holland, Amsterdam, 1983), p. 288; p. 341.
- [23] T. G. Heil, S. E. Butler, and A. Dalgarno, Phys. Rev. A 23, 1100 (1981).
- [24] A. R. Edmond, Angular Momentum in Quantum Mechanics (Princeton University Press, New Jersey, 1957).
- [25] R. N. Zare, Angular Momentum (Wiley-Interscience, New York, 1988).
- [26] B. R. Johnson, J. Comput. Phys. **13**, 445 (1973).
- [27] J. C. Tully, in *Dynamics of Molecular Collisions*, edited by W. M. Miller (Plenum, New York, 1976), p. 217.
- [28] A. W. Kleyn, J. Los, and E. A. Gislason, Phys. Rep. 90, 1 (1982).

- [29] M. Baer, in Topics in Current Physics: Molecular Collisions Dynamics, edited by J.
 M. Bowman (Springer-Verlag, Berlin, 1983), Vol. 13, p. 117.
- [30] P. McGuire and J. C. Bellum, J. Chem. Phys **71**, 1975 (1979).
- [31] C. Y. Lin, P.C. Stancil, J.-P. Gu, R. J. Buenker and M. Kimura, Phys. Rev. A 71, 062708 (2005).
- [32] P. C. Stancil, B. Zygelman, N. J. Clarke, and D. L. Cooper, J. Phys. B: At. Mol. Phys. 30, 1013 (1997).
- [33] B. Zygelman, D. L. Cooper, M. J. Ford, A. Dalgarno, J. Gerratt, and M. Raimondi, Phys. Rev. A 46, 3846 (1992).
- [34] B. Zygelman, P. C. Stancil, N. J. Clarke, and D. L. Cooper, Phys. Rev. A 56, 457 (1997).
- [35] R. J. Buenker and S. D. Peyerimhoff, Theor. Chim. Acta 35, 33, (1974); 39, 217, (1975).
- [36] R. J. Buenker, in *Current Aspects of Quantum Chemistry*, edited by R. Carbo (Elsevier, Amsterdam, 1981), Vol. 21, p. 17.
- [37] S. Krebs and R. J. Buenker, J. Chem. Phys. **103**, 5613, (1995).
- [38] C. Galloy and J. C. Lorquet, J. Chem. Phys. **67**, 4672, (1977).
- [39] G. Hirsch, P. J. Bruna, R. J. Buenker, and S. D. Peyerimhoff, J. Chem. Phys. 45, 335, (1980).
- [40] N. Shimakura and M. Kimura, Phys. Rev. A 44, 1659 (1991).
- [41] R. F. Stebbings, W. L. Fite, and D. G. Hummer, J. Chem. Phys. 33, 1226 (1960).
- [42] M. Kimura, J. P. Gu, G. Hirsch, and R. J. Buenker, Phys. Rev. A 55, 2778 (1997).

- [43] R. Cabrera-Trujillo, Y. Öhrn, E. Deumens, and J. R. Sabin, Phys. Rev. A 62, 052714 (2000).
- [44] H. B. Gilbody and J. B. Hasted, Proc. R. Soc. London, Ser. A 238, 334 (1957).
- [45] G. Steigman, M. W. Werner, and F. M. Geldon, Astrophys. J. 168, 373 (1971).
- [46] S. E. Butler and A. Dalgarno, Astrophys. J. **234**, 765 (1979).
- [47] J. B. Kingdon and G. J. Ferland, Astrophys. J. Sup. Ser. **106**, 205 (1996).
- [48] J. B. Kingdon and G. J. Ferland, Astrophys. J. **516**, L107 (1999).
- [49] E. Oliva, A. Marconi, and A. F. Moorwood, Astron. Astrophys. 342, 87 (1999).
- [50] D. Charbonneau, T. M. Brown, R. W. Noyes, and R. L. Gilliland, Astrophys. J. 568, 377 (2002).
- [51] T. S. Barman, P. H. Hauschildt, A. Schweitzer, P. C. Stancil, E. Baron, and F. Allard, Astrophys. J. 569, L51 (2002).
- [52] C. Bottcher, T. C. Cravens, and A. Dalgarno, Proc. R. Soc. Lond. A **346**, 157 (1975).
- [53] N. Andersen and S. E. Nielsen, in Adv. At. Mol. Phys., edited by D Bates and B Bederson (Academic, New York, 1982), p. 266.
- [54] C. Courbin-Gaussorgues and V. Sidis, J. Phys. B: At. Mol. Phys. 18, 699 (1985).
- [55] M. Kimura and J. Pascale, J. Phys. B: At. Mol. Phys. 18, 2719 (1985).
- [56] W. Mecklenbrauck, J. Schön, E. Speller, and V. Kempter, J. Phys. B: At. Mol. Phys. 10, 3271 (1977).
- [57] J. O. Olsen, N. Andersen, and T. Andersen, J. Phys. B: At. Mol. Phys 10, 1723 (1977).
- [58] N. Andersen, T. Andersen, K. Bahr, C. L. Coche, E. Horsdal Pedersen, and J. Oest-gaard Olsen, J. Phys. B: At. Mol. Phys. 12, 2529 (1979).

- [59] L. L. Vahala, P. S. Julienne and M. D. Havey, Phys. Rev. A 34, 1856 (1986).
- [60] C. Zhu, J. F. Babb, and A. Dalgarno, Phys. Rev. A 73, 012506 (2006).
- [61] O. Dulieu, M. Raoult, and E. Tiemann, J. Phys. B: At. Mol. Opt. Phys. 39, (2006).
- [62] R. J. Buenker, Proceedings of the Workshop on Quantum Chemistry and Molecular Physics, edited by P. G. Burton (University of Wollongong Press, Wollongong, 1980), p. 1.5.1.
- [63] R. J. Buenker and R. A. Philips, THEOCHEM 123, 291 (1985).
- [64] D. E. Woon and T. H. Dunning, Jr., J. Chem. Phys. **100**, 2975 (1994).
- [65] T. H. Dunning, Jr., J. Chem. Phys. **90**, 1007 (1989).
- [66] D. Cvetko, A. Lausi, A. Morgante, F. Tommasini, P. Cortona, and M. G. Dondi, J. Chem. Phys. 100, 2052 (1994).
- [67] C. Zhu, A. Dalgarno, S. G. Porsev, and A. Derevianko, Phys. Rev. A 70, 032722 (2004).
- [68] T. R. Proctor and W. C. Stwalley, J. Chem. Phys. **66**, 2063 (1977).
- [69] U. Kleinekathöfer, M. Lewerenz, and M. Mladenović, Phys. Rev. Lett. 83, 4717 (1999).
- [70] J. Mitroy and M. W. J. Bromley, Phys. Rev. A 68, 062710 (2003).
- [71] M. D. Havey, S. E. Frolking, and J. J. Wright, Phys. Rev. Lett. 45, 1783 (1980).
- [72] R. V. Krems and A. Dalgarno, Phys. Rev. A 66, 012702 (2002).
- [73] E. P. Wigner, Phys. Rev. **73**, 1002 (1948).
- [74] A. K. Belyaev, J. Grosser, J. Hahne, and T. Menzel, Phys. Rev. A 60, 2151 (1999).
- [75] N. Balakrishnan, V. Kharchenko, R. C. Forrey, and A. Dalgarno, Chem. Phys. Lett. 280, 5 (1997).

- [76] P. J. Leo, V. Venturi, I. B. Whittingham, and J. F. Babb, Phys. Rev. A 64, 042710 (2001).
- [77] M. J. Jamieson and B. Zygelman, Phys. Rev. A 64, 032703 (2001).
- [78] S. Seager and D. D. Sasslov, Astrophys. J. **537**, 916 (2000).
- [79] T. M. Brown, D. Charbonneau, R. L. Gilliland, R. W. Noyes, and A. Burrows, Astrophys. J. 552, 699 (2001).
- [80] W. B. Hubbard, J. J. Fortney, J. I. Lunine, A. Burrows, D. Sudarsky, and P. Pinto, Astrophys. J. 560, 413 (2001).
- [81] J. J. Fortney, D. Sudarsky, I. Hubeny, C. S. Cooper, W. B. Hubbard, A. Burrows, and J. I. Lunine, Astrophys. J. 589, 615 (2003).
- [82] V. Sidis, in *Collision Theory for Atomx and Molecules*, edited by F. A. Gianturco (Plenum, New York, 1989).
- [83] E. Gustafsson and E. Lindholm, Ark. Fys. 18, 219 (1960).
- [84] W. Federer, H. Villinger, F. Howorka, W. Lindinger, P. Tosi, D. Bassi, and E. Ferguson, Phys. Rev. Lett. 52, 2084 (1984).
- [85] R. S. Gao, L. K. Johnson, C. L. Hakes, K. A. Smith, and R. F. Stebbings, Phys. Rev. A 41, 5929 (1990).
- [86] T. Kusakabe, K. Asahina, J.-P. Gu, G. Hirsch, R. J. Buenker, M. Kimura, H. Tawara, and Yohta Nakai, Phys. Rev. A 62, 062714 (2000).
- [87] I. Čadež, J. B. Greenwood, A. Chutjian, R. J. Mawhorter, S. J. Smith, and M. Niimura, J. Phys. B 35, 2515 (2002).
- [88] M. Kimura, J.-P. Gu, G. Hirsch, R. J. Buenker, and P. C. Stancil Phys. Rev. A 61, 032708 (2000).

- [89] P. C. Stancil, Physica Scripta **T110**, 340 (2004).
- [90] T. J. D. Kumar, A. Saieswari, and S. Kumar, J. Chem. Phys. **124**, 034314 (2006).
- [91] P. H. Krupenie and S. Weissman, J. Chem. Phys. 43, 1529 (1965).
- [92] I. Borges Jr., P. J. S. B. Caridade, and A. J. C. Varandas, J. Mol. Spectrosc. 209, 24 (2001).
- [93] L. Magnani and M. F. A'Hearn, Astrophys. J. **302**, 447 (1986).
- [94] S. A. Fuselier, E. G. Shelley, B. E. Goldstein, R. Goldstein, M. Neugebauer, W.-H. Ip, H. Balsiger, and H. Reme, Astrophys. J. 379, 734 (1991).
- [95] H. L. Bethlem, G. Berden and G. Meijer, Phys. Rev. Lett. 83, 1558 (1999).
- [96] J. P. Toennies and A. F. Vilesov, Angew. Chem. Int. Ed. 43, 2622 (2004).
- [97] J. M. Hutson and S. Green, Computer code MOLSCAT, version 14 (U.K. Engineering and Physical Sciences Research Council Collaborative Computational Project No. 6, 1994).

Appendix A

The derivation of coupled-channel equations

Given the Hamiltonian in Eq. (2.1) and the total wave function Ψ in Eq. (2.2), the L.H.S. of Eq. (2.5) is

$$H\Psi(\mathbf{s}, \mathbf{R}) = \left[-\frac{1}{2\mu} \nabla_{\mathbf{R}}^{2} - \frac{1}{2} \nabla_{\mathbf{s}}^{2} + V \right] \sum_{j=1}^{N} \psi_{j}(\mathbf{s}, \mathbf{R}) F_{j}(\mathbf{R})$$

$$= \sum_{j=1}^{N} \left(-\frac{1}{2\mu} \right) \nabla_{\mathbf{R}} \cdot \left[(\nabla_{\mathbf{R}} \psi_{j}(\mathbf{s}, \mathbf{R})) F_{j}(\mathbf{R}) + \psi_{j}(\mathbf{s}, \mathbf{R}) (\nabla_{\mathbf{R}} F_{j}(\mathbf{R})) \right]$$

$$+ \sum_{j=1}^{N} \left\{ -\frac{1}{2} \left(\nabla_{\mathbf{s}}^{2} \psi_{j}(\mathbf{s}, \mathbf{R}) \right) F_{j}(\mathbf{R}) + V \psi_{j}(\mathbf{s}, \mathbf{R}) F_{j}(\mathbf{R}) \right\}$$

$$= \sum_{j=1}^{N} \left\{ -\frac{1}{2\mu} \left(\nabla_{\mathbf{R}}^{2} \psi_{j}(\mathbf{s}, \mathbf{R}) \right) F_{j}(\mathbf{R}) - \frac{1}{\mu} \nabla_{\mathbf{R}} \psi_{j}(\mathbf{s}, \mathbf{R}) \cdot \nabla_{\mathbf{R}} F_{j}(\mathbf{R}) \right\}$$

$$-\frac{1}{2\mu} \psi_{j}(\mathbf{s}, \mathbf{R}) \nabla_{\mathbf{R}}^{2} F_{j}(\mathbf{R})$$

$$+ \sum_{j=1}^{N} \left[-\frac{1}{2} \nabla_{\mathbf{s}}^{2} \psi_{j}(\mathbf{s}, \mathbf{R}) + V \psi_{j}(\mathbf{s}, \mathbf{R}) \right] F_{j}(\mathbf{R}). \tag{A.1}$$

Using the above expression with Eqs. (2.3) and (2.4), we obtain

$$\int \psi_{i}^{*}(\mathbf{s}, \mathbf{R}) H \Psi(\mathbf{s}, \mathbf{R}) d\mathbf{s} = \sum_{j=1}^{N} \left\{ -\frac{1}{2\mu} \int \psi_{i}^{*}(\mathbf{s}, \mathbf{R}) \left[\nabla_{\mathbf{R}}^{2} \psi_{j}(\mathbf{s}, \mathbf{R}) \right] d\mathbf{s} F_{j}(\mathbf{R}) - \frac{1}{\mu} \int \left[\psi_{i}^{*}(\mathbf{s}, \mathbf{R}) \nabla_{\mathbf{R}} \psi_{j}(\mathbf{s}, \mathbf{R}) \right] d\mathbf{s} \cdot \nabla_{\mathbf{R}} F_{j}(\mathbf{R}) - \frac{1}{2\mu} \delta_{ij} \nabla_{\mathbf{R}}^{2} F_{j}(\mathbf{R}) + \varepsilon_{j}(R) \delta_{ij} F_{j}(\mathbf{R}) \right\} \\
= \sum_{j=1}^{N} \left[\frac{1}{2\mu} M_{ij}(\mathbf{R}) F_{j}(\mathbf{R}) + \frac{1}{2\mu} \mathbf{P}_{ij}(\mathbf{R}) \cdot \nabla_{\mathbf{R}} F_{j}(\mathbf{R}) \right] - \frac{1}{2\mu} \nabla_{\mathbf{R}}^{2} F_{i}(\mathbf{R}) + \varepsilon_{i}(R) F_{i}(\mathbf{R}), \tag{A.2}$$

where $M_{ij}(\mathbf{R})$ is defined in Eq. (2.8) and $\mathbf{P}_{ij}(\mathbf{R})$ is defined in Eq. (2.9). On the other hand,

$$\int \psi_i^*(\mathbf{s}, \mathbf{R}) E \Psi(\mathbf{s}, \mathbf{R}) d\mathbf{s} = E F_i(\mathbf{R}). \tag{A.3}$$

Given Eqs. (A.2) and (A.3), Eq. (2.6) leads to

$$\left[\nabla_{\mathbf{R}}^{2} - 2\mu(\varepsilon_{i}(R) - E)\right] F_{i}(\mathbf{R}) = \sum_{j=1}^{N} \left[M_{ij}(\mathbf{R}) + \mathbf{P}_{ij}(\mathbf{R}) \cdot \nabla_{\mathbf{R}}\right] F_{j}(\mathbf{R}), \tag{A.4}$$

which is Eq. (2.7).

Appendix B

THE ROTATION MATRIX

The rotation matrix defining the transformation between the body-fixed frame (x', y', z') and the space-fixed frame (x, y, z) is composed of three rotations corresponding to the three Euler angles α , β , and γ . Firstly, a rotation with the angle α about the z-axis brings the space-fixed frame (x, y, z) to the frame (x_1, y_1, z_1) (see Fig. (B.1)). This rotation can be represented by a transformation using a rotation matrix $R(\alpha)$,

$$R_z(\alpha) = \begin{pmatrix} \cos \alpha & \sin \alpha & 0 \\ -\sin \alpha & \cos \alpha & 0 \\ 0 & 0 & 1 \end{pmatrix}. \tag{B.1}$$

Secondly, a rotation with the angle β about the y_1 -axis brings the frame (x_1, y_1, z_1) to the frame (x_2, y_2, z_2) (see Fig. (B.2)). This rotation is expressed by a transformation using a rotation matrix $R(\beta)$,

$$R_{y_1}(\beta) = \begin{pmatrix} \cos \beta & 0 & -\sin \beta \\ 0 & 1 & 0 \\ \sin \beta & 0 & \cos \beta \end{pmatrix}.$$
 (B.2)

Thirdly, a rotation with the angle γ about z_2 -axis brings the frame (x_2, y_2, z_2) to the body-fixed frame (x', y', z') (see Fig. (B.3)). This rotation is given by a transformation using a rotation matrix $R(\gamma)$,

$$R_{z_2}(\gamma) = \begin{pmatrix} \cos \gamma & \sin \gamma & 0 \\ -\sin \gamma & \cos \gamma & 0 \\ 0 & 0 & 1 \end{pmatrix}.$$
 (B.3)

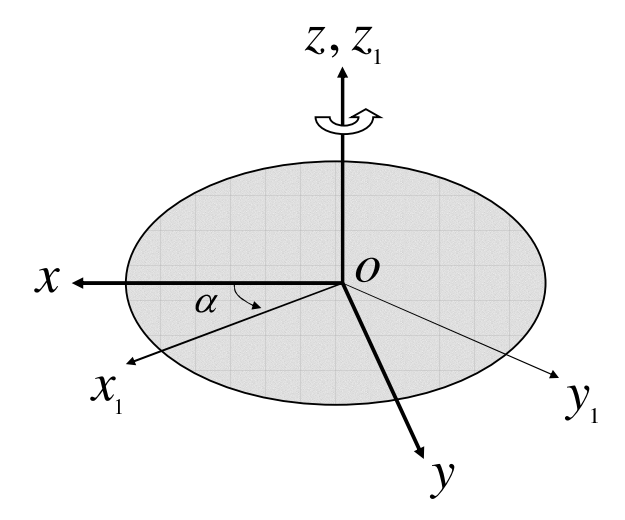


Figure B.1: A rotation about the z-axis by an angle α

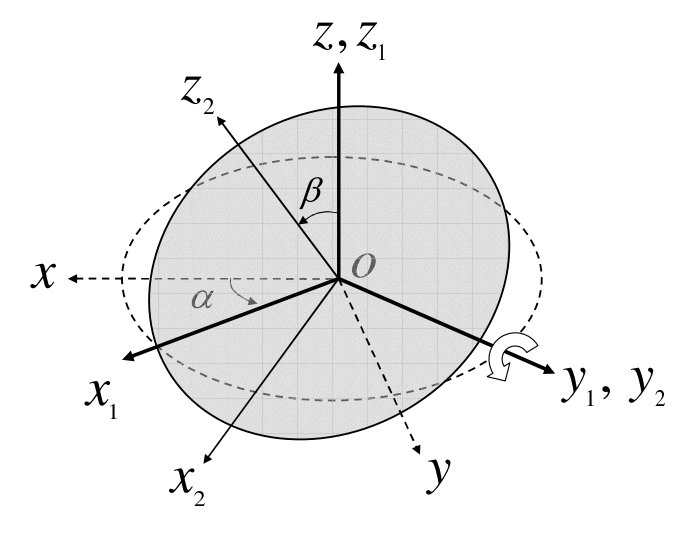


Figure B.2: A rotation about the y_1 -axis by an angle β

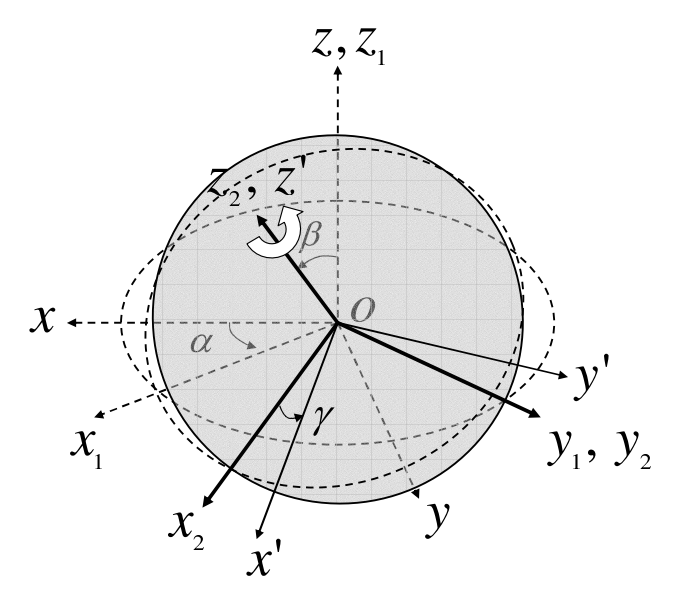


Figure B.3: A rotation about the z_2 -axis by an angle γ

Therefore, a rotation matrix $R(\gamma, \beta, \alpha)$ for a transformation from the space-fixed to the body-fixed frame is given as a product of these three rotations:

$$R(\gamma, \beta, \alpha) = R_{z_2}(\gamma)R_{y_1}(\beta)R_z(\alpha) =$$

$$\begin{pmatrix} \cos \alpha \cos \beta \cos \gamma & \sin \alpha \cos \beta \cos \gamma & -\sin \beta \cos \gamma \\ -\sin \alpha \sin \gamma & +\cos \alpha \sin \gamma & \\ -\cos \alpha \cos \beta \sin \gamma & -\sin \alpha \cos \beta \sin \gamma & \sin \beta \sin \gamma \\ -\sin \alpha \cos \gamma & +\cos \alpha \cos \gamma & \\ \cos \alpha \sin \beta & \sin \alpha \sin \beta & \cos \beta & \end{pmatrix}.$$
(B.4)

It is easily shown that for $\alpha = \Phi$, $\beta = \Theta$, and $\gamma = 0$, Eq. (B.4) reduces to Eq. (2.11).

Appendix C

ELECTRONIC WAVE FUNCTION DERIVATIVES IN THE BF FRAME

According to Eq. (2.10), the relationship between an electronic position vector in the body-fixed frame (x', y', z') and in the space-fixed frame (x, y, z) is given as

$$x' = x\cos\Theta\cos\Phi + y\cos\Theta\sin\Phi - z\sin\Theta, \tag{C.1a}$$

$$y' = -x\sin\Phi + y\cos\Phi,\tag{C.1b}$$

$$z' = x \sin \Theta \cos \Phi + y \sin \Theta \sin \Phi + z \cos \Theta, \tag{C.1c}$$

From Eq. (C.1), we can obtain

$$\frac{\partial x'}{\partial R} = \frac{\partial y'}{\partial R} = \frac{\partial z'}{\partial R} = 0,$$
(C.2a)

$$\frac{\partial x'}{\partial \Theta} = -x \sin \Theta \cos \Phi - y \sin \Theta \sin \Phi - z \cos \Theta$$

$$= -z', (C.2b)$$

$$\frac{\partial y'}{\partial \Theta} = 0, \tag{C.2c}$$

$$\frac{\partial z'}{\partial \Theta} = x \cos \Theta \cos \Phi + y \cos \Theta \sin \Phi - z \sin \Theta$$

$$= x', (C.2d)$$

$$\frac{\partial x'}{\partial \Phi} = -x\cos\Theta\sin\Phi + y\cos\Theta\cos\Phi$$

$$=y'\cos\Theta,$$
 (C.2e)

$$\frac{\partial y'}{\partial \Phi} = -x \cos \Phi - y \sin \Phi$$

$$= -x'\cos\Theta - z'\sin\Theta,\tag{C.2f}$$

$$\frac{\partial z'}{\partial \Phi} = -x \sin \Theta \sin \Phi + y \sin \Theta \cos \Phi$$

(C.3c)

$$= y' \sin \Theta.$$
 (C.2g)

With these derivatives, Eq. (2.17) gives the following relations:

$$\frac{\partial}{\partial R} = \frac{\partial'}{\partial R}, \qquad (C.3a)$$

$$\frac{\partial}{\partial \Theta} = \frac{\partial'}{\partial \Theta} - z' \frac{\partial}{\partial x'} + x' \frac{\partial}{\partial z'}$$

$$= \frac{\partial'}{\partial \Theta} - i\bar{L}_y, \qquad (C.3b)$$

$$\frac{\partial}{\partial \Phi} = \frac{\partial'}{\partial \Phi} + y' \cos\Theta \frac{\partial}{\partial x'} + (-x' \cos\Theta - z' \sin\Theta) \frac{\partial}{\partial y'} + y' \sin\Theta \frac{\partial}{\partial z'}$$

$$= \frac{\partial'}{\partial \Phi} + \cos\Theta \left(-x' \frac{\partial}{\partial y'} + y' \frac{\partial}{\partial x'} \right) + \sin\Theta \left(y' \frac{\partial}{\partial z'} - z' \frac{\partial}{\partial y'} \right)$$

$$= \frac{\partial'}{\partial \Phi} - i \cos\Theta \bar{L}_z + i \sin\Theta \bar{L}_x, \qquad (C.3c)$$

where \bar{L}_x , \bar{L}_y , and \bar{L}_z are defined as

$$\bar{L}_x = -i\left(y'\frac{\partial}{\partial z'} - z'\frac{\partial}{\partial y'}\right),$$
 (C.4a)

$$\bar{L}_y = -i\left(z'\frac{\partial}{\partial x'} - x'\frac{\partial}{\partial z'}\right),\tag{C.4b}$$

$$\bar{L}_z = -i\left(x'\frac{\partial}{\partial y'} - y'\frac{\partial}{\partial x'}\right). \tag{C.4c}$$

Similarly, the angular momentum $(\bar{L}_x, \bar{L}_y, \bar{L}_z)$ in the body-fixed frame is related to its components (L_x, L_y, L_z) in the space-fixed frame by

$$\bar{L}_x = L_x \cos\Theta \cos\Phi + L_y \cos\Theta \sin\Phi - L_z \sin\Theta, \tag{C.5a}$$

$$\bar{L}_y = -L_x \sin \Phi + L_y \cos \Phi, \tag{C.5b}$$

$$\bar{L}_z = L_x \sin \Theta \cos \Phi + L_y \sin \Theta \sin \Phi + L_z \cos \Theta. \tag{C.5c}$$

The reverse relationship is given as

$$L_x = \bar{L}_x \cos \Theta \cos \Phi - \bar{L}_y \sin \Phi + \bar{L}_z \sin \Theta \cos \Phi, \qquad (C.6a)$$

$$L_y = \bar{L}_x \cos \Theta \sin \Phi + \bar{L}_y \cos \Phi + \bar{L}_z \sin \Theta \sin \Phi, \qquad (C.6b)$$

$$L_z = -\bar{L}_x \sin\Theta + \bar{L}_z \cos\Theta. \tag{C.6c}$$

Appendix D

Angular momentum in spherical polar coordinates

Taking advantage of the transformation between Cartesian coordinates and spherical polar coordinates,

$$R = (x^2 + y^2 + z^2)^{1/2}, (D.1a)$$

$$\cos\Theta = \frac{z}{(x^2 + y^2 + z^2)^{1/2}},\tag{D.1b}$$

$$\tan \Phi = \frac{y}{x},\tag{D.1c}$$

we can transform the angular momentum in Cartesian coordinates,

$$N_x = -i\left(y\frac{\partial}{\partial z} - z\frac{\partial}{\partial y}\right),\tag{D.2a}$$

$$N_y = -i\left(z\frac{\partial}{\partial x} - x\frac{\partial}{\partial z}\right),\tag{D.2b}$$

$$N_z = -i\left(x\frac{\partial}{\partial y} - y\frac{\partial}{\partial x}\right),\tag{D.2c}$$

(D.2d)

into spherical polar coordinates,

$$N_x = i \left(\sin \Phi \frac{\partial}{\partial \Theta} + \cot \Theta \cos \Phi \frac{\partial}{\partial \Phi} \right), \tag{D.3a}$$

$$N_y = i \left(-\cos \Phi \frac{\partial}{\partial \Theta} + \cot \Theta \sin \Phi \frac{\partial}{\partial \Phi} \right), \tag{D.3b}$$

$$N_z = -i\frac{\partial}{\partial \Phi}.$$
 (D.3c)

(D.3d)

Appendix E

Total angular momentum

The total angular momentum J is defined as

$$\mathbf{J} = \mathbf{N} + \mathbf{L},\tag{E.1}$$

where N is total nuclear orbital angular momentum and L is total electronic orbital angular momentum. In the space-fixed frame, the operators of components of N can be expressed in spherical polar coordinates (see Appendix D) as

$$N_x = i \left(\sin \Phi \frac{\partial}{\partial \Theta} + \cot \Theta \cos \Phi \frac{\partial}{\partial \Phi} \right), \tag{E.2}$$

$$N_y = i \left(-\cos \Phi \frac{\partial}{\partial \Theta} + \cot \Theta \sin \Phi \frac{\partial}{\partial \Phi} \right), \tag{E.3}$$

and

$$N_z = -i\frac{\partial}{\partial \Phi}.$$
 (E.4)

From the above expressions, it follows that

$$N_{\pm} \equiv N_x \pm i N_y$$

$$= \exp \pm (i\Phi) \left(\pm \frac{\partial}{\partial \Theta} + i \cot \Theta \frac{\partial}{\partial \Phi} \right). \tag{E.5}$$

According to Eq. (E.1),

$$J_z = N_z + L_z$$

$$= -i\frac{\partial}{\partial \Phi} + L_z. \tag{E.6}$$

Because

$$-i\frac{\partial}{\partial\Phi} = -i\frac{\partial'}{\partial\Phi} - \cos\Theta\bar{L}_z + \sin\Theta\bar{L}_x, \tag{E.7}$$

from Eq. (C.3c) and

$$L_z = -\sin\Theta\bar{L}_x + \cos\Theta\bar{L}_z,\tag{E.8}$$

from Eq. (C.6c) we can immediately prove that

$$J_z = -i\frac{\partial'}{\partial\Phi}.\tag{E.9}$$

On the other hand, the expression for J_+ is given as

$$J_{+} \equiv J_{x} + iJ_{y}$$

$$= N_{x} + iN_{y} + L_{x} + iL_{y}$$

$$= N_{+} + L_{x} + iL_{y}$$

$$= \exp(i\Phi) \left(\frac{\partial}{\partial\Theta} + i\cot\Theta\frac{\partial}{\partial\Phi}\right) + L_{x} + iL_{y}.$$
(E.10)

Substituting Eqs. (C.3b) and (C.3c) for $\frac{\partial}{\partial \Theta}$ and $\frac{\partial}{\partial \Phi}$, and replacing L_x and L_y by their body-fixed representations (see Eq. (C.6)), we can obtain

$$J_{+} = \exp(i\Phi) \left(\frac{\partial'}{\partial \Theta} + i \cot \Theta \frac{\partial'}{\partial \Phi} \right) + \exp(i\Phi) \frac{\bar{L}_{z}}{\sin \Theta}.$$
 (E.11)

Similarly, the expression of J_{-} is given as

$$J_{-} \equiv J_{x} - iJ_{y}$$

$$= N_{-} + L_{x} - iLy$$

$$= \exp(-i\Phi) \left(-\frac{\partial}{\partial\Theta} + i\cot\Theta\frac{\partial}{\partial\Phi}\right) + L_{x} - iL_{y}.$$
(E.12)

Following the same procedure as Eq. (E.11) leads to

$$J_{-} = \exp(-i\Phi) \left(-\frac{\partial'}{\partial\Theta} + i\cot\Theta \frac{\partial'}{\partial\Phi} \right) + \exp(-i\Phi) \frac{\bar{L}_z}{\sin\Theta}.$$
 (E.13)

From Eqs. (E.11) and (E.13), we can obtain

$$J_{+}J_{-} = -\frac{\partial^{2}}{\partial\Theta^{2}} - \cot\Theta\frac{\partial^{2}}{\partial\Theta} - \frac{1}{\sin^{2}\Theta}\left(\cos\Theta\frac{\partial^{2}}{\partial\Phi} - i\bar{L}_{z}\right)^{2} - i\frac{\partial^{2}}{\partial\Phi}.$$
 (E.14)

Because the total angular momentum J can be written in the form

$$\mathbf{J}^2 = J_+ J_- - J_z + J_z^2, \tag{E.15}$$

applying Eqs. (E.14) and (E.9) to Eq. (E.15), the expression for \mathbf{J}^2 is given by

$$\mathbf{J}^{2} = -\frac{\partial^{2}}{\partial \Theta^{2}} - \cot \Theta \frac{\partial^{2}}{\partial \Theta} - \frac{1}{\sin^{2} \Theta} \left(\frac{\partial^{2}}{\partial \Phi} - i \cos \Theta \bar{L}_{z} \right)^{2} + \bar{L}_{z}^{2}.$$
 (E.16)

Appendix F

The raising and lowering operator

The relations of a raising J_+ or lowering J_- operator acting on a total angular momentum state $\mathbf{H}_{M,\lambda}^J(\Theta,\Phi)$ are given by

$$J_{\pm}\mathbf{H}_{M,\lambda}^{J}(\Theta,\Phi) = \sqrt{(J \pm M + 1)(J \mp M)}\mathbf{H}_{M\pm1,\lambda}^{J}(\Theta,\Phi).$$
 (F.1)

Substituting Eqs. (2.63) and (2.64) for J_{+} and J_{-} , this leads to

$$\exp(\pm i\Phi) \left(\pm \frac{\partial}{\partial \Theta} + i \cot \Theta \frac{\partial}{\partial \Phi} + \frac{\lambda}{\sin \Theta}\right) \mathbf{H}_{M,\lambda}^{J}(\Theta, \Phi)$$
$$= \sqrt{(J \pm M + 1)(J \mp M)} \mathbf{H}_{M\pm 1,\lambda}^{J}(\Theta, \Phi). \tag{F.2}$$

Because of Eq. (2.73), Eq. (F.2) can be written as

$$\exp\left(\pm i\Phi\right) \left(\pm \frac{\partial}{\partial\Theta} + \frac{\lambda - M\cos\Theta}{\sin\Theta}\right) d_{M,\lambda}^{J}(\Theta) \exp\left(iM\Phi\right)$$

$$= -\sqrt{(J \pm M + 1)(J \mp M)} d_{M\pm1,\lambda}^{J}(\Theta) \exp\left[i(M \pm 1)\Phi\right], \tag{F.3}$$

or

$$\left(\pm \frac{\partial}{\partial \Theta} + \frac{\lambda - M \cos \Theta}{\sin \Theta}\right) d_{M,\lambda}^{J}(\Theta) = -\sqrt{(J \pm M + 1)(J \mp M)} d_{M\pm 1,\lambda}^{J}(\Theta). \tag{F.4}$$

Let $\beta = -\Theta$, we obtain

$$\left(\mp \frac{\partial}{\partial \beta} - \frac{\lambda - M \cos \beta}{\sin \beta}\right) d_{M,\lambda}^{J}(-\beta) = -\sqrt{(J \pm M + 1)(J \mp M)} d_{M\pm 1,\lambda}^{J}(-\beta). \tag{F.5}$$

Since $d_{M,\lambda}^J(-\beta) = d_{\lambda,M}^J(\beta)$ (see Eq. (2.80)), it is easy to obtain

$$\left(\mp \frac{\partial}{\partial \beta} - \frac{\lambda - M \cos \beta}{\sin \beta}\right) d_{\lambda,M}^{J}(\beta) = -\sqrt{(J \pm M + 1)(J \mp M)} d_{\lambda,M\pm 1}^{J}(\beta). \tag{F.6}$$

By an exchange of λ and M, Eq. (F.6) becomes

$$\left(\mp \frac{\partial}{\partial \beta} - \frac{M - \lambda \cos \beta}{\sin \beta}\right) d_{M,\lambda}^{J}(\beta) = -\sqrt{(J \pm \lambda + 1)(J \mp \lambda)} d_{M,\lambda \pm 1}^{J}(\beta). \tag{F.7}$$

Finally, let $\beta = \Theta$ to

$$\left(\mp \frac{\partial}{\partial \Theta} - \frac{M - \lambda \cos \Theta}{\sin \Theta}\right) d_{M,\lambda}^{J}(\Theta) = -\sqrt{(J \pm \lambda + 1)(J \mp \lambda)} d_{M,\lambda \pm 1}^{J}(\Theta). \tag{F.8}$$

Eq. (F.8) is equivalent to

$$\left[\mp \frac{\partial}{\partial \Theta} + \frac{i}{\sin \Theta} \frac{\partial}{\partial \Phi} + \lambda \cot \Theta\right] d_{M,\lambda}^{J}(\Theta) \exp(iM\Phi)$$

$$= -\sqrt{(J \pm \lambda + 1)(J \mp \lambda)} d_{M,\lambda \pm 1}^{J}(\Theta) \exp(iM\Phi), \tag{F.9}$$

or

$$\left[\mp \frac{\partial}{\partial \Theta} + \frac{i}{\sin \Theta} \frac{\partial}{\partial \Phi} + \lambda \cot \Theta\right] \mathbf{H}_{M,\lambda}^{J}(\Theta, \Phi)$$

$$= \sqrt{(J \pm \lambda + 1)(J \mp \lambda)} \mathbf{H}_{M,\lambda \pm 1}^{J}(\Theta, \Phi). \tag{F.10}$$

Appendix G

THE DIFFERENTIAL CROSS SECTION

The differential cross section $\frac{d\sigma}{d\Omega}$ is defined by the ratio of the number of particles scattered into $d\Omega$ per unit time and the number of incident particles crossing unit area per unit time, i.e.

$$\frac{\partial \sigma}{\partial \Omega} d\Omega = \frac{(\mathbf{j}_{scatt} \cdot \hat{R}) R^2 d\Omega}{(\mathbf{j}_{incid} \cdot \hat{z})},\tag{G.1}$$

where $d\Omega$ is a differential solid-angle element, \hat{z} the incident direction, \mathbf{j}_{scatt} the scattered probability flux, and \mathbf{j}_{incid} the incident probability flux.

For a transition from the incident channel i into the open channel j with $k_j^2 > 0$, the asymptotic channel wave function (see Eq. (2.104)) for the incident channel is

$$G_i(\mathbf{R}) = A \exp(ik_i z),$$
 (G.2)

and for the scattered channel is

$$G_j(\mathbf{R}) = \frac{A}{R} f_{ji}(\Theta, \Phi) \exp(ik_j R). \tag{G.3}$$

By the definition of the probability flux

$$\mathbf{j} = \frac{1}{\mu} \operatorname{Im}(G^*(\mathbf{R}) \nabla G(\mathbf{R})), \tag{G.4}$$

where μ is the reduced mass of the scattering system, we obtain

$$\mathbf{j}_{scatt} \cdot \hat{R} = \frac{1}{\mu} \operatorname{Im} \left(G_j^*(\mathbf{R}) \frac{\partial}{\partial R} G_j(\mathbf{R}) \right),$$

$$= \frac{A^2}{\mu} \operatorname{Im} \left(\frac{ik_j}{R^2} |f_{ji}(\Theta, \Phi)|^2 \right),$$

$$= \frac{A^2 k_j}{\mu R^2} |f_{ji}(\Theta, \Phi)|^2,$$
(G.5)

 $\quad \text{and} \quad$

$$\mathbf{j}_{incid} \cdot \hat{z} = \frac{1}{\mu} \operatorname{Im} \left(G_i^*(\mathbf{R}) \frac{\partial}{\partial z} G_i(\mathbf{R}) \right),$$

$$= \frac{A^2}{\mu} k_i.$$
(G.6)

Therefore, Eq. (G.1) leads to

$$\frac{\partial \sigma_{ji}}{\partial \Omega} d\Omega = \frac{k_j}{k_i} |f_{ji}(\Theta, \Phi)|^2 d\Omega, \tag{G.7}$$

or

$$\frac{d\sigma_{ji}}{d\Omega} = \frac{k_j}{k_i} |f_{ji}(\Theta, \Phi)|^2.$$
 (G.8)